

RICE UNIVERSITY

**Three-Dimensional Biomimetic Patterning to Guide Cellular
Migration and Organization**


by

Joseph Charles Hoffmann


A THESIS SUBMITTED
IN PARTIAL FULFILLMENT OF THE
REQUIREMENTS FOR THE DEGREE

Doctor of Philosophy


Approved, Thesis Committee:



Jennifer L. West, Professor, Committee Chair,
Bioengineering



Robert M. Raphael, Associate Professor,
Bioengineering



Sibani L. Biswal, Assistant Professor,
Chemical and Biomolecular Engineering

Houston, TX
June 2012

ABSTRACT

Three-Dimensional Biomimetic Patterning to Guide Cellular Migration and Organization

by

Joseph Charles Hoffmann

This thesis develops a novel photopatterning strategy for biomimetic scaffolds that enables spatial and biochemical control of engineered cellular architectures, such as the microvasculature. Intricate tools that allow for the three dimensional (3D) manipulation of biomaterial microenvironments will be critical for organizing cellular behavior, directing tissue formation, and ultimately, developing functional therapeutics to treat patients with critical organ failure. Poly(ethylene glycol) (PEG) based hydrogels, which without modification naturally resist protein adsorption and cellular adhesion, were utilized in combination with a two-photon laser patterning approach to covalently immobilize specific biomolecules in custom-designed, three-dimensional (3D) micropatterns. This technique, known as two-photon laser scanning lithography (TP-LSL), was shown in this thesis to possess the capability to micropattern multiple different biomolecules at modular concentrations into a single hydrogel microenvironment over a broad range of size scales with high 3D resolution. 3D cellular adhesion and migration were then explored in detail using time-lapse confocal microscopy to follow cells as they migrated along micropatterned tracks of various 3D size and composition. Further, in a valuable modification of TP-LSL, images from the endogenous microenvironment were converted into instructions to precisely direct the laser patterning of biomolecules within

PEG-based hydrogels. 3D images of endogenous microvasculature from various tissues were directly converted into 3D biomolecule patterns within the hydrogel scaffold with precise pattern fidelity. While tissue engineers have previously demonstrated the formation of vessels through the encapsulation of endothelial cells and pericyte precursor cells within PEG-based hydrogels, the vessel structure had been random, uncoordinated, and therefore, ultimately non-functional. This thesis has utilized image guided TP-LSL to pattern biomolecules into a 3D structure that directs the organization of vessels to mimic that of the endogenous tissue vasculature. TP-LSL now stands as a valuable tool to control the microstructure of engineered cellular architectures, thereby providing a critical step in the development of cellularized scaffolds into functional tissues. Ultimately, this thesis develops new technologies that advance the field of regenerative medicine towards the goal of engineering viable organs to therapeutically treat the 18 patients who die every day waiting on the organ transplant list.

ACKNOWLEDGEMENTS

A heartfelt thank you to my mentor Dr. Jennifer West for providing guidance and advice throughout this research project. I have always valued your opinion and appreciated your kindness and support the past 4 years. I would also like to thank my committee members Dr. Sibani Lisa Biswal and Dr. Robert Raphael for helpful discussion throughout the research process. Thank you to Dr. Mary Dickinson for new ideas and encouragement throughout our very productive collaborations.

A gigantic thank you to all of the graduate students and post-docs who have given me countless hours of technical and personal support over the past 4 years. It has been a joy to collaborate with Jim Culver and Dr. John Slater who always have great ideas but are even better people. Thank you to Dr. Michael Cuchiara and Dr. Maude Cuchiara for befriending me as a new graduate student, and for help and encouragement in a thousand different ways. Thank you to Dr. Melissa McHale for your perspective and friendly writing and presentation advice. Thank you to fellow graduate students and friends B.J. Gill, Andrew Coughlin, Steve Higbee, Christy Franco, Robert Langsner, Allan Henslee, and Clark Needham. I wouldn't have been able to complete this research project without you. And a special thank you to Dr. Jennifer Saik. You are brilliant, beautiful and the most caring person I know. And finally, thank you to Jerry, Mollie and Eric Hoffmann for supporting me throughout my entire life. I love you all.

This research was supported by generous grants from the National Institute of Health, including a Biotechnology Training Grant.

Table of Contents

Chapter 1: Introduction.....	1
1.1 The Need for Vascularization in Tissue Engineering	1
1.2 The Structure and Formation of the Microvasculature	3
1.3 The Angiogenic Process.....	6
1.4 Growth Factors and Signaling Molecules in Angiogenesis	7
1.5 Cell Sources in Vascular Tissue Engineering	10
1.6 Biomaterials in Microvascular Tissue Engineering	12
1.6.1 Natural Biomaterials	13
1.6.2 Synthetic Materials	15
1.6.3 Biosynthetic Hybrid Materials	15
1.7 Hydrogel Systems to Engineer the Microvasculature	16
1.8 Photopolymerization of Degradable Hydrogels.....	17
1.8.1 Poly(ethylene glycol) Diacrylate Hydrogels.....	20
1.9 Control of the Cellular Microenvironment	21
1.10 Cellular Responses in Three Dimensions	22
1.11 3D Printing.....	25
1.11.1 Direct-Write Bioprinting.....	26
1.11.2 Inkjet Bioprinting.....	30
1.11.3 Biological Laser Printing	33
1.12 Photopatterning	36
1.12.1 Layer by Layer Photolithography	37
1.12.2 Microfluidic Photopatterning.....	40
1.13 Shortcomings of Current 3D Scaffold Fabrication Technologies	42
1.14 Post-Gelation Photopatterning of PEG-based Hydrogels	43
1.15 Two-Photon Excitation	46

1.16 Two-Photon Laser Scanning Lithography	48
1.17 Summary	49
Chapter 2: Three-Dimensional Photolithographic Patterning of Multiple Bioactive Ligands in Poly(ethylene) Glycol Hydrogels	51
2.1 Introduction.....	51
2.2 Materials and Methods.....	54
2.2.1 Poly(ethylene glycol) Diacrylate (PEG-DA) Synthesis and Purification	54
2.2.2 Synthesis of Monoacrylate PEG-peptides and Degradable PEG-DA Hydrogels	55
2.2.3 Fluorescent Tagging of Monoacrylate PEG-peptides.....	56
2.2.4 PEG-DA Hydrogel Fabrication.....	57
2.2.5 Design of 3D Patterns of Fluorescent Monoacrylate PEG-RGDS.....	58
2.2.6 Patterning PEG-RGDS using Two-Photon Laser Scanning Lithography.....	59
2.2.7 Patterning PEG-RGDS and PEG-CS-1 within a PEG-PQ Hydrogel.....	60
2.3 Results.....	61
2.3.1 Fabrication of Fluorescent RGDS Patterns of Varying Size.....	61
2.3.2 Axial Resolution of Fluorescent RGDS Patterning in PEG-DA Hydrogels.....	62
2.3.3 Demonstration of the Three-Dimensionality of TP-LSL Patterns	63
2.3.4 Controlling RGDS Concentration with Laser Scan Speed and Intensity.....	64
2.3.5 Patterning Multiple Fluorescent RGDS Variants.....	66
2.3.6 Patterning Different Bioactive Peptides within a Degradable Hydrogel Microenvironment	68
2.4 Discussion	69
2.5 Conclusion	73
Chapter 3: Quantitative Investigation of Cell Migration in PEG-Based Hydrogels using Two-photon Laser Scanning Lithography	75
3.1 Introduction.....	75

3.2 Materials and Methods.....	80
3.2.1 Synthesis of Acrylate-PEG-Derivatives	80
3.2.2 Cell Maintenance	81
3.2.3 Ninhydrin Assay	81
3.2.4 Fabrication of PEG-RGDS Patterns to Guide 2D Cell Migration	82
3.2.5 Seeding and Visualization of HT1080s on 2D PEG-RGDS Surface Patterns	84
3.2.6 Fabrication of PEG-RGDS Patterns to Guide 3D Cell Migration	85
3.2.7 Guiding Cell Migration into 3D PEG-RGDS Micropatterns.....	86
3.2.8 Staining Nuclei and F-Actin to Visualize Cell Structure.....	88
3.2.9 Analysis of Cell Migration.....	89
3.3 Results.....	91
3.3.1 Quantification of PEG-RGDS Concentration in TP-LSL Patterned Hydrogels	91
3.3.2 Comparing 2D and 3D Cell Migration using TP-LSL and PEG-Based Hydrogels.....	93
3.3.3 Controlling 2D and 3D Cell Migration with PEG-RGDS Patterns of Varying Size	98
3.3.4 Variation of PEG-RGDS Concentration to Manipulate Cell Migration	101
3.3.5 Cell Speed and Persistence within 3D Hydrogels Increase over Time	107
3.3.6 Hydrogel Composition Affects Leading Cell Displacement into Hydrogel	110
3.4 Discussion.....	112
3.5 Conclusion	117
Chapter 4: Three-Dimensional Biomimetic Patterning in Hydrogels to Guide Cellular	
Organization.....	119
4.1 Introduction.....	119
4.2 Materials and Methods.....	122
4.2.1 Mice	122
4.2.2 Retinal Imaging.....	122
4.2.3 Cerebral Cortex Imaging	123

4.2.4 Heart Imaging	123
4.2.5 Subependymal Zone Imaging	124
4.2.6 Synthesis and Fluorescent Labeling of PEG-IKVAV.....	124
4.2.7 Fabrication of PEG-PQ Hydrogel.....	125
4.2.8 Mosaic Reconstruction of Imaged Structures Using LSM ROIs	127
4.2.9 Image-Guided TP-LSL Patterning Methodology	127
4.2.10 Patterning the Endogenous SEZ Microenvironment with Multiple Peptides	129
4.2.11 Cell Maintenance	129
4.2.12 Encapsulation of HUVECs and 10T1/2s into Hydrogels.....	130
4.2.13 Patterning Cellularized Hydrogels.....	130
4.2.14 Immunohistochemistry on Cellularized Hydrogels	132
4.2.15 Demonstration of Cell Alignment with PEG-RGDS Pattern.....	133
4.3 Results.....	134
4.3.1 Development of Image-Guided TP-LSL Methodology	134
4.3.2 Three-Dimensional Patterning of Endogenous Vessel Features.....	138
4.3.3 Patterning Multiple Biochemical Features of a Complex Tissue	141
4.3.4 Engineering a Biomimetic Microvasculature	143
4.4 Discussion.....	150
4.5 Conclusion	152
Chapter 5: Conclusions and Future Directions	153
5.1 Thesis Summary and Conclusions	153
5.2 Future Directions	157
5.2.1 TP-LSL Patterning of Proteins.....	157
5.2.2 Cell Migration Under Various Patterned Conditions.....	158
5.2.3 Image-Guided TP-LSL for Tissue Engineering and Model Development	159
5.2.4 Engineering Functional Vascularized Tissues	160

5.2.5 Summary	161
Chapter 6: References	162
Chapter 7: Appendix	176
7.1 Description of Custom MATLAB Scripts	176
7.2 Custom MATLAB Scripts	176

List of Figures

Figure 1-1: Tissue Engineering Paradigm..	2
Figure 1-2: Microvasculature Formation	5
Figure 1-3: Effect of VEGF on Angiogenesis.	6
Figure 1-4: Capillary Structures using 10T1/2s and HUVECs.....	11
Figure 1-5: Vessel Formation on a Fibrin Matrix.	14
Figure 1-6: Endothelial Cell Tubules on a Bioynthetic Hybrid Scaffold.	16
Figure 1-7: Photoinitiators for Photopolymerizable Hydrogels.....	18
Figure 1-8: Fibroblast Migrating in Degradable Hydrogel.	20
Figure 1-9: 2D vs. 3D Cell Morphology and Migration	23
Figure 1-10: Direct-Write Bioprinting.....	26
Figure 1-11: Direct-Write Bioprinting Collagen Scaffolds with Microfluidic Channels.	27
Figure 1-12: Direct-Write Bioprinting of Cellularized Spheroids..	29
Figure 1-13: Inkjet Bioprinting	31
Figure 1-14: Microdrop Scaffold Fabrication using an Inkjet Bioprinter.	33
Figure 1-15: Biological Laser Printing Setup..	34
Figure 1-16: Multicolor Biological Laser Printing	36
Figure 1-17: Layer by Layer Photolithography	39
Figure 1-18: Microfluidic Photopatterning	41
Figure 1-19: Photolithography on PEG-DA Hydrogels.....	444
Figure 1-20: Two-Photon Excitation.	47
Figure 1-21: TP-LSL Methodology	48
Figure 2-1: Incorporation of Biomolecules into PEG-based Hydrogels.....	52
Figure 2-2: PEG-DA Synthesis.....	54
Figure 2-3: Synthesis of PEG-RGDS and PEG-PQ.....	56
Figure 2-4: Fluorescent Acrylate-PEG-RGDS Synthesis..	57

Figure 2-5: PEG-DA Hydrogel Formation.....	58
Figure 2-6: Fluorescent RGDS Patterns of Various Size.....	62
Figure 2-7: Axial Resolution of TP-LSL.....	63
Figure 2-8: 3D Micropatterns via TP-LSL.....	64
Figure 2-9: Controlling RGDS Concentration with Laser Scan Speed and Intensity.....	66
Figure 2-10: Patterning Multiple Fluorescent RGDS Variants.....	67
Figure 2-11: Patterning Multiple Fluorescent RGDSs Variants in 3D.....	68
Figure 2-12: Patterning RGDS and CS-1 in a Degradable PEG Hydrogel.....	69
Figure 3-1: Illustration of the Forces Involved in Cell Migration.....	76
Figure 3-2: Diagram of PEG-RGDS Pattern on Surface of PEG-DA Hydrogel.....	84
Figure 3-3: 3D Patterns of PEG-RGDS Vary in Width and Height.....	86
Figure 3-4: Guiding HT1080s into PEG-RGDS Micropatterns within PEG-PQ Hydrogels.....	88
Figure 3-5: Quantification of PEG-RGDS Concentration in TP-LSL Patterned Hydrogels.....	92
Figure 3-6: Differences in Cell Speed and Persistence between 2D and 3D Cell Migration.....	95
Figure 3-7: Differences in Cell Size and Shape between 2D and 3D Cell Migration.....	97
Figure 3-8: Guiding Cell Migration with PEG-RGDS Micropatterns of Varying Size.....	99
Figure 3-9: Cell Speed and Persistence as a Function of PEG-RGDS Concentration.....	102
Figure 3-10: PEG-RGDS Concentration Affects Cell Morphology on 2D PEG-DA Surfaces...	104
Figure 3-11: Leading Cell Displacement in 3D Micropatterns varies with PEG-RGDS Concentration.....	107
Figure 3-13: Leading Cell Displacement in 3D Micropatterns Varies with PEG-PQ Hydrogel Composition.....	111
Figure 4-1: Tubule Networks in PEG-Based Hydrogels.....	120
Figure 4-2: Fabrication Methodology for Immobilized PEG-PQ Hydrogels.....	126
Figure 4-3: Methodology for Patterning Cellularized Hydrogels to Guide Tubule Formation...	132
Figure 4-4: Image-Guided TP-LSL Methodology.....	137

Figure 4-5: 3D Patterning to Recapitulate Multiple Tissue Types..	139
Figure 4-6: Lateral and Axial Fidelity of the 3D Patterning Process.....	140
Figure 4-7: Recapitulating the Subependymal Zone Vascular Niche Microenvironment.	142
Figure 4-8: Guiding Vascular Network Formation in Cellularized Hydrogels.....	145
Figure 4-9: Guiding Vessel Network Formation to Mimic the Vasculature from the Neural Stem Cell Niche..	147
Figure 4-10: Investigating the Development of Guided Vessel Networks	149

List of Tables

Table 1-1: Pros and Cons of 3D Microfabrication Technologies.....43

List of Equations

Equation 3-1: Cell Migration Speed.....	90
Equation 3-2: Cell Persistence.....	90
Equation 3-3: Cell Migration Ratio.....	90
Equation 3-4: Cell Circularity.....	90

Chapter 1: Introduction

1.1 The Need for Vascularization in Tissue Engineering

In the United States alone over 112,000 patients await life-saving organ transplants at any given moment¹. Alarming, the number of people on the waiting list continues to climb at a rate of over 300 additional patients every month, while 18 patients die every day waiting for an available donor¹. The field of tissue engineering seeks to find medical solutions for these patients through the application of biological and engineering principles to develop therapeutics that restore, maintain, or enhance the functions of failing tissues and organs². The longstanding paradigm of tissue engineering, as seen in Figure 1-1, combines the utilization of a biomaterial scaffold with cells and bioactive signals to design and fabricate a functional tissue. Several tissue engineering products have successfully implemented this strategy and are currently commercially available. For example, at least 13 different products have been brought to market that utilize cells and scaffolds to provide an engineered skin replacement therapeutic³. Additionally, implementation of tissue engineered strategies for the cornea⁴, bronchus airway⁵, bladder⁶, and cartilage⁷ have had at least some clinical success.

While these accomplishments are significant, the broad scale clinical success of tissue engineering applications has thus far been limited to simple tissues with few complex microstructures. For example, all of the tissue engineering products currently on the market have focused on thin, avascular tissues in which oxygen and nutrients diffuse throughout the tissue constructs to sustain cellular viability. When attempting to construct thicker, more complex tissues such as those in the heart, lungs, kidney and liver, cells

more than several hundred microns from the nearest capillary have been shown to suffer from hypoxia and subsequent cell death⁸. In order to engineer more complex tissues and organs, it will be necessary, therefore, to form a microvasculature that allows for sufficient gas exchange and nutrient supply to sustain high cell viability. Further, since the specific microstructure of endogenous vascular networks relates directly to the ability of a tissue to function properly⁹, it will be necessary to precisely control the density and spatial orientation of capillaries within biomaterial scaffolds.

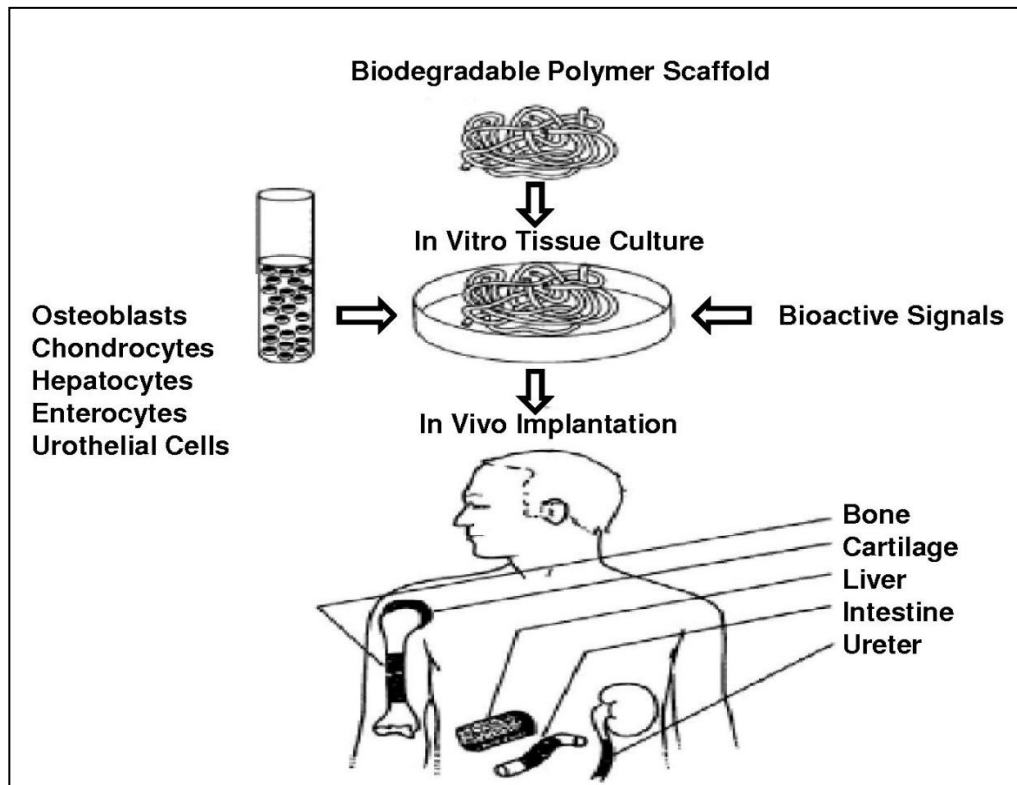


Figure 1-1: Tissue Engineering Paradigm. Chosen cell types are combined with bioactive signals and a biodegradable scaffold in an *in vitro* culture system with the hope of producing functional engineered tissue such as bone, cartilage, liver, intestine, or ureter. Adapted from Langer and Vacanti².

With this goal in mind, numerous biomaterial scaffolding approaches have been combined with various cell types and bioactive signals to promote the growth of blood vessel-like structures. Further, an array of microfabrication technologies have been developed in order to manipulate scaffolding materials to better mimic the chemical and structural microenvironment of naturally vascularized tissues.

This chapter first examines the structure of the microvasculature and the process of angiogenesis that occurs naturally in the body, including a discussion of the associated bioactive signals and growth factors. Current approaches to forming cell-based vessel structures are then investigated including analysis of various biomaterials, cell sources, and *in vivo* angiogenic assays. Finally, this chapter focuses on approaches to fabricate and pattern 3D biomaterial scaffolds on the microscale, with an emphasis on applications in tissue engineering. Together, this discussion lays a foundation of knowledge towards the fabrication of functional, engineered vascularized tissues. This thesis then significantly builds upon this knowledge base through the development and application of a 3D photolithographic patterning technology to probe 3D cellular interactions and to recapitulate endogenous microvascular networks using tissue engineered scaffolds. Overall, the contributions set forth in this thesis provide a new toolset to answer difficult questions in both cell biology and regenerative medicine, and move the field one step closer to achieving life saving therapeutics for those in need of organ transplants.

1.2 The Structure and Formation of the Microvasculature

A working knowledge of the structure and formation of the physiological microvasculature system is required to biomimetically engineer functional, vascularized tissue constructs. Capillaries that make up the microvasculature consist of an endothelial

cell layer, a deposited extracellular matrix basal membrane, and a single layer of supporting pericyte cells. The endothelial cells adhere strongly together to form thrombo-resistant, cylindrical tubules that serve to modulate blood flow, leukocyte interactions and vascular permeability⁸. Pericytes envelop the endothelial cell wall with many long, cytoplasmic appendages, essentially stabilizing the endothelial cells with focal contacts around the perimeter of the tubules¹⁰. Endothelial cells and pericytes then form a variety of junctions and adhesions to both each other and the deposited basement membrane. These junctions and adhesions are critical for both stabilization and regulation of the mature microvasculature¹⁰. The ratio of pericytes to endothelial cells in the microvasculature is linked directly to the permeability of the vessels, and thus, the highest ratios are found in the highly impermeable vasculature of the retina and brain¹¹.

There are two main mechanisms by which new vessels are formed – namely vasculogenesis, in which vessels assemble *de novo*, and angiogenesis, in which vessels sprout from pre-existing vessels (Figure 1-2)⁸. Vasculogenesis occurs through the differentiation of mesodermal cells first to angioblasts and then eventually into endothelial cells⁸. Newly differentiated endothelial cells are then organized into a capillary plexus of tubules⁸. Contrastingly, angiogenesis proceeds through the growth factor-dependent sprouting of new endothelial cell stalks from existing vessels. Both angiogenic and vasculogenic principles will likely be required to engineer a functional vascularized tissue. In this thesis, the vasculogenic pathway was principally utilized to examine vessel formation in biomaterial scaffolds. Specifically, endothelial cells and pericytes encapsulated within a biodegradable biomaterial are shown to self-assemble and form endothelial cell tubules with supporting pericytic cells lining the exterior in a

process similar to vasculogenesis. Recently, the line between angiogenesis and vasculogenesis has become blurred and many of the cell processes and signaling pathways are now thought to overlap between the two. While vasculogenesis was originally believed to be limited to fetal development, it has become clear that endothelial progenitor cells migrate and form basic vascular structures within adults¹². Additionally, angiogenesis has been observed in the developing fetus¹². An in depth understanding of this concurrent assembly system will be critical to the fabrication of functional vascular tissue engineering constructs.

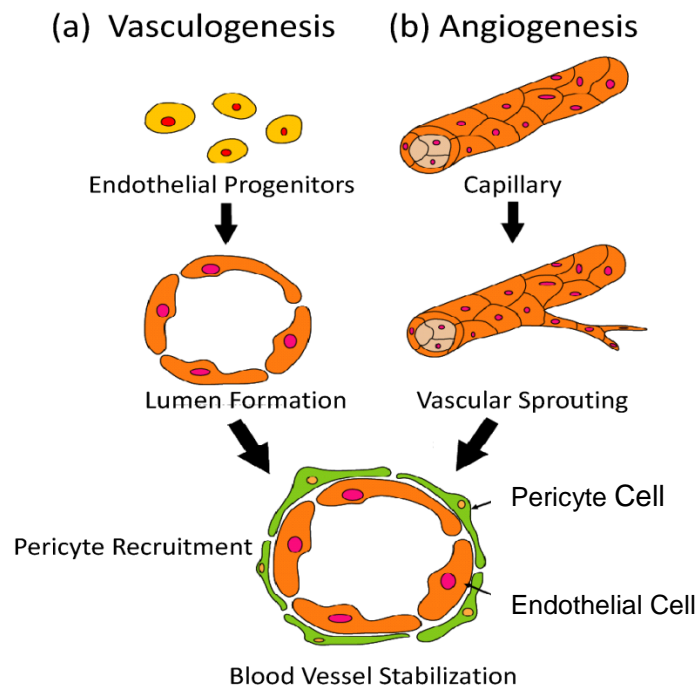


Figure 1-2: Microvasculature Formation. The two mechanisms by which new microvasculature forms are (a) vasculogenesis, where endothelial progenitors are organized into endothelial cell tubules, and (b) angiogenesis, where new endothelial cell tubules sprout from existing vasculature. Both of these mechanisms are followed by pericyte recruitment to stabilize the vessel structure. Adapted from Moon and West⁸.

1.3 The Angiogenic Process

The angiogenic process begins with the activation of selected endothelial cells and the subsequent release of proteolytic enzymes, known as matrix metalloproteinases (MMPs), by these cells to degrade the nearby extracellular matrix environment. Specifically, MMP-2 and MMP-9 have been shown to be critical in the degradation of ECM proteins during angiogenesis¹³. The activated endothelial cells, known as tip cells, begin extending long filopodia and migrating into the interstitial space as they follow an increasing gradient of angiogenic growth factors, principally vascular endothelial growth factor A (VEGF)¹⁴. Tip cells are followed by a cord of endothelial cells known as stalk cells, which display fewer filopodia and are less exploratory in nature (Figure 1-3)¹⁵.

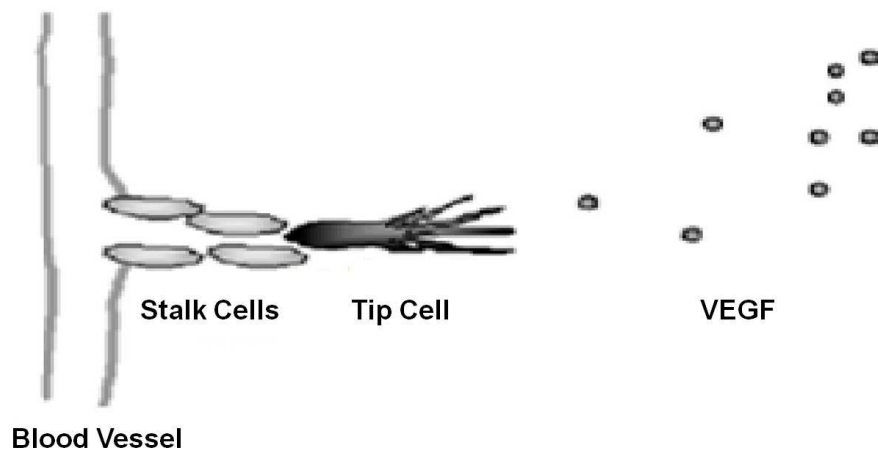


Figure 1-3: Effect of VEGF on Angiogenesis. The tip cell extends long filopodia and migrates down a VEGF gradient. Endothelial stalk cells proliferate and migrate behind the tip cell. Adapted from Karamyshiva *et al.*¹⁵

As they migrate, endothelial stalk cells begin to form vacuoles via pinocytosis and phagocytosis, with these vacuoles eventually coalescing to form a long, hollow lumen within endothelial cells¹⁶. When tip cells reach their target, such as another sprout of an adjacent capillary, the endothelial cells are signaled to suppress their motile, explorative behavior¹⁷. The subsequent formation of a lumen and the onset of blood flow helps to stabilize new vessel connections, as an increased oxygen supply down regulates angiogenesis growth factors such as VEGF¹⁷. As endothelial cells stabilize, chemotactically recruited pericytes begin to arrive and synthesize extracellular matrix for use in the basement membrane. Endothelial cells and pericytes form gap junctions that allow for signaling molecules to pass directly between the two cell bodies, ensuring a stable but adaptable microvascular system¹⁰.

1.4 Growth Factors and Signaling Molecules in Angiogenesis

The events of angiogenesis are directed by a host of growth factors and signaling molecules. The principal protein that guides angiogenesis is vascular endothelial growth factor (VEGF), which is produced primarily in response to hypoxia. There are more than 7 different proteins in the VEGF family¹⁸. Of these, VEGFA is the most common and is responsible for activating signal transduction pathways related to increased vascular permeability, as well as endothelial cell mitogenesis, migration, and survival. The VEGFA subgroup may be further divided into as many as 9 isoforms of varying amino acid length, depending on the splicing of the VEGFA gene during transcription¹⁸. These isoforms differ in their binding affinity for heparin. Specifically, VEGFA₁₈₉ and VEGFA₂₀₆ possess a high heparin binding affinity, VEGFA₁₂₁ has a very low heparin binding affinity, and VEGF₁₆₅ has an intermediate affinity for heparin¹⁵. Further,

VEGF₁₆₅ has been observed to possess the highest bioactivity of the different isoforms. The heparin binding properties of VEGFA are important as they determine whether the growth factor will accumulate in the proteoglycans of the extracellular matrix after secretion, or whether it will diffuse away. VEGFA's varying degree of binding to the extracellular matrix allows for the fabrication of complex gradients, which may be closely followed by migrating endothelial cell stalks (Figure 1-3).

The VEGF family binds 3 different endothelial cell receptors (VEGR1, VEGFR2, and VEGFR3), all of which belong to the transmembrane receptor tyrosine kinase family. VEGFA binds both VEGFR1 and VEGFR2, with VEGFR2 acting as the primary transduction pathway to induce migratory endothelial cells¹⁹, and VEGFR1 acting as an inhibitor²⁰. The third VEGF receptor is associated with the organization of lymphatic system endothelial cells and is primarily activated by VEGFC and VEGFD¹⁸.

VEGFA binding and activation have been observed to have different effects on endothelial tip cells and endothelial stalk cells. For example, upon exposure to the growth factor, tip cells extend large filopodia and become highly migratory while remaining non-proliferative; contrastingly, stalk cells extend fewer filopodia and proliferate significantly. The differences in the effect of VEGFA were partially explained by the presence of Delta like ligand 4 (Dll4) on tip cells, which paracrinously activates notch protein receptors on stalk cells¹⁴. The activation of notch receptors on stalk cells serves to down regulate the expression of VEGFR2, thereby producing the reduced migratory effect²¹.

In addition to VEGF receptors, a large class of membrane-bound tyrosine kinase signaling molecules, known as eph receptors, have been reported to be intricately

involved with the specification, activation, and migration of endothelial cells. Eph receptors are activated by a class of signaling molecules known as ephrins, and a variety of downstream bidirectional signaling events allow for eph/ephrin interaction to regulate both cell shape and cell movement²². While there are as many as 16 subclasses of eph receptors that are activated throughout the body²², it has been reported that the activation of the EphA2 receptor by ephrinA1 ligand binding is necessary for endothelial cell activation and is therefore a key governing component of angiogenesis²³.

A number of other growth factor interactions are important for the activation of endothelial cells. Fibroblast growth factor 2 (FGF-2) co-associates with the extracellular matrix (syndecans and glycosaminoglycans) and membrane-bound receptors on endothelial cells to further support the formation of new microvessels²⁴. Further, angiopoietins, such as ang-1 and ang-2, competitively bind tyrosine kinase receptor, Tie2, to induce chemotaxis of endothelial cells²⁵.

Growth factors are also responsible for coordinating the stabilizing aspects of angiogenesis. For example, platelet-derived growth factor BB (PDGF-BB) is produced by migrating endothelial cells and binds to platelet-derived growth factor receptor β on pericyte cells²⁶. The PDGF-BB gradient produced by the migratory endothelial cells chemotactically recruits pericytes to support the newly forming tubules. After pericytes have made junctions with endothelial cells, they begin releasing transforming growth factor β (TGF- β) and ang-1, which bind and stabilize endothelial cells²⁷.

Much remains to be elucidated regarding the complex interplay between the soluble protein signals regulating angiogenesis; however, the growth factors and

activation pathways discovered thus far are invaluable when designing a vascularized tissue engineering construct.

1.5 Cell Sources in Vascular Tissue Engineering

Another key element to a successful microvascular tissue engineering strategy is the selection of appropriate cell sources. To engineer the microvasculature, a cell source for both endothelial cells and pericytes will be required. A common source for endothelial cells is the human umbilical vein endothelial cell line (HUVEC). These cells have the ability to form vascular tubules and may be maintained in stable culture for up to eight passages²⁸. Differentiated pericytes have been historically difficult to isolate and maintain in culture, and therefore, multipotent mesenchymal precursor cells, such as those from the murine 10T1/2 cell line, may be used to act as mural cells to stabilize endothelial cell tubes and promote tubule anastomosis *in vivo* (Figure 1-4)²⁹. One may also consider using microvascular endothelial cells as opposed to macrovascular endothelial cells, when attempting to engineer vessels on the microscale.

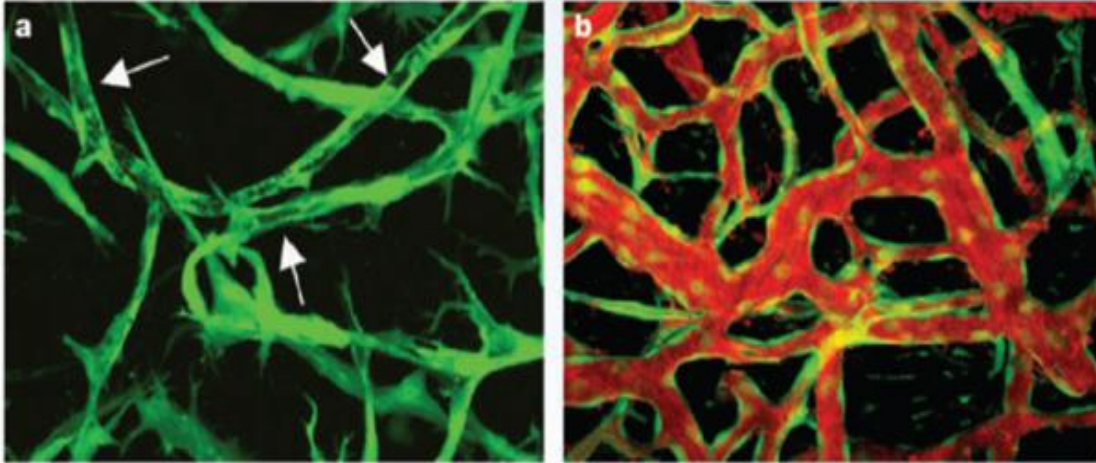


Figure 1-4: Capillary Structures using 10T1/2s and HUVECs. (a) Endothelial cells begin lumen formation (white arrows) 4 days post implantation in mice. (b) Vessels are fully lumenized and anastomosed with host vasculature at 12 days, as evidenced by perfused fluorescent dextran. Adapted from Koike *et al.*²⁹

These two cell types undergo distinct, morphogenetic programs to direct their phenotype, as microvascular endothelial cells generally produce capillaries which branch often, while macrovascular endothelial cells are generally used in the production of large tubes³⁰; therefore, it may be advantageous to choose cells suited to the specific vascular engineering application.

In addition to angiogenesis, vasculogenesis will be necessary for the engineering of stable vasculature. Endothelial progenitor cells have recently been isolated and present an attractive alternative to differentiated endothelial cells. Endothelial progenitor cells have been reported to instinctively home to sites of neovascularization and differentiate into endothelial cells upon arrival³¹. In recent work by Melero-Martin *et al.*, the co-implantation of mesenchymal stem cells and endothelial progenitor cells suspended in Matrigel into immunodeficient mice resulted in the formation of microvascular capillary networks that rapidly anastomosed with the host vessels³². The selection of these two cell types for vascular tissue engineering is advantageous due to their availability for

implantation into humans with minimal immunogenicity and donor site morbidity³². When selecting a vascular engineering cell source, one must also consider the relative ease of maintaining a cell line in culture for long periods of time, in terms of both workability and cost, especially for early *in vitro* research. HUVECs and 10T1/2 cells have each proven to be easily obtainable, cost effective, and to work well as a long term culture model. For these reasons, HUVECs and 10T1/2s were selected for much of the vascular tissue engineering work in this thesis. However, as cell isolation and culture techniques continue to advance, a shift is predicted toward other cell types, such as autogenous stem cells, that will allow for vascularization of tissue engineered constructs with greater therapeutic potential.

1.6 Biomaterials in Microvascular Tissue Engineering

While the selection of cell sources are a crucial component of tissue engineering, it is equally important to select the appropriate biomaterials. A variety of different types of biomaterials have been utilized as tissue engineering scaffolds to induce vascularization. The main purpose of any such tissue engineering scaffold is twofold. First, the scaffold must provide physical support for the vascularized tissue construct, and thus should have physical properties similar to those of soft tissues. Second, the scaffold must provide a means for the integration of cells and soluble signals to guide tissue formation³³. Biomaterials utilized for vascular scaffolds can be categorized into three distinct types: natural materials, synthetic materials, and biosynthetic hybrid materials. Each of these classes of materials has achieved a degree of success in the promotion of vascularization; each will be discussed to provide an overview of the current state of the art.

1.6.1 Natural Biomaterials

The most widely applied natural scaffolds used in the engineering of vessels are collagen and fibrin gels. Each of these materials possesses an innate angiogenic activity that may be controlled to promote tubule formation³⁴. Type I collagen, among the most abundant proteins in the human body, often takes the form of fibrils throughout the extracellular matrix. Human endothelial cells grown within collagen fiber gels are seen to organize into networks of capillary tubes with lumens³⁵. The innate angiogenic properties of collagen likely stem from the binding of the $\alpha_2\beta_1$ integrins of endothelial cells to the amino acid binding site GFPGER in collagen³⁴. The angiogenic properties of collagen may be further enhanced through the incorporation of growth factors, such as VEGF, via a homobifunctional cross-linker. Collagen implants with immobilized VEGF were observed to have a significant effect on the formation and in-growth of microvessels when an *in vivo* chorioallantoic membrane angiogenic (CAM) assay was performed³⁶. Fibrin gels also potently induce angiogenesis. For example, endothelial cells exposed to fibrin spontaneously form tubules with lumens within 6 – 12 hours of culture³⁷. Additionally, human microvascular endothelial cells were observed to organize into capillary like structures within a three dimensional fibrin matrix, and upon implantation *in vivo*, became stabilized by cells demonstrating pericyte morphology (Figure 1-4)³⁸.

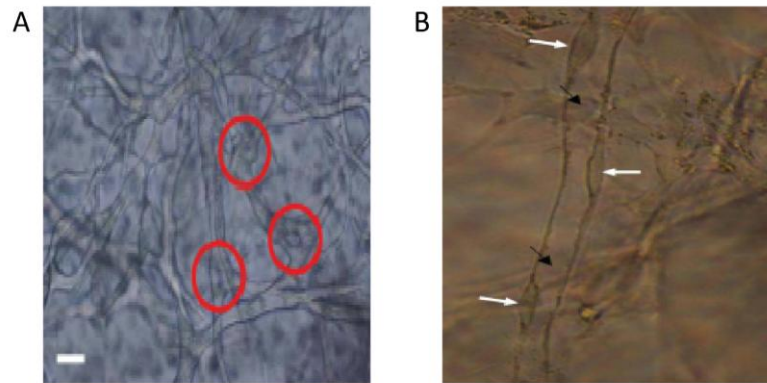


Figure 1-5: Vessel Formation on a Fibrin Matrix. Microvascular endothelial cells form tubules on three dimensional fibrin matrices. (A) Endothelial cell tubes anastomose with one another (red circles). (B) Endothelial cells form tubes with lumen (black arrows) with distinct nuclei (white arrows). Adapted from Montano *et al.*³⁸

Another naturally derived material that has been successfully utilized for vascular tissue engineering is gelled basement membrane extract, commercially known as Matrigel, Cultrex or EHS extract. These materials consist of a variety of extracellular matrix components, including collagen and fibrin. Endothelial cell tubule formation on these materials is rapid (within 6 hours) and reliable³⁹. These materials have additionally been used as an angiogenic assay for tubule formation to test proteins for pro-angiogenic and anti-angiogenic properties³⁹. While natural scaffolds have the advantage of presenting cells with complex, biochemical cues native to the physiological microenvironment, they have several important disadvantages. For example, natural scaffolds are often rapidly degraded and absorbed by the body, decreasing their potential for long term tissue engineering solutions. Additionally, natural scaffolds have the potential to cause an immune response, risk the transmittance of disease and possess a high degree of batch to batch variability that is difficult to control for³³. Synthetic scaffolds offer a safer alternative that may be readily produced and processed.

1.6.2 Synthetic Materials

Synthetic scaffolds coated with adsorbed extracellular matrix have been utilized for specialized tissue engineering applications. For example, endothelial cells have been cultured on poly(dimethyl siloxane) (PDMS) scaffolds⁴⁰ as well as poly(L)lactide and polycaprolactone copolymer⁴¹ and were seen to proliferate rapidly after protein adsorption. Synthetic materials offer greater control over mechanical properties and degradation rates than do natural materials, allowing for a better mimicry of tissues⁴². Poly(lactic acid) (PLA), poly(glycolic acid) (PGA), and their copolymer poly(lactic-co-glycolic acid) (PLGA) have been shown to possess a modulatable hydrolysis rate based on the molecular weight of the polymer, polymer crystallinity, and the ratio of glycolic acid to lactic acid⁴². Poly-4-hydroxybutyrate (P4HB) and polyhydroxyalkanoate (PHA) have been adjusted to possess elastomeric properties that simulate those of several soft tissues⁴². In general, however, these materials lack the specific biomolecular interactions necessary to guide endothelial cells and pericytes toward the formation of a complex microvasculature.

1.6.3 Biosynthetic Hybrid Materials

Biosynthetic hybrid scaffolding systems offer a modulatable, readily available system that allows for the custom tailoring of both physical and biochemical properties. The ability to precisely control such diverse sets of properties with very little batch-to-batch variability is the reason that a biosynthetic scaffold was ultimately selected for the research presented in this thesis. Many hybrid materials utilize the incorporation of extracellular matrix proteins or peptides, as well as other growth factors, to tailor their bioactivity for specific applications. For example, fibrin bioactivity has been incorporated

into Dacron materials to encourage neo-vascularization and enhanced wound healing⁴³. Additionally, a variety of poly(ethylene glycol) (PEG) based hydrogels have been synthesized that allow for the incorporation of bioactive proteins and peptides. Specifically, bioactivity has been incorporated into PEG-based hydrogels via several

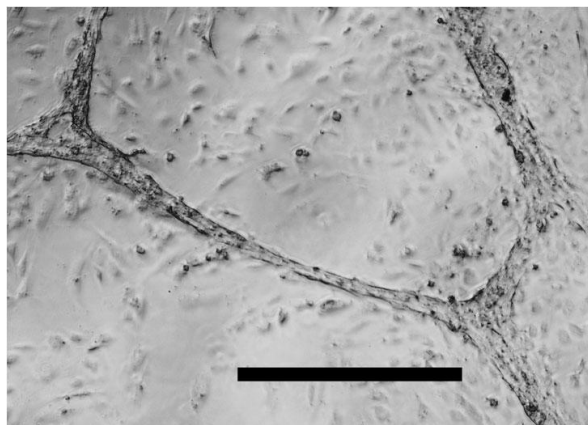


Figure 1-6: Endothelial Cell Tubules on a Biosynthetic Hybrid Scaffold. Branching endothelial tubule networks formed on the surface of PEG-based hydrogels modified with RGDS and VEGF. Scale bar 500 μm . Adapted from Leslie-Barbick *et al.*⁴⁷

methods including Michael type additions⁴⁴, thiol photocoupling with click chemistry⁴⁵, as well as the use of N-hydroxysuccinimide (NHS) leaving groups⁸. In vascular tissue engineering applications, work has been done to incorporate both RGDS (a cell adhesive peptide) and VEGF into PEG hydrogels via a Michael type addition, and researchers observed increased angiogenic activity alongside cellular in-growth *in vivo*⁴⁴. Further, other studies utilized NHS chemistry to incorporate the Ephrin A-1 binding domain⁴⁶, as well as VEGF⁴⁷ into acrylate based hydrogels to observe the formation of tubules by endothelial cells (Figure 1-6). Acrylate-based PEG hydrogels hold special advantages for the microfabrication of vascular structures, and will be discussed in detail later in this thesis.

1.7 Hydrogel Systems to Engineer the Microvasculature

Hydrogels have emerged as the leading biosynthetic hybrid material for vascular tissue engineering as they possess the innate advantages of both mimicking the

mechanical properties of soft tissues with high cellular compatibility, and also offer opportunities for biofunctionalization⁴². The porous and aqueous nature of hydrogels also allows for diffusion of cellular metabolic products, such as nutrients and wastes, a condition critical to high cellular viability. In recent years, hydrogels have been selected and modified with a variety of growth factors and cell adhesive ligands to produce cellular effects ranging from endothelial cell tubule formation⁴⁸, to guided neurite extension⁴⁹, and osteoblast differentiation and mineralization⁵⁰. Additionally, many biodegradable hydrogels have been utilized extensively in tissue engineering research with hopes of forming a fully biological construct after tissue formation⁴².

1.8 Photopolymerization of Degradable Hydrogels

While methods of hydrogel fabrication vary⁵¹, photopolymerization of hydrogels offers some distinct advantages for tissue engineering applications. Photopolymerizable hydrogels are generally fabricated via free radical induced cross linking of macromolecular precursors. The propagation of free radicals is generally created by the photocleavage of a photoinitiator upon light activation at the appropriate wavelength. Specifically, photoinitiators, such as benzoin derivatives, benziketals, acetophenone derivatives, and hydroxyalkylphenones, achieve free radical polymerization via the photocleavage of C-C, C-Cl, C-O, or C-S bonds when exposed to light⁵². When selecting a photoinitiator, one must consider the biocompatibility, water solubility, cytotoxicity, and excitation wavelength of the chosen molecule so that the photoinitiator best fits the needs of a particular application.

Several commonly used photoinitiators include 2, 2-dimethoxy-2-phenylacetophenone and 4-(2-hydroxyethoxy) phenyl-(2-propyl) ketone, which are

activated by ultraviolet light, and eosin Y and Camphorquinone, which are activated by visible light (Figure 1-7)⁵³. Photopolymerizable hydrogels have the advantage of a high level of spatial and temporal control during fabrication and offer opportunities to incorporate biomolecules for increased functionality⁵². Additionally, it has been shown in many cases that cells may be encapsulated in photopolymerizable hydrogels and retain high viability after macromolecular crosslinking. For example, osteoblasts retained high viability when photoencapsulated in ten percent poly(ethylene glycol) diacrylate (PEG-DA) hydrogel networks⁵⁴ and endothelial cells retained high viability when encapsulated in poly propylene fumarate-co-ethylene glycol networks⁵⁵. Some cell types, such as endothelial cells and primary cells, are especially sensitive to free radical damage from photoinitiators. For these scenarios, the photoinitiators 4-(2-hydroxyethoxy) phenyl-(2-propyl) ketone (Irgacure 2959) and eosin Y have been shown to have the lowest cytotoxicity and thus more success with cell encapsulation⁵³.

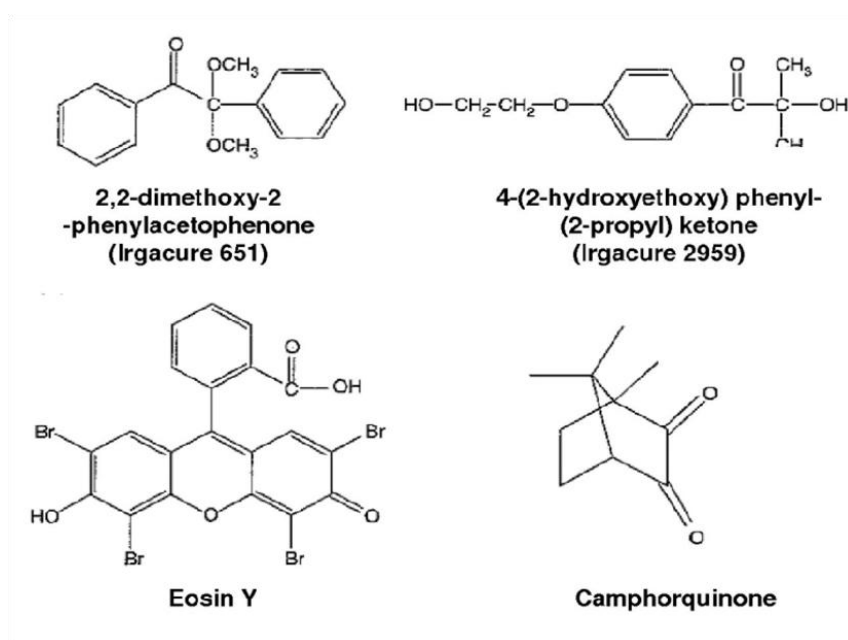


Figure 1-7: Photoinitiators for Photopolymerizable Hydrogels. The chemical structures of several common photoinitiators used to polymerize hydrogels are shown. Adapted from Bryant *et al.*⁵³

While photopolymerizable hydrogels are primarily composed of non-degradable carbon-carbon-based kinetic chains, degradable photopolymerizable materials have been synthesized through the incorporation of cleavable substrates into the polymeric backbone. Many photocrosslinkable hydrogels have been successfully rendered biodegradable including photopolymerizable polyanyhydrides, photocrosslinkable polyethylene glycol acrylates, photocrosslinkable polypropylene fumarates, photocrosslinkable polyvinyl alcohol, and photocrosslinkable polyamino esters⁵⁶. These photopolymerizable hydrogels normally breakdown through either hydrolytic or enzymatic mechanisms. Hydrogels designed to degrade by hydrolysis normally utilize poly(glycolic acid), poly(lactic acid) or poly(ϵ -caprolactone) in the macromer backbone. Upon polymerization, these materials will then degrade at modulatable rates upon placement in an aqueous environment. Enzymatically degradable gels may utilize natural substrates such as hyaluronic acid and chondroitin sulfate that are then naturally degradable by cells producing enzymes such hyaluronidase and chondroitinase⁵⁶. Alternatively, short, proteolytically labile peptide sequences that degrade upon exposure to specific proteases released by cells may be incorporated into the polymeric material. For example, Lee *et al.* incorporated a collagenase sensitive peptide sequence into the backbone of a photopolymerizable PEG-DA substrate to render it biodegradable. In this case, Bodipy fluorogenic dyes were also conjugated to the peptide, such that when the peptide was cleaved by collagenase, an increase in fluorescence intensity was observed in the hydrogel. When fibroblasts migrated through the hydrogel, they released collagenase that locally cleaved the peptide, thus causing an increase in fluorescence intensity and functionally allowing for the visualization of cell migration (Figure 1-8)⁵⁷.

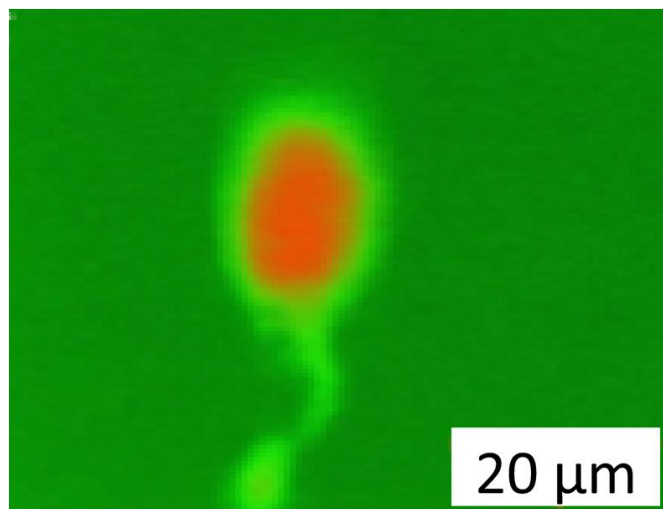


Figure 1-8: Fibroblast Migrating in Degradable Hydrogel. Confocal fluorescence image of a fibroblast migrating through degradable hydrogel with a fluorogenic MMP sensitive peptide linker in the polymer backbone. Adapted from Lee *et al.*⁵⁷

1.8.1 Poly(ethylene glycol) Diacrylate Hydrogels

Poly(ethylene glycol) diacrylate (PEG-DA) hydrogels have been utilized extensively in microvascular tissue engineering due to their well established biocompatibility, inherent resistance to protein adsorption, and ease of physical and chemical modification^{52,56}. Specifically, PEG-DA macromers are formed via the modification of PEG chains with an acrylate group at each terminus. These macromers rapidly polymerize upon exposure to light in the presence of an appropriate photoinitiator, forming water-based hydrogels. As mentioned previously, PEG-DA gels have further been rendered enzymatically degradable via the incorporation of short peptide sequences that are cleaved by migrating cells secreting matrix metalloproteinases (MMPs)^{47,57,58}.

Due to their inherent resistance to protein absorption, PEG-DA hydrogels act as a “blank slate” into which custom bioactivity may be incorporated. Specifically, with the

covalent attachment of acrylate-PEG-ligand moieties within the hydrogels, individually selected proteins and peptides may be utilized to guide cellular organization and differentiation within these materials^{59,60}.

A variety of proteins and peptide sequences have been incorporated into PEG-DA hydrogels. For example, cellular adhesive ligands such as the fibronectin-derived peptide sequence Arg-Gly-Asp-Ser (RGDS) have been added to acrylate based PEG hydrogels and shown to promote the cellular adhesion and migration of many cell types including fibroblasts⁶¹. Other sequences, such as the elastin-derived peptide Val-Ala-Pro-Gly (VAPG) for smooth muscles cells⁶² and laminin-derived Tyr-Ile-Gly-Ser-Arg (YIGSR) for endothelial cells⁶³, have also been modified with a PEG-acrylate chain to promote cell-type specific adhesion within the hydrogels. Additionally, as discussed in Section 1.6.3, ephrin-A1⁴⁶ and VEGF⁴⁷ have each been incorporated into PEG-DA hydrogels, and have been observed to induce the formation of capillary-like tubules with diameters of 5-30 μm ⁴⁶. Overall, the acrylate-PEG-based hydrogel system provides a versatile, multifunctional material platform that this thesis utilizes to both explore core biological principles as well as to develop vascularized tissues constructs with regenerative medicine applications.

1.9 Control of the Cellular Microenvironment

In parallel with the development of multifunctional PEG hydrogels, micropatterning techniques have emerged in order to fabricate physical and biochemical structures that better mimic the cellular microenvironment. For example, micro-contact printing utilizes elastomeric stamps to immobilize distinct patterns of adhesive molecules, such as fibronectin, onto biomaterial substrates⁶⁴. Further, photolithographic

techniques employ high resolution photomasks to spatially control photochemical reactions that immobilize bioactive proteins and peptides onto biocompatible material surfaces⁶⁵. These methods have proven highly useful in the study of complex cellular interactions as they allow for the control of cell morphology and the organization of cells into complex, pre-designed microstructures; however, these methods are primarily applicable to flat, two-dimensional surfaces, and therefore, fail to allow for the fabrication of three-dimensional biochemical structures to mimic the physiological microenvironment of the extracellular matrix.

1.10 Cellular Responses in Three Dimensions

Recent findings have shown that nearly all cell types require three-dimensional (3D) cues to produce a physiologically relevant cellular response⁶⁶. Specifically, researchers have observed dramatic differences in cellular attachment, morphology, migration, and proliferation between cells in 2D versus 3D environments. To understand the nuances of these differences, one must examine the fundamentals of cellular adhesion. Generally, cells utilize a class of heterodimeric proteins known as integrins to both bind to the extracellular matrix and to transduce information about the environment to the inside of the cell. To adhere to the matrix, the integrin contacts of a cell localize with one another as well as with a variety of other transduction proteins to form adhesion complexes. On a two-dimensional surface, cells form two distinct matrix contacts known as focal adhesions and fibrillar adhesions. Focal adhesions consist mostly of $\alpha_v\beta_3$ integrin, paxillin, vinculin, and focal adhesion kinase proteins and are primarily strong contacts formed at the periphery of cells. Fibrillar adhesions consist mostly of the $\alpha_5\beta_1$ integrin and tensin protein, form in the center of the cell, and align along fibronectin

fibers⁶⁷. In 2001, work by Cukierman *et al.* demonstrated that on a 3D substrate, $\alpha_5\beta_1$ integrin localized with paxillin, vinculin, and focal adhesion kinase to form a single type of adhesion, observed only in 3D, that was long, slender and aligned along fibronectin fibers⁶⁸. Cukierman went on to show that these novel adhesions resulted in a 1.5 fold increase in cellular migratory speed, a slender and less spread cellular morphology, and increased cellular attachment and proliferation when compared with cells cultured on a 2D surfaces with traditional adhesions (Figure 1-9)⁶⁸.

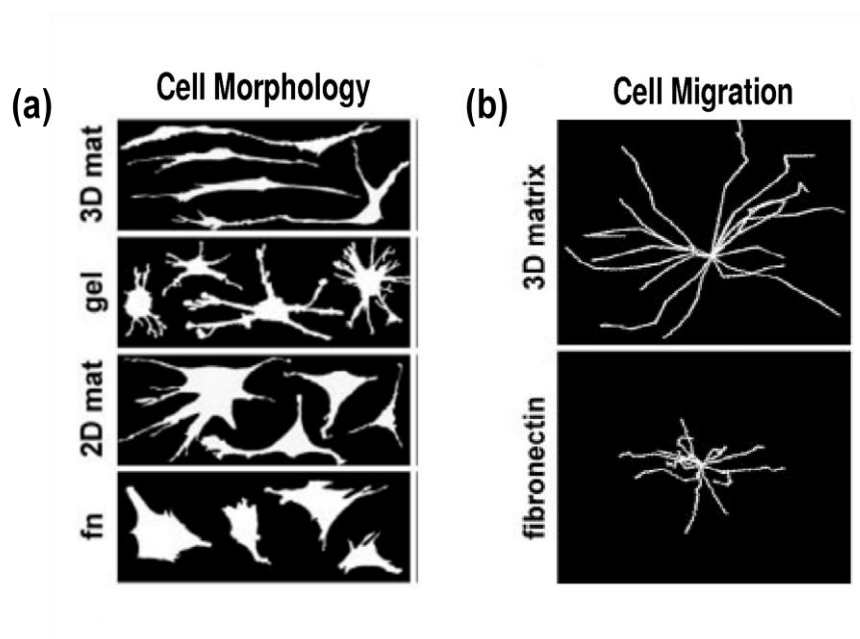


Figure 1-9: 2D vs. 3D Cell Morphology and Migration. (a) Cell morphology of fibroblasts on 3D extracellular matrix, compared to cell morphology on various 2D substrates including collagen (gel), a flattened 2D extracellular matrix (2D mat), and fibronectin (fn). (b) Cell migration tracks for fibroblasts within a 3D matrix compared with those on a fibronectin plate. Adapted from Cukierman *et al.*⁶⁸

Several researchers have gone on to study three-dimensional cell migration in greater detail. For example, Zaman *et al.* examined the interplay of matrix stiffness, matrix proteolysis, and adhesion molecules on cellular migration in three dimensions⁶⁹.

Recently, Zaman *et al.* demonstrated that as 3D Matrigel matrices were softened, human prostate carcinoma cells migrated at maximal speeds on lower concentrations of adhesive molecules⁶⁹. This migration trend is in direct contrast with two-dimensional migration studies and is likely explained by the forces a 3D matrix places on all cell surfaces, with fewer stiff surfaces serving as a better environment for matrix degradation, remodeling, and subsequent motility. Additionally, Dikovsky *et al.* used a series of fibrinogen PEG-DA hydrogels of varying elastic modulus (10 – 700 Pa) and a MMP inhibitor in order to show that initial cell spreading and remodeling were highly dependent on the proteolytic susceptibility of the 3D matrix, while the state of cell compaction and later motility were directly tied to matrix elasticity⁷⁰.

Much remains to be elucidated regarding cellular migration in three-dimensional substrates. Since cells naturally undergoing angiogenesis assemble into tissues within a three-dimensional extracellular matrix microenvironment, it follows that an in depth understanding of the migratory actions of cells in 3D will be critical to a successful tissue engineering strategy. In this thesis, the development of new patterning tools allows for exploration into complex cellular migratory behavior within custom designed 3D hydrogel systems. First, however, the state of the art of 3D scaffold microfabrication and micropatterning technologies will be reviewed to better understand the accomplishments and shortcomings of current approaches to mimic the 3D environments of cells and tissues. Specifically, various types of 3D printing and photolithography will be discussed in detail with an emphasis on progress thus far towards engineering complex biomimetic tissue structures.

1.11 3D Printing

Early 3D printing systems for tissue engineering were borrowed from the field of materials manufacturing and were composed of a print-head mounted on X-Y rails, a building platform with an axial elevator, and a powder dispensing roller. Scaffolds were fabricated by laying down a powder across the building platform, and then directing the print head to dispense a liquid binder in designed two-dimensional patterns. After axial adjustment, another layer of powder was applied, and bound in the areas where the binding liquid was deposited⁷¹. Using computer automated design software, a series of two-dimensional images were thereby translated into a 3D tissue engineering scaffold. In 2002, this type of 3D printing was utilized to pattern a scaffold with variable properties to better mimic the characteristics of both bone and cartilage⁷². Specifically, the top section of a scaffold was printed using poly(D,L,-lactide-co-glycolide) (PLGA) and L- poly lactic acid (PLA) at 90% porosity with staggered macroscopic channels to facilitate chondrocyte seeding and cartilage formation. The bottom portion of the same scaffold was printed into a cloverleaf shape using PLGA and calcium phosphate at 55% porosity to achieve strong mechanical properties and initiate bone growth. This 3D printing technology demonstrated varied control of porosity, material composition, physical structure and mechanical properties within a 3D biomaterial scaffold, with the goal of fabricating multifaceted materials for total joint replacement⁷². Excited by early success, engineers have since moved to 3D printing of hydrogel structures on the micron scale. Further, over the last 10 years, the term 3D printing has evolved and split to encompass at least three valuable yet distinct technologies now being utilized in the tissue engineering community. These technologies, known as direct-write bioprinting, inkjet bioprinting,

and biological laser printing will now each be discussed in turn, with an emphasis on recent successes in tissue engineering applications.

1.11.1 Direct-Write Bioprinting

Direct-write bioprinting involves the use of a three-dimensionally controlled actuator to extrude a liquid material, or bioink, through a dispensing pen in the form of a designed pattern (Figure 1-10a-b)^{73,74}. The pattern is subsequently crosslinked or gelled through the use of chemical reagents or environmental factors. 3D structures are then built through an additive layer-by-layer process (Figure 1-10c). Direct-write bioprinting generally prints a continuous line of material extruded from the dispensing pen and the resolution is highly dependent on the printing material, including its viscosity, as well as crosslinking or gelling conditions⁷⁴.

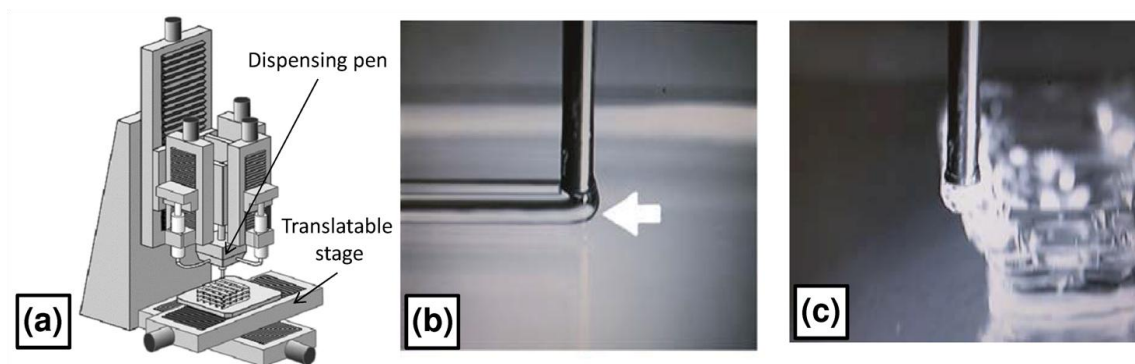


Figure 1-10: Direct-Write Bioprinting. (a) A schematic of a direct-write bioprinting apparatus. Biomaterials are dispensed by a pen onto a translatable stage to form a scaffold. Adapted from Lewis *et al.*⁷³ (b) Close up image of a dispensing pen extruding the first layer of a hydrogel biomaterial onto a surface (arrow is leading edge). (c) After curing the first layer, additional layers are deposited to form 3D structures. Adapted from Chang *et al.*⁷⁴

Some direct-write bioprinters are capable of printing 3D structures as small as 5 μm and as large as many millimeters^{74,75}. Direct-write bioprinting was recently utilized to print 3D collagen scaffolds containing microfluidic channels⁷⁶. Specifically, the scaffold was fabricated by first printing collagen into a designed pattern and then crosslinking it with nebulized sodium bicarbonate using a custom designed 3D bioprinter (Figure 1-11a)⁷⁶.

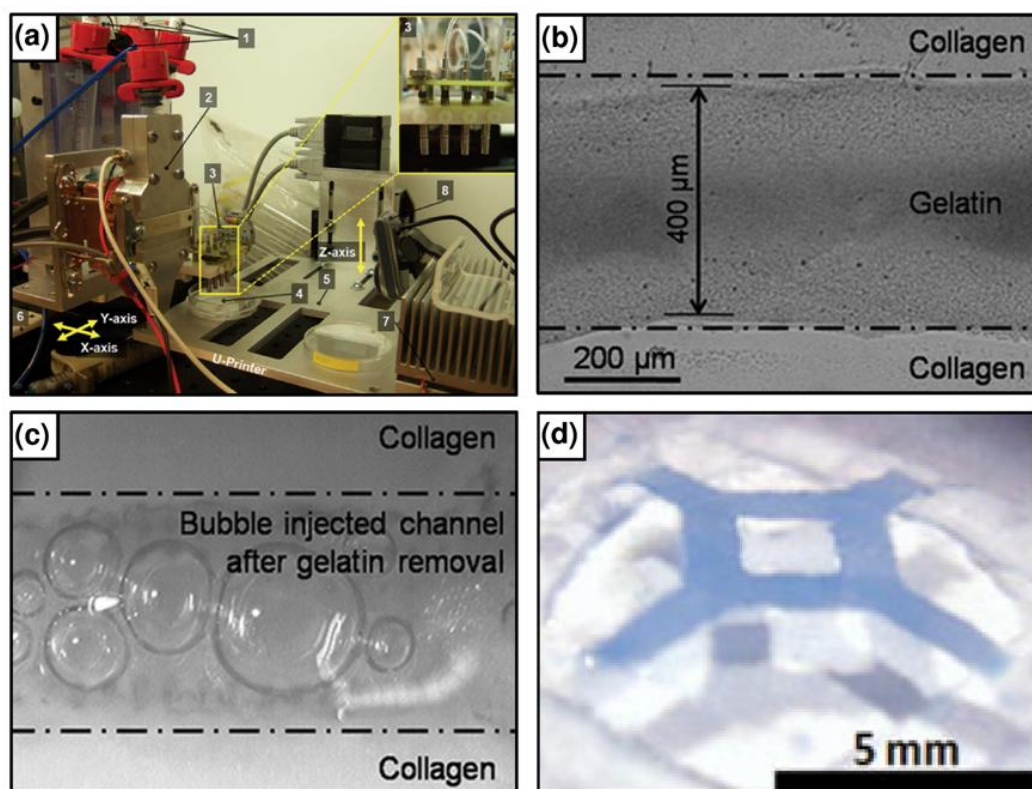


Figure 1-11: Direct-Write Bioprinting Collagen Scaffolds with Microfluidic Channels. (a) A photograph of the custom designed 3D bioprinter including [1] a 4-channel syringe unit, [2] a heating and cooling element, [3] a 4-channel dispensing unit, [4] a target substrate, and [5] a vertical and [6] horizontal stage. (b) This bioprinter was utilized to fabricate 3D collagen scaffolds containing 400 μm wide 3D channels of gelatin. (c) The channels became hollow when heated and washed thus allowing for air bubbles to be injected into them. (d) Perfusion of blue microspheres in PBS was demonstrated in a rotary pattern of hollow channels within a collagen scaffold. Adapted from Lee *et al.*⁷⁶

Heated gelatin was then printed into the regions of the scaffold where collagen was not present, and crosslinked via temperature cooling. Using a layer by layer method, 400 μm wide 3D channels of gelatin were patterned within a collagen scaffold (Figure 1-11b)⁷⁶. The scaffold was then heated to liquefy and rinse away the gelatin, leaving hollow channels behind (Figure 1-11c)⁷⁶. A complex rotary pattern of hollow channels was also fabricated and perfused with blue microspheres in phosphate buffered saline (PBS) to demonstrate mechanical integrity (Figure 1-11d)⁷⁶. When dermal fibroblasts were seeded on this scaffold, the micropatterned channels allowed for better nutrient transport and increased cell viability as opposed to scaffolds without channels⁷⁶.

In addition to collagen and gelatin, direct-write bioprinting has been demonstrated using a wide variety of biomaterials including agarose⁷⁷, alginate⁷⁸, pluronic F127⁷⁵, Matrigel⁷⁹, a hyaluronan-gelatin copolymer⁸⁰, as well as a synthetic copolymer containing poly(ethylene glycol)⁸¹. The direct-write bioprinting technique has also shown the ability to incorporate highly viable cells⁷⁴, thus allowing for the spatially controlled formation of 3D cellularized scaffolds. For example, rat microvascular cells were incorporated into a collagen bioink, and a multilayer 3D structure was printed with cell viability over 90 percent⁸².

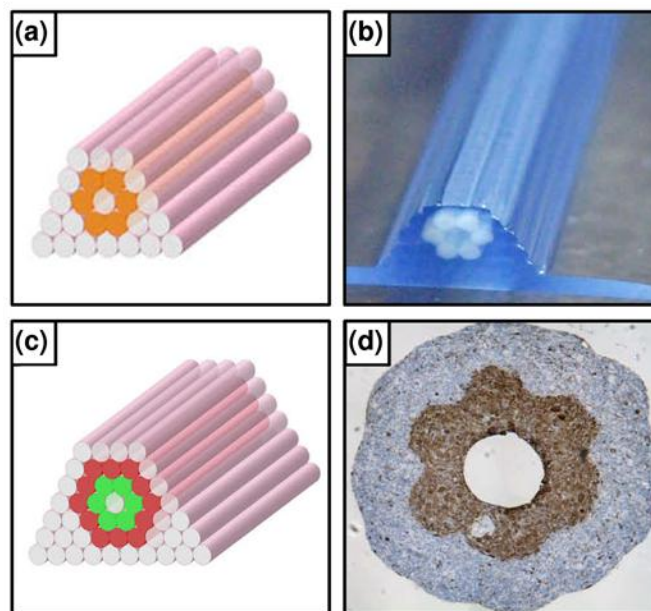


Figure 1-12: Direct-Write Bioprinting of Cellularized Spheroids. (a) Design template to form hollow tubules from cylindrical fused cell spheroids (orange) and non-adhesive agarose rods. (b) Printed construct with non-adhesive agarose rods in blue and cell spheroids in white. (c) Design template to form double layered vascular wall with vascular smooth muscle cells cylinders (green) and fibroblast cells (red). (d) Histological examination of double layered vascular wall. The brown staining (smooth muscle α -actin) and blue staining (hematoxylin) are used to clearly differentiate the two cellular layers. Adapted from Norotte *et al*⁷⁷.

Researchers have even utilized direct-write bioprinting in a scaffoldless approach in which cylinders composed only of fused cell spheroids were three-dimensionally positioned in between non-adhesive rods to form perusable vessel-like tubules of various designed geometries (Figure 1-12a-b)⁷⁷. The same group was then able to combine both vascular smooth muscle cell cylinders and fibroblast cylinders in order to fabricate a multiwalled structure that mimicked the multilayer structures that occur naturally in blood vessels (Figure 1-12c-d)⁷⁷. Most recently, direct-write bioprinting has used multiple cell types to form different types of tissues when implanted *in vivo*⁷⁹. Specifically, endothelial progenitor cells encapsulated in Matrigel in one section of a printed scaffold were seen to form vessels containing red blood cells after a 6 week

implantation in immunodeficient mice. A different section of the same scaffold was printed with mesenchymal stem cells and calcium phosphate micro particles in Matrigel and demonstrated significant bone formation after a six week implantation⁷⁹.

1.11.2 Inkjet Bioprinting

Inkjet bioprinting involves the use of modified commercial printers to dispense cells or cell-biomaterial mixtures in a precise, micropatterned manner⁸³. Specifically, commercial print heads are modified with needles or nozzles and commercial printer ink is replaced with bioink consisting of living cells in solution (Figure 1-13a)⁸⁴. Generally, printers are exposed to UV light and modified cartridges are wiped down with ethanol in order to provide cells with a sterile environment. Desktop thermal printers are most common in inkjet bioprinting and operate by using a heating element to induce a small liquid bubble that then forces a precise amount of liquid through a series of nozzles⁸³, each of which is about 50 μm in diameter⁸⁵ (Figure 1-13b). When the heat pulse is removed, the bubble collapses, and the subsequent loss of volume draws more fluid into the chamber. The inkjet bioprinting process proceeds via repeated generation of microdroplets of bioink that are subsequently deposited onto a biomaterial substrate, or biopaper, in computer-specified patterns. In one of the first examples of inkjet printing of mammalian cells, Chinese hamster ovary (CHO) cells were deposited onto collagen or agarose hydrogels into distinct patterns with less than 10% loss of cell viability⁸⁶. Researchers have also used ink jet printers to pattern both viable cells and a biomaterial scaffold. For example, in one recent study, a solution containing thrombin and human microvascular endothelial cells (HMECs) was utilized as bioink and printed onto a fibrinogen coated coverslip⁸⁷. After incubation at 37°C for 20 minutes, a mechanically

stable fibrin scaffold with HMECs had formed. 100 μm diameter fibers were printed and the HMECs were seen to coalesce and form high integrity microvascular tubules aligned along the fibrin scaffolds after 21 days in culture⁸⁷.

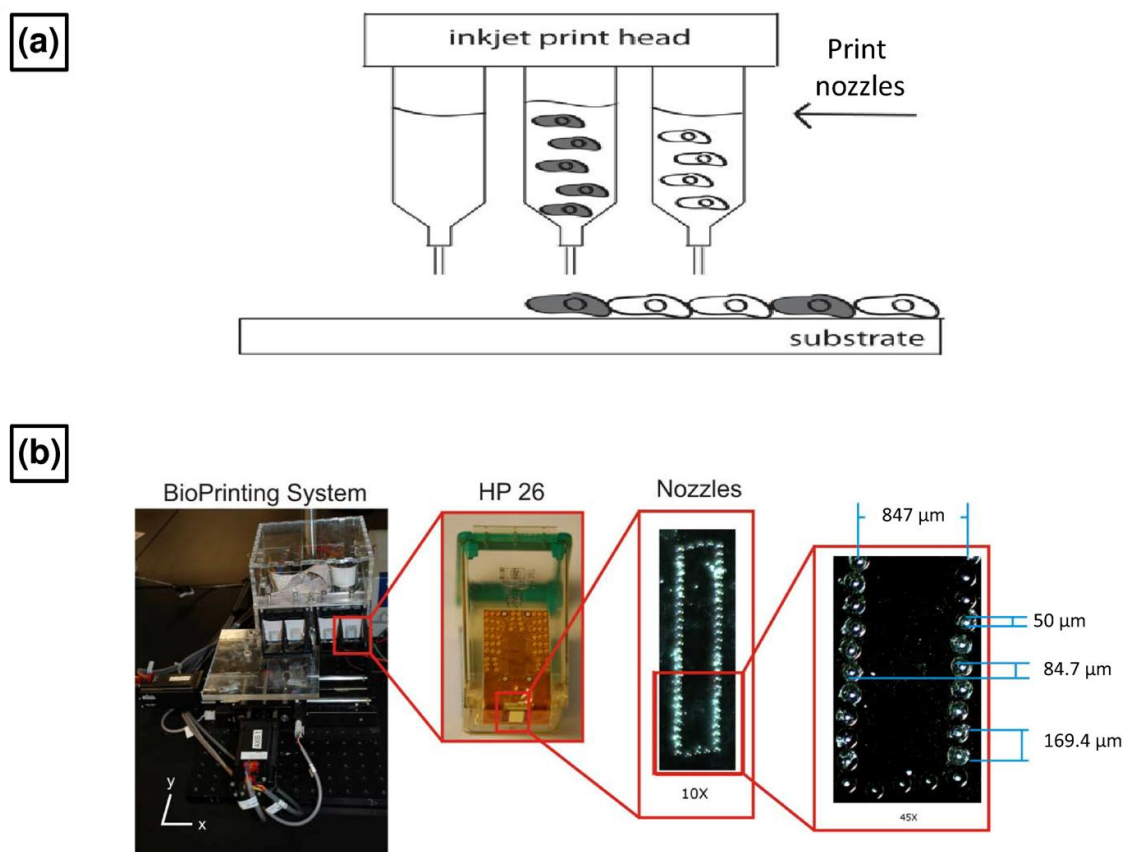


Figure 1-13: Inkjet Bioprinting. (a) Schematic of inkjet bioprinting in which an inkjet print head containing nozzles dispenses cells onto a biomaterial substrate. Adapted from Silke *et al.*⁸⁴ (b) An inkjet bioprinting system is pictured. This system uses an HP26 ink cartridge with 50 nozzles, each of which is 50 μm in width. Adapted from Pepper *et al.*⁸⁵

Three-dimensionality in most inkjet bioprinting systems has been achieved by stacking of multiple biomaterial substrates. For example, 5 sequential layers of fibrin were printed in a layer by layer manner, with each layer containing neuronal cells and possessing a thickness of about 50 μm ⁸⁶. While promising for some applications, automated and precise 3D control using inkjet bioprinting has been limited because when

printing a liquid material on a hydrogel substrate, the liquid spreads out, thus becoming thin and limiting pattern resolution to hundreds of micrometers. Researchers have overcome this obstacle using modified inkjet printers to pattern quick gelling alginate droplets⁸⁸. Alginate forms a hydrogel almost immediately when exposed to calcium, and therefore, droplets can be crosslinked before spreading occurs, thus greatly increasing resolution and 3D patterning capabilities.

For example, alginate microdroplets were recently printed onto a gelatin substrate that contained calcium chloride⁸⁸. As the alginate droplets were printed, they were gelled rapidly as calcium ions diffused into them. Each gelled calcium droplet then acted as a building block to build 3D structures (Figure 1-14a). Researchers achieved excellent cell viability within the alginate droplets and a maximum resolution of under 3 μm . Using this technique, a bifurcating hollow microchannel, reminiscent of those seen in the microvasculature, was patterned (Figure 1-14b-c) and subsequently supported physiologic flow conditions without leaking⁸⁸. Finally, this research group demonstrated that this ink jet printing platform could be used to provide 3D structure to slower gelling, more biologically active materials by combining them with alginate. Specifically, alginate and collagen were mixed and structures were formed using the fast- gelling alginate process. The collagen was then allowed to slowly gel when heated. After collagen gelation, the alginate was removed via chelation, leaving behind a 3D collagen structure⁸⁸.

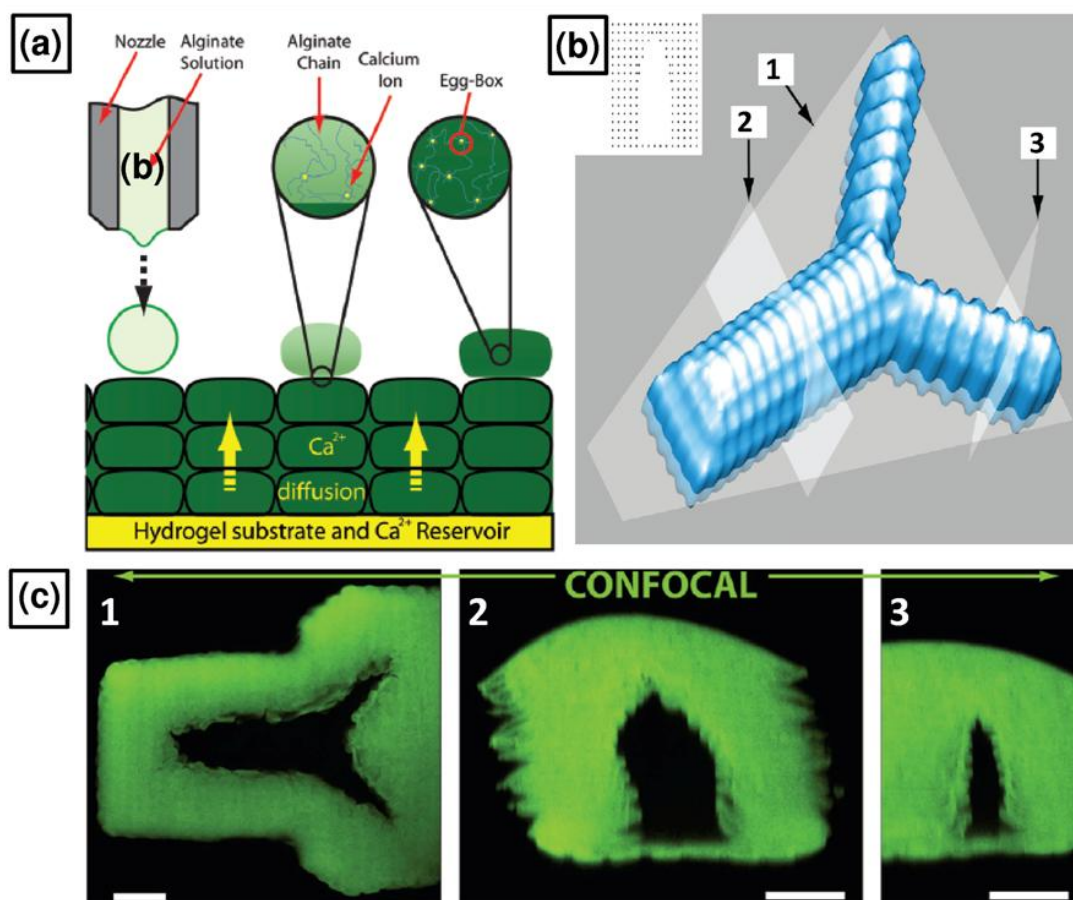


Figure 1-14: Microdrop Scaffold Fabrication using an Inkjet Bioprinter. (a) Alginate microdroplets are printed onto a gelatin hydrogel permeated with calcium chloride. Calcium ions diffuse upwards and rapidly crosslink the droplets, allowing for the formation of 3D structures. (b) Model of a bifurcating channel to be printed with indicated slices corresponding to confocal images below. Inset: model of droplets needed to form larger channel. (c) Confocal images of the crosslinked alginate channel with each image corresponding the indicated plane in the model above. All scale bars = 200 μm . Adapted from Pataky et al.⁸⁸

1.11.3 Biological Laser Printing

Biological laser printing (BioLP) has emerged as a parallel process to dictate the microstructure of cells on biomaterials. BioLP is a modified laser-induced forward transfer technique that involves the use of a high pulsed laser to transfer cells onto a

biomaterial substrate in a highly controlled manner. In this technology, a laser is focused on a target material consisting of a transparent mechanical support layer (glass or quartz), an energy conversion layer (gold or titanium), and a liquid transfer layer containing the cells to be printed (Figure 1-15)⁸³. The laser is specifically focused on the energy conversion layer, which absorbs the laser light and transmits it to the cell containing transfer material. This results in a jet of cell-containing material being transferred to a biomaterial substrate in the exact location of the laser pulse⁸³. The amount of material transferred per laser pulse is generally about 500 femtoliters⁸⁹, and the resulting resolution has been reported to be less than 5 μm ⁹⁰. The biomaterial substrate receiving surface is normally controlled by a CAD/CAM interface that allows for translation of the material and therefore the fabrication of patterned materials.

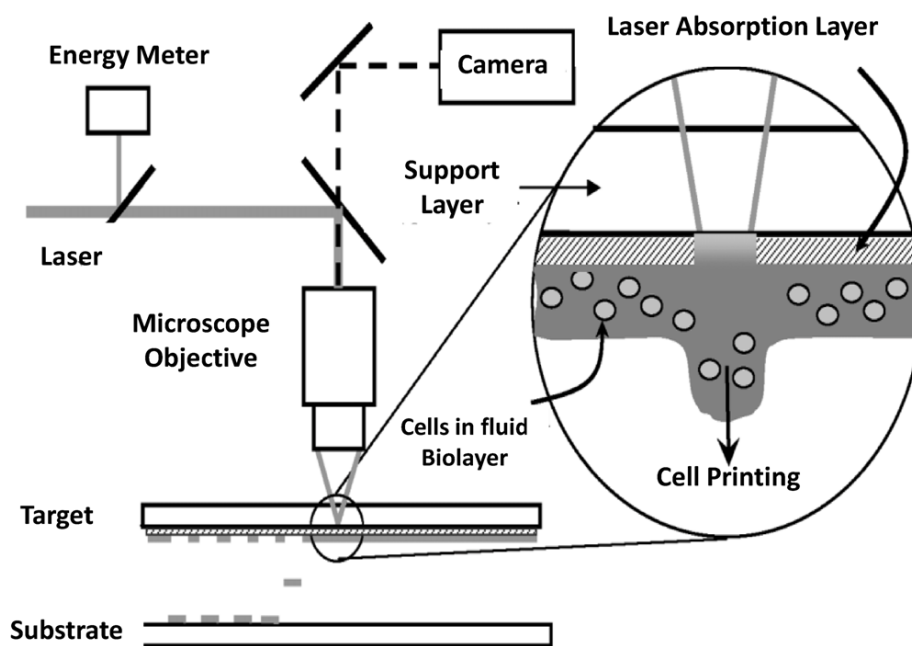


Figure 1-15: Biological Laser Printing Setup. A schematic of biological laser printing is depicted. The laser is focused on the laser absorption layer (also known as the energy conversion layer). Energy is transmitted to the cell-laden transfer layer which results in a jet of material being transferred to the biomaterial substrate⁸³.

Numerous cell types have been shown to survive this process with cell viability near 100 percent^{83,89,91,92}, and different kinds of cells have been deposited adjacent to one another⁹⁰ and in single cell arrays on biomaterial surfaces⁹¹. Recently, high-throughput BioLP systems have been designed that allow for the rapid printing of multiple different kinds of cells or biomaterials. For example, a "multi-color" BioLP system, was utilized to rapidly print alginate droplets, hydroxyapatite nanocrystals, and endothelial cells with high precision using the same automated printing system⁹³. This was achieved using a single infrared laser and a rotating carousel that could quickly change between printing materials⁹³. Multiple populations of endothelial cells were later printed into juxtaposed concentric patterns with high resolution between the cell types (Figure 1-16)⁹⁴. In moving towards more 3D constructs, a 500 μm thick fibrin scaffold was fabricated with BioLP by printing thrombin onto a fibrinogen biopaper⁹⁴. Specifically, a patterned array of fibrin fibers containing endothelial cells was printed with resolution comparable to the endogenous microvasculature. Using a 200 mm/s scan speed, a 4 cm^2 construct was micropatterned in just a few seconds⁹⁴.

BioLP has also been applied in a layer by layer method to fabricate thicker constructs closer to the size scale of naturally occurring tissues and organs. For example, in one study, human osteosarcoma cells were printed into a distinct patterns on a thin layer of basement membrane hydrogel (Matrigel)^{83,90}. A new Matrigel layer was then applied on top of top of the cells, and another distinct pattern of osteosarcoma cells was printed. Interestingly, the cells were printed onto the soft hydrogel with enough force to be encapsulated in a 3D manner, rather than simply adhering to the surface. Using this layer by layer method, three cell patterns were incorporated into a 3D hydrogel, with each

layer comprising approximately 50 -75 μm in thickness^{83,90}. In a different study, salt leached PLGA impregnated with collagen or Matrigel was utilized with BioLP to print endothelial cells into distinct patterns of microscopic lines⁹⁵. The endothelial cells were seen to form vessel-like networks and maintain their pattern configurations. Further, the PLGA based biopapers were sturdy enough to be physically stacked together to form a 3D construct, which served as a proof of concept for fabricating 3D vascularized scaffolds⁹⁵.

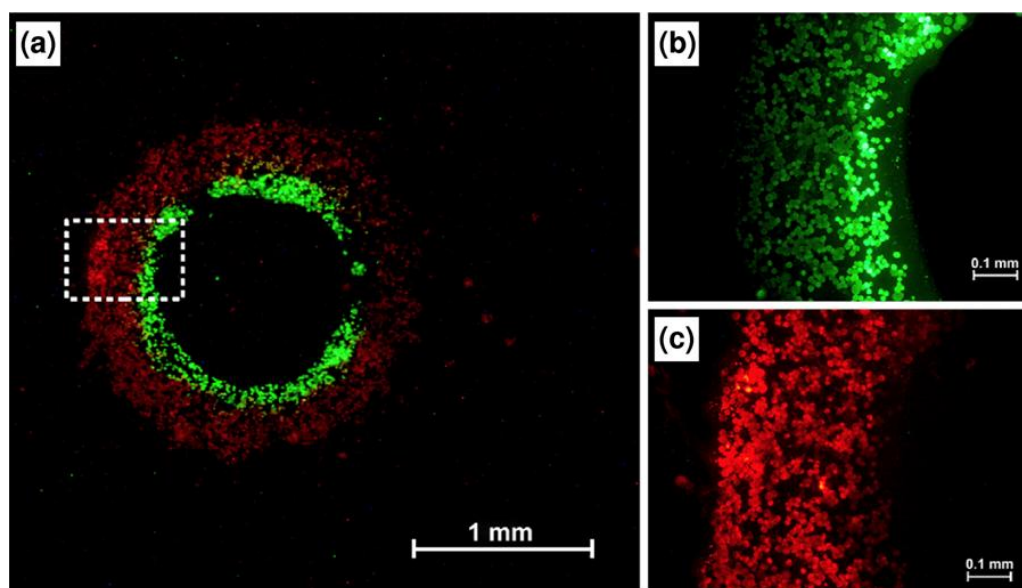


Figure 1-16: Multicolor Biological Laser Printing. (a) Human endothelial cells were labeled with green or red fluorescent dyes, and printed using BioLP into a pattern of concentric circles. (b-c) Higher magnification of the patterned cellular structures. The two cellular circles partially overlap at their interface⁹⁴.

1.12 Photopatterning

In parallel with the development of biological 3D printing, photopatterning has evolved into an array of techniques capable of fabricating 3D hydrogels with detailed features on the micron scale. Originally developed and long used in the microelectronics

industry, photopatterning involves spatial and temporal control of light-based chemical reactions using a photomask to facilitate or alter the crosslinking of polymers.

Photopatterning in tissue engineering has developed in conjunction with the synthesis of biocompatible macromolecular precursors that can be polymerized via a free radical induced cross linking reaction in order to form photopolymerized hydrogels⁵². Recently, two distinct photopatterning techniques, namely layer-by-layer photolithography and microfluidic photopatterning, have been developed to fabricate 3D hydrogel scaffolds with detailed micron scale features for use in tissue engineering applications.

1.12.1 Layer by Layer Photolithography

Layer by layer photolithography, sometimes referred to as stereolithography, employs an iterative strategy in which a thin film of uncrosslinked hydrogel precursor solution is exposed to light of a particular wavelength through a photomask. In regions where the photomask is clear, the light passes through to the polymer and initiates a free radical-induced crosslinking reaction⁵¹. The hydrogel precursor solution normally contains a photocrosslinkable polymer, a photoinitiator, and, at times, living cells. After the crosslinking of the first hydrogel layer, excess solution is washed away, and a second layer of precursor solution is deposited and subsequently polymerized. This process is then repeated until hydrogel scaffolds with the desired 3D architecture have been achieved.

Several different methods have been implemented to control the features of photopolymerized hydrogel scaffolds using layer-by-layer photolithography. Early researchers used molds and transparency photomasks to control the structure of each layer. For example, Teflon spacers and a photomask with a series of uniform spheres and

channels were used in combination with a UV lamp in order to photopolymerize a poly(2-hydroxyethyl methacrylate) (polyHEMA) hydrogel micropatterned with a controlled porosity and gel thickness⁹⁶. Pores of 62 μm and channels of 200 μm were fabricated. After collagen deposition, these poly(HEMA) scaffolds were shown to support the spreading and differentiation of myoblasts into fibrillar structures that aligned along the micropatterned porosity⁹⁶. In a different study, PEG-DA hydrogels were polymerized in an interfacial manner to facilitate layer by layer patterning⁹⁷. Specifically, PEG-DA mixed with poly(ethylene glycol)-amino acrylate (PEG-AA) was photopolymerized onto an eosin Y functionalized surface. After the photopolymerization of the first layer, eosin Y was soaked into the hydrogel to react with free amines of the PEG-AA, thus providing a new functionalized surface on which the next hydrogel layer was polymerized. With this technique, a series of complex transparency photomasks were utilized to fabricate hydrogels into a high resolution (50 micron) structure that resembled a complex vascular architecture⁹⁷. Hydrogels fabricated with transparency photomasks have also been shown to facilitate high cell viability during crosslinking and even increased nutrient transport and cell function compared with bulk, non-patterned hydrogels⁹⁸. The use of laser light sources and virtual masks have become increasingly common to achieve both high resolution control and a larger degree of automation in the fabrication of photopolymerized hydrogel structures. For example, a UV laser was utilized in combination with a platform that translates in the Z direction in order to polymerize multilayer, cellularized PEG-DA hydrogels (Figure 1-17a)^{99,100}. Specifically, CAD software directed the UV laser to photopolymerize a cell-laden hydrogel into a cross hatch structure (Figure 1-17b). The platform was moved axially after the initial

polymerization and a second layer was photopolymerized onto the first layer. Unique populations of fibroblasts were also incorporated into different layer sets of the hydrogel to fabricate a complex multilayer tissue engineering scaffold (Figure 1-17c)¹⁰⁰.

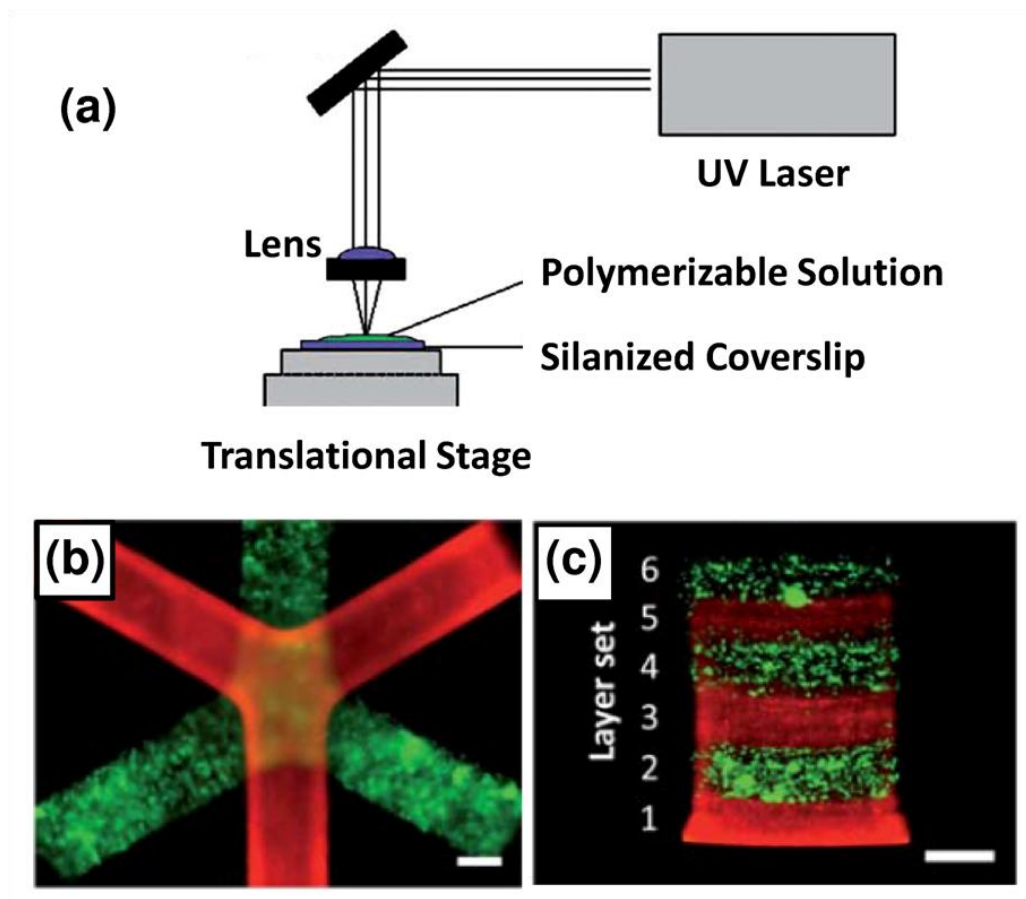


Figure 1-17: Layer by Layer Photolithography. (a) Layer by layer photolithography experimental setup where a UV laser is used to polymerize a monomer solution into distinct shapes using a translational stage. To form each new layer the stage then moves axially. Adapted from Khetan *et al*⁹⁹. (b) A multi-layer PEG-based hydrogel forming a complex crosshatch structure. The first layer set of the scaffold contains green fluorescent fibroblasts while the second layer set contains red fluorescent fibroblasts. Scale bar = 1 mm. (c) A cross sectional view of a multilayer PEG-based hydrogel, with each layer containing red or green labeled fibroblasts. Six sets of layers are shown, with each layer set approximately 500 μm . Scale bar = 1 mm. Adapted from Chan *et al*¹⁰⁰.

1.12.2 Microfluidic Photopatterning

Through the variation of fluid flow in channels on the microscale, three-dimensional scaffolds have been fabricated that restrict cells and biomolecules to distinct three-dimensional volumes¹⁰¹. Specifically, a matrix polymer solution with cells may be perfused through a channel at a particular flow rate and then polymerized so that the matrix occupies only a portion of the channel. Additional matrix polymers with different types of cells may then be perfused through the polymer free section of the channel at controlled flow rates so as not to disturb preformed layers. Upon polymerization, multilayer cellular constructs may be fabricated. In recent work by Tan and Desai, microchannels molded into PDMS were serially perfused with different polymers and cell types to fabricate a construct that mimicked the environment of blood vessels. Specifically, collagen with fibroblasts, a collagen and chitosan mixture with smooth muscle cells, and matrigel with endothelial cells were recently fabricated into a multilayer 3D structure that mimicked the adventitia, media, and intima of blood vessels¹⁰². Other researchers have used flow of buffer in between streams of hydrogel to polymerize distinct sub-channel structures within a microfluidic device as a means to more precisely study paracrine cellular communication mediated by soluble factors¹⁰³. A microfluidic system was also recently developed in which multiple types of photopolymerizable materials could be rapidly polymerized into 3D structures on the microscale in a highly automated way¹⁰⁴. This system involved flowing a hydrogel precursor solution in a chamber, polymerizing it with a 532 nm laser, and then washing away uncrosslinked material (Figure 1-18a).

The process was repeated with various hydrogel precursor solutions to form complex, multi-component hydrogel structures (Figure 1-18b). Complex structures were patterned using this technique with a resolution of $3\ \mu\text{m}^{104}$.

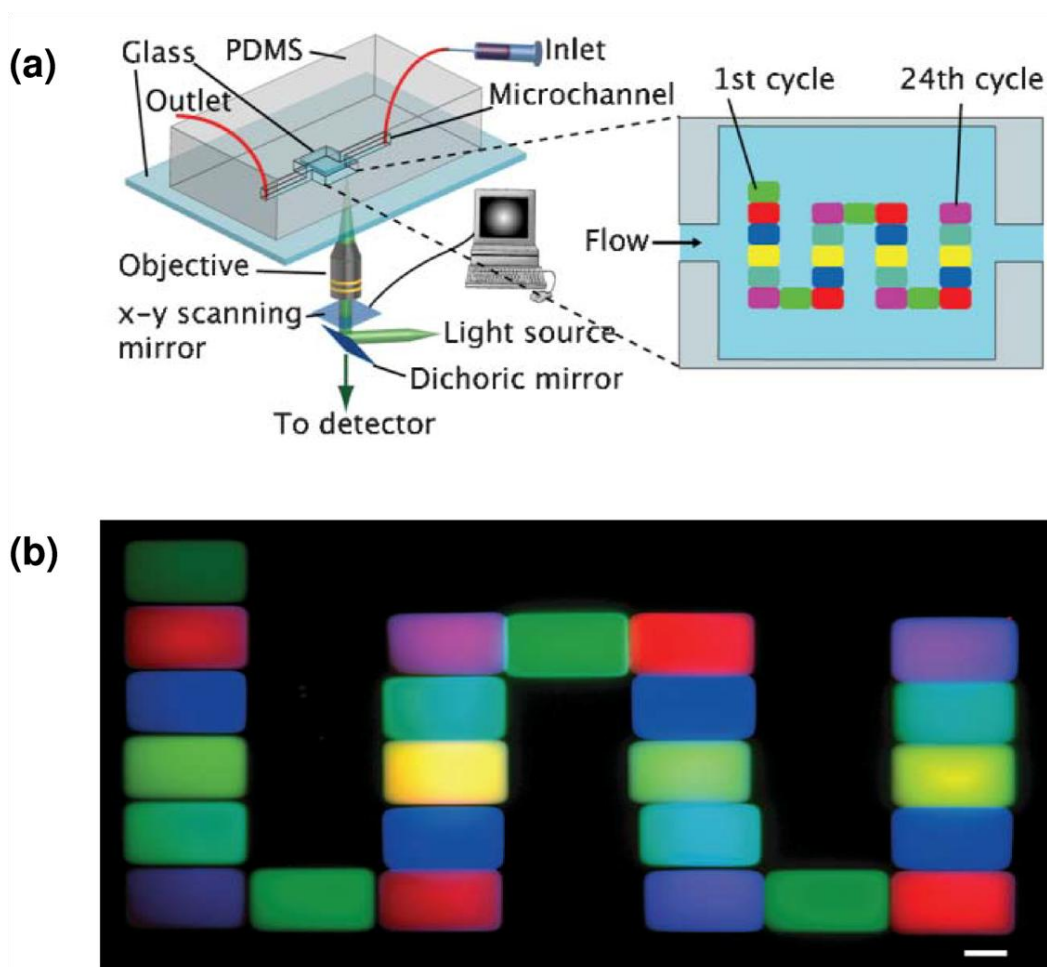


Figure 1-18: Microfluidic Photopatterning. (a) Microfluidic patterning setup. A microfluidic device was placed on the stage of a confocal microscope. Photocurable agents were injected via the inlet. Structures were then polymerized and washed before the next cycle began. (b) PEG-based hydrogels fabricated within a microfluidic system. 24 compositionally unique microscopic PEG-based hydrogels were fabricated using 24 cycles of this process. Scale bar = 200 μm . Adapted from Cheung et al.¹⁰⁴

1.13 Shortcomings of Current 3D Scaffold Fabrication Technologies

While three-dimensional scaffold fabrication technologies have come a long way since their development, each technique still possesses distinct advantages and disadvantages (Table 1-1). For example, direct-write bioprinting and layer by layer photolithography are best suited for fabricating 3D structures, but in many cases lack the resolution necessary to manipulate individual cells into complex tissue microstructures. Biological laser printing has become a fine way to manipulate cell position, but has limited ability to fabricate spatially complex 3D structures. Ink-jet printing and microfluidic photopatterning are promising in terms of accessibility and economics, but the ability to fabricate larger 3D structures with precise resolution has only just begun to be realized. Overall, however, the principal shortcoming of these scaffold microfabrication technologies is that they employ a sequential layering method to create microstructures with desired axial depths. When placing layer upon layer of material, scaffolds suffer from a lack of fidelity and feature resolution in the axial dimension as it becomes difficult to precisely align layers with micrometer precision¹⁰⁵. These issues are further compounded when attempting to fabricate three-dimensional structures with precise spatial control of multiple bioactive ligands. To present physical and biochemical cues to cells in a physiologically relevant way, a fabrication technology must be developed that offers both micron level control in three dimensions, as well as the ability to easily pattern multiple bioactive moieties with high fidelity.

Table 1-1: Pros and Cons of 3D Microfabrication Technologies. A list of the advantages and disadvantages of 5 different techniques to fabricate and manipulate 3D biomaterials.

	Pros	Cons
Direct-Write Bioprinting	<ul style="list-style-type: none"> - Fabricate large structures - Fabricate 3D structures 	<ul style="list-style-type: none"> - Lacks 3D resolution - Difficult to pattern multiple bioactive molecules
Ink-jet Bioprinting	<ul style="list-style-type: none"> - Accessible and economical - Incorporation of multiple cell types 	<ul style="list-style-type: none"> - Difficult to achieve 3D structures - Difficult to pattern multiple bioactive molecules
Biological Laser Printing	<ul style="list-style-type: none"> - Allows for precise placement of cells - Incorporation of multiple cell types 	<ul style="list-style-type: none"> - Difficult to achieve 3D structures - Difficult to pattern multiple bioactive molecules
Layer-by-Layer Photolithography	<ul style="list-style-type: none"> - Fabricate 3D structures - Incorporation of multiple materials/cell types 	<ul style="list-style-type: none"> - Lacks 3D resolution
Microfluidic Patterning	<ul style="list-style-type: none"> - High throughput - Incorporation of multiple materials/cell types 	<ul style="list-style-type: none"> - Lacks 3D resolution

1.14 Post-Gelation Photopatterning of PEG-based Hydrogels

The integration of versatile PEG-based hydrogels and post-gelation photopatterning techniques overcomes many of the current shortcomings of current 3D scaffold fabrication technologies and serves as an excellent platform for engineering the microvasculature. Post-gelation photopatterning involves the crosslinking of a preformed hydrogel and the subsequent micropatterning of physical or biochemical structures within that hydrogel by exposing portions of the gel to light of a particular wavelength⁹⁹. Post-gelation patterning is often achieved by permeating the pre-formed hydrogel with photoinitiator molecules as well as with biomolecules to be patterned into the gel. Traditionally, patterning of PEG hydrogel systems has been primarily centered on surface patterning of biomolecules. For example, the integration of photolithography with photopolymerizable hydrogels has yielded the fabrication of complex patterns of biomolecules on hydrogel surfaces. Using a designed, high resolution transparency mask, biomolecules such as acrylate-PEG-RGDS have been patterned in monolayers onto PEG-DA hydrogel surfaces in specific regions via the application of UV light and a

photoinitiator (Figure 1-19)⁵⁹. The resulting photopatterns yield controlled designs of adhesive peptide (and therefore cells) on an otherwise non-adhesive PEG substrate, but they fail to present biochemical cues in a physiologically relevant three-dimensional manner.

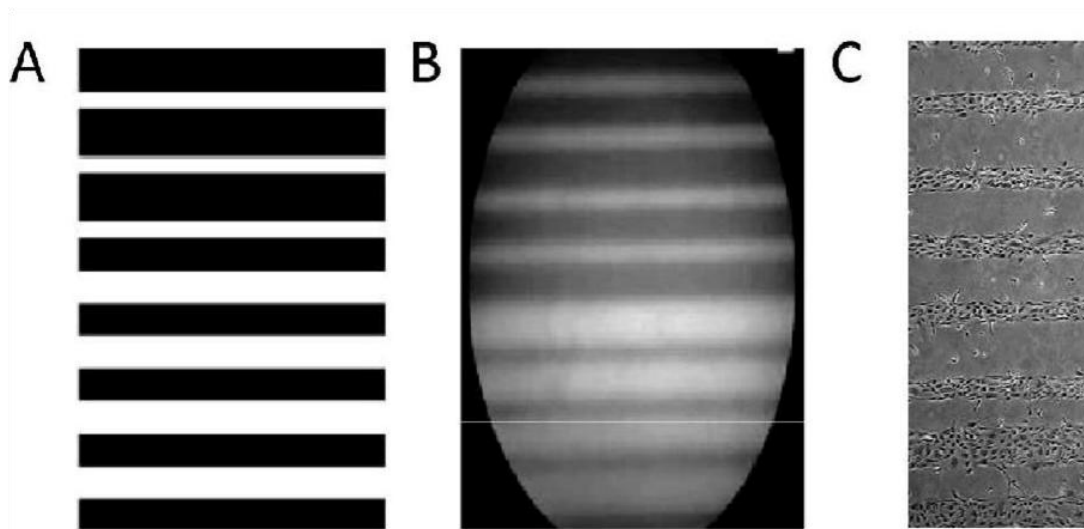


Figure 1-19: Photolithography on PEG-DA Hydrogels. (a) High resolution photomask used to pattern fluorescently labeled regions of acrylate-PEG-RGDS peptide on PEG-DA hydrogels. HUVECS align and form tubes on these patterns (c). Adapted from Moon et al.⁶⁵

Luo and Shoichet were among the first researchers to guide cells through 3D hydrogel environment using immobilized patterns of biomolecules¹⁰⁶. Specifically, these researchers utilized a degradable agarose hydrogel modified with a cysteine based sulphhydryl protecting group that was cleavable with UV light¹⁰⁶. A UV laser was utilized to cleave these protecting groups into the shape of a channel, and the free sulphhydryl groups were then chemically reacted with the biomolecule maleimide-GRGDS. This scheme created 3D channels of GRGDS through the hydrogel, and neural cells were seen

to be guided down these pathways, demonstrating the guidance of cells in a micropatterned 3D biomaterial¹⁰⁶.

An advance in laser-based photopatterning has come with the advent of laser scanning lithography (LSL) using confocal microscopes. Confocal microscopes scan precisely focused laser light over a specified area and use an adjustable light collection pinhole to eliminate out of focus light and to allow for optical sectioning with high axial resolution¹⁰⁷. In LSL, a confocal laser scanning microscope is utilized to excite a photoinitiator and crosslink biomolecules within a hydrogel, which may subsequently be utilized to guide cellular organization. To achieve a high level of spatial resolution, virtual masks were designed, yielding defined regions of interest for laser excitation and subsequent patterning¹⁰⁸.

Additionally, laser exposure times may be varied to fabricate concentration gradients of crosslinked PEG-RGDS within the PEG hydrogel¹⁰⁸. While patterns fabricated using traditional LSL have an increased lateral resolution and exposure flexibility compared with traditional transparency masks, crosslinking of adhesive ligands occurs throughout the axial dimension of the hydrogel, thus limiting the ability of the technique to crosslink high-resolution, three-dimensional patterns within bulk hydrogels. Recently, laser scanning lithography has been transformed into a more powerful technology due to the increased availability of two-photon microscopes. In order to recognize the significance of this advance, however, one must first understand the basic principles of two-photon excitation.

1.15 Two-Photon Excitation

When considering normal photonic excitation, a fluorophore is excited with light of the appropriate wavelength, and an electron is allowed to reach an excited energy state. Upon relaxation of this electron, energy is released in the form of a photon, producing the fluorescent effect. In two-photon excitation, the simultaneous excitation of two photons of a lower energy is used to excite a fluorophore, which may then release a photon at a higher energy than either of the two excitatory photons. For example, two-photon excitation using light at 720 nm will allow for fluorophore excitation at 360 nm. The probability of two-photon excitation is very low, and thus a high frequency pulsed laser, such as a titanium sapphire laser, is normally required to achieve the effect. A Ti:Sapphire laser is capable of producing light pulses faster than 100 femtoseconds at a frequency of 75 Megahertz¹⁰⁹. The pulse nature of the laser allows for the peak excitation power to be very high (1 – 10 kilowatts), while the average power is sufficiently low as to not cause damage to materials and even allow for cell viability¹⁰⁹. Two-photon excitation has several innate advantages over one photon excitation. First, the probability of simultaneous excitation of two photons is proportional to the square of the light intensity, and thus excitation decays away rapidly with the fourth power of distance from the focal point¹¹⁰. Functionally, this allows for the excitation to be limited to a microscopic, three-dimensional volume at the focal point of excitation light; therefore, while one photon excitation would excite a fluorophore throughout the axial direction of a sample, two-photon excitation allows for innate three-dimensionality in which the fluorophore is only excited where the light is precisely focused (Figure 1-20)¹⁰⁹. Another advantage of two-photon excitation is that long wavelength infrared light, (between 720 – 1200 nm) is used

for excitation, and this light normally passes through biological water-based materials with significantly less scattering than visible or ultraviolet light, thereby allowing for high resolution excitation at greater axial depths in hydrogels. While traditionally employed for optical imaging, two-photon excitation may also be used to confine photo-reactive processes to three-dimensional focal volumes with high resolution.

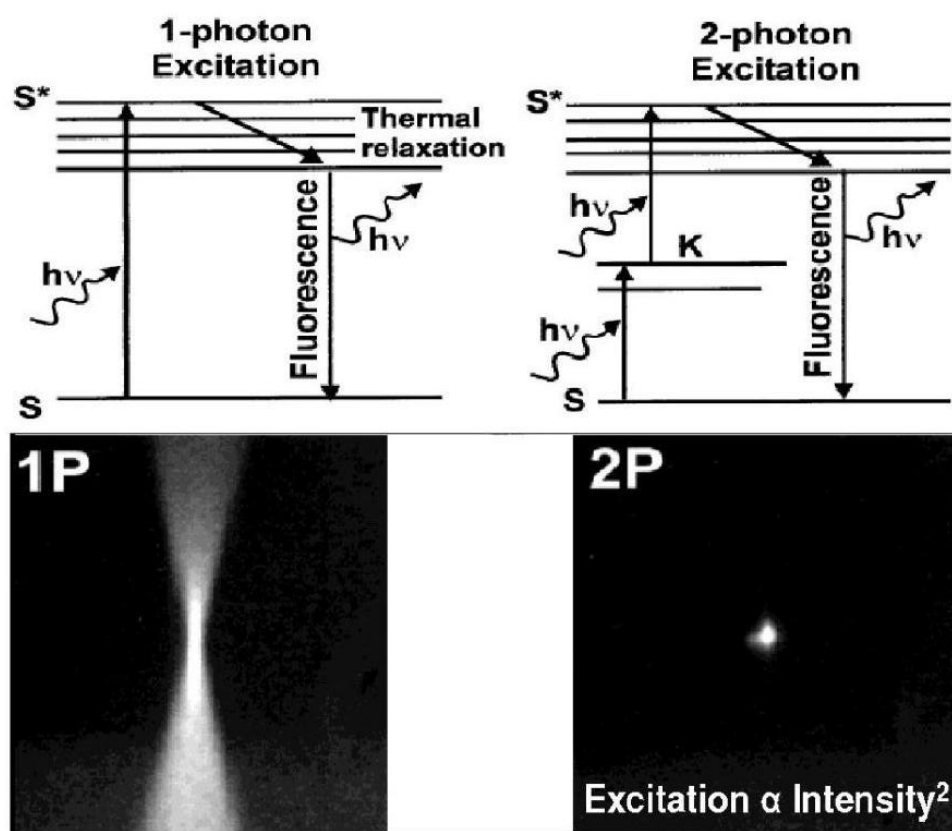


Figure 1-20: Two-Photon Excitation. The probability of excitation of two simultaneous photons is proportional to the intensity squared, thereby limiting excitation to a minute three-dimensional volume. Adapted from Soeller *et al.*¹⁰⁹

1.16 Two-Photon Laser Scanning Lithography

The use of a two-photon excitation process to directly modify preformed, photosensitive hydrogel scaffolds offers a straightforward alternative for the fabrication of 3D microenvironments with high 3D resolution and a large degree of spatial control over multiple biomolecules. Two-photon laser scanning lithography (TP-LSL) in photosensitive acrylate-based PEG hydrogels takes advantage of the two-photon excitation phenomenon by confining photo-reactive processes to focused, 3D microvolumes, leaving all other points along the laser's optical path unaltered (Figure 1-21)⁵⁸.

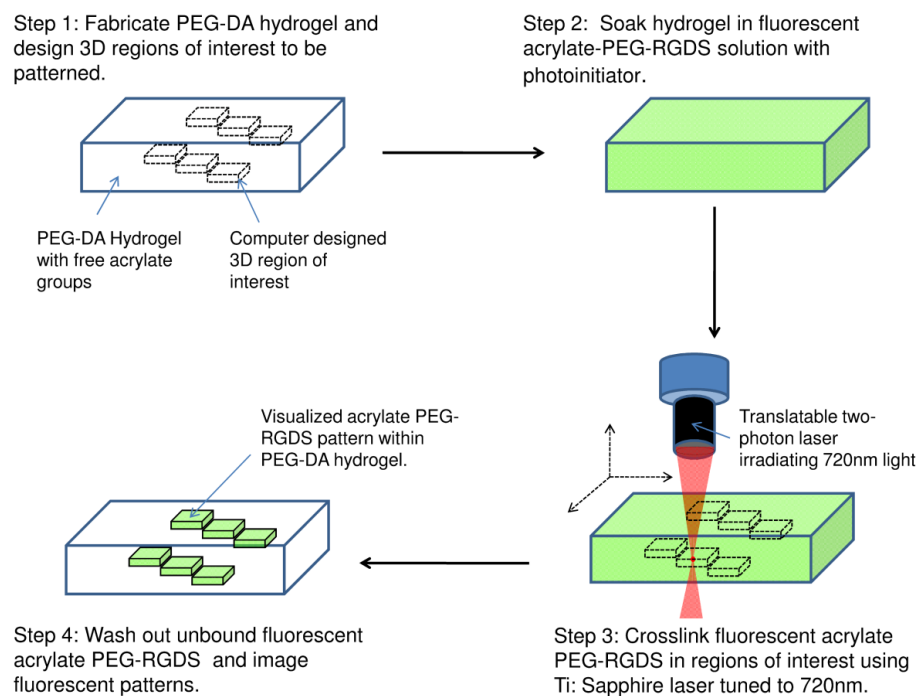


Figure 1-21: TP-LSL Methodology. A PEG-DA hydrogel was fabricated and 3D ROIs were designed using LSM software. Fluorescent monoacrylate PEG-RGDS solution with photoinitiator was soaked into the PEG-DA hydrogel, and a Ti: Sapphire laser tuned to 720 nm was used to crosslink the fluorescent PEG-RGDS moieties in desired free form 3D patterns. The PEG-DA GELS were washed thoroughly and imaged¹¹⁵.

Specifically, a photocrosslinkable, bioactive molecule (acrylate-PEG-ligand) is soaked into a preformed PEG hydrogel, and through the use of a microscope, a focused, two-photon laser excites photoinitiator molecules instead of a fluorophore. This two-photon excitation induces free-radical based chemical crosslinking of the biomolecule at the microscopic, three-dimensional volume of the laser focal point. Uncrosslinked molecules are then washed away, leaving behind precisely designed three-dimensional regions of bioactivity with preformed hydrogel scaffolds. This technology is developed and applied in this thesis to three-dimensionally pattern various biomolecules with PEG hydrogel scaffolds, and ultimately is utilized to guide the biomimetic formation of a microvasculature.

1.17 Summary

Much has already been accomplished towards the engineering of vascularized tissues; however, in order to take the next step towards functional therapeutics, there remains a need to develop 3D scaffolds that can mimic the complex tissue architectures found in nature. Enzymatically degradable, acrylate based PEG hydrogels have been shown to act as a blank slate into which custom designed biomolecules may be introduced via photopatterning technologies. Recently, the advent of TP-LSL has made possible the three-dimensional arrangement of bioactive ligands within these hydrogel scaffolds, allowing for an unprecedented level of biomaterial control. In this thesis, two-photon laser scanning lithography is further developed and applied to multiple applications in tissue engineering. First, the system capabilities and parameters of TP-LSL are fully explored, answering questions about the size, resolution, and concentration of biomolecule patterns as well as the patterning of multiple types of biomolecules in

three dimensions. Next, a novel system to probe three-dimensional cellular dynamics is developed, allowing for the examination of complex migratory behaviors under various micropatterned conditions and ultimately shedding light on how cells interact with their environment and organize into tissues. Finally, this thesis demonstrates the ability to pattern biomolecules into the exact structure of endogenous microenvironments, including those of the critical microvasculature. These bioactive patterns are then shown to structurally guide the formation of tissue engineered vessels into the precise structure of vessels that occur naturally in the body.

In summary, the development and application of two-photon laser scanning lithography discussed in this thesis has provided a new toolset to both probe three-dimensional cell behavior and to mimic endogenous cellular architectures within multifunctional biomaterials. Most importantly, however, this work stands as an important advance in the tissue engineering community, taking scientists one step closer to the fabrication of functional vascularized organs that could one day save thousands of lives.

Chapter 2: Three-Dimensional Photolithographic Patterning of Multiple Bioactive Ligands in Poly(ethylene) Glycol Hydrogels

A significant portion of this chapter has been previously published in:

J.C. Hoffmann and J. L. West. 2010. Three-dimensional photolithographic patterning of multiple bioactive ligands in poly(ethylene glycol) hydrogels. *Soft Matter* 6:5056- 63.

2.1 Introduction

A tremendous amount of research has focused on the design of complex biomaterials to recreate a physiological tissue environment. Potential applications range from the development of pharmaceutical assays and diagnostics to the production of drug delivery devices and tissue engineered therapeutics¹¹¹. Much of this work initially focused on the study of cell-biomaterial interactions in two dimensions (2D); however, recent findings have shown that nearly all cell types require three-dimensional (3D) cues to produce a physiologically relevant response⁶⁶. In order to mimic physiological tissue structures, it is of critical importance to design and fabricate 3D microenvironments in which bioactive signals may be presented in a precisely controlled manner.

As discussed in chapter 1, researchers have recently utilized hydrogels as a useful medium in which to engineer a 3D biological microarchitecture, taking advantage of their tunable physical and chemical properties^{51,112}. Poly(ethylene glycol) (PEG) hydrogel systems, in particular, have been used extensively due to their ability to probe individual mechanical and biochemical effects without the presence of confounding biological factors, such as collagen or other extracellular matrix components, that are found in many naturally derived scaffolds^{52,56}. PEG macromers modified with an acrylate group at each terminus have been shown to rapidly polymerize upon exposure to light in the presence

of an appropriate photoinitiator. These PEG-based hydrogels act as a “blank slate” into which biochemical cues may be incorporated, thus allowing for the introduction of bio-functionalized patterns via controlled light exposure (Figure 2-1)^{59,113,114}.

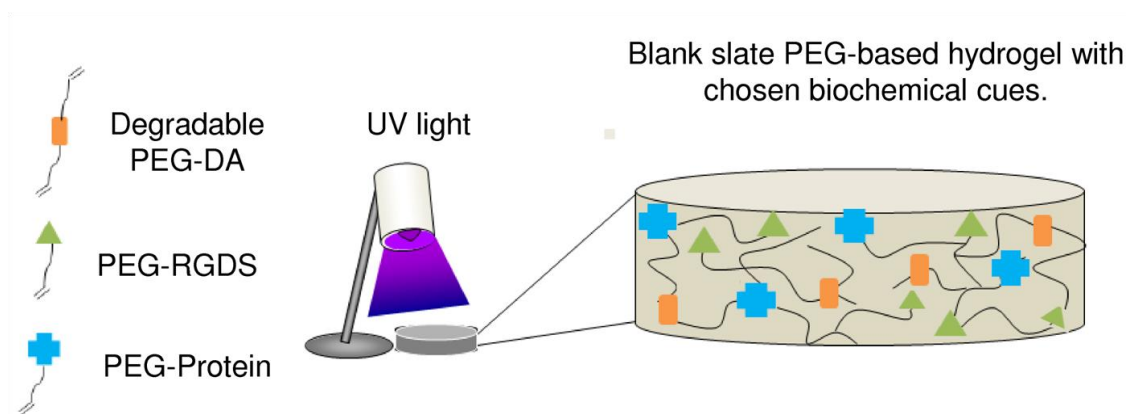


Figure 2-1: Incorporation of Biomolecules into PEG-based Hydrogels. Biochemical cues such as PEG-RGDS or PEG-proteins can be mixed with enzymatically degradable PEG-DA and a photoinitiator to form a hydrogel precursor solution. Upon exposure to UV light, acrylate groups are covalently crosslinked leading to the formation of an enzymatically degradable hydrogel with immobilized biochemical cues. Adapted from Saik¹¹⁴.

In parallel with the development of versatile hydrogel materials, a variety of microfabrication techniques have emerged with the goal of transforming these materials into structures that offer a 3D microenvironment. In particular, as reviewed in detail in Chapter 1, 3D printing and photolithography have been utilized with increasing success to fabricate biomaterials with designed 3D features on the microscale¹⁰¹. However, these techniques generally employ a sequential layering method to create microstructures with desired axial depths and therefore suffer from lack of fidelity and poor resolution in the axial dimension¹⁰⁵. These issues are further compounded when designing microenvironments with multiple bioactive moieties confined to three-dimensionally distinct spatial locations.

The use of a two-photon excitation process to directly modify preformed, photosensitive hydrogel scaffolds offers a straightforward alternative for the fabrication of 3D microenvironments. Utilizing the simultaneous absorption of two photons from a high frequency pulsed laser, excitation volumes may be effectively limited to a minute focal volume¹¹⁰. Two-photon laser scanning lithography (TP-LSL) in photosensitive materials takes advantage of this phenomenon by confining the photo-reactive processes to focused, 3D micro-volumes, leaving all other points along the laser's optical path unaltered^{58,115}. Previously, TP-LSL has been applied to poly(ethylene glycol) diacrylate (PEG-DA) hydrogels, among other materials, yielding complex 3D patterns and gradients of biomolecules within preformed hydrogels^{45,58,98,113,116–118}. (See Section 1.16 for further discussion of this process).

Despite this significant advance in 3D microenvironment fabrication technology, relatively little progress has been made towards the application of TP-LSL to tissue engineering and fundamental cellular biology. The growth of TP-LSL applications has instead been stunted by a lack of development of its key operating parameters and system capabilities. This chapter serves to characterize and expand upon several critical aspects of TP-LSL through the micropatterning of fluorescently labeled monoacrylate PEG-RGDS peptide in PEG-DA hydrogels. Specifically, this chapter demonstrates the ability to pattern RGDS over several different size ranges, and probes the lateral and axial resolution limits of the technique. Further, the effect of laser scan speed and power on the concentration of patterned RGDS is characterized, and the versatility of TP-LSL is demonstrated by fabricating micropatterns of varying 3D shape. Patterns of multiple, spatially overlapping acrylate-PEG-RGDS moieties have also been shown to serve as a

proof of concept for fabricating a complex, heterogeneous cellular microenvironment. Finally, this chapter reports the micropatterning of two distinct, fibronectin derived peptides (RGDS and CS-1) within a collagenase degradable PEG-DA hydrogel to demonstrate a seamless transition towards the patterning of different types of adhesive ligands and growth factors within photosensitive, biodegradable materials. These results demonstrate the versatility and effectiveness of TP-LSL as a technique to fabricate complex biological landscapes at the microscale and should serve as a solid foundation upon which a variety of biomimetic technologies may be built.

2.2 Materials and Methods

2.2.1 Poly(ethylene glycol) Diacrylate (PEG-DA) Synthesis and Purification

Dry poly(ethylene glycol) (PEG 3400 Da; Fluka) was reacted with acryloyl chloride (Sigma) at a 1:4 molar ratio in anhydrous dichloromethane (DCM; Sigma) with triethyl amine (TEA; Sigma) at a 1:2 molar ratio (PEG:TEA) (Figure 2-2). The reaction was stirred overnight under argon and washed with 2M K_2CO_3 to remove chloride salt via phase separation. The PEG-DA containing organic phase was dried using anhydrous $MgSO_4$, filtered, and precipitated in diethyl ether. The final PEG-DA product was filtered, dried overnight under vacuum, and characterized by 1H -NMR.

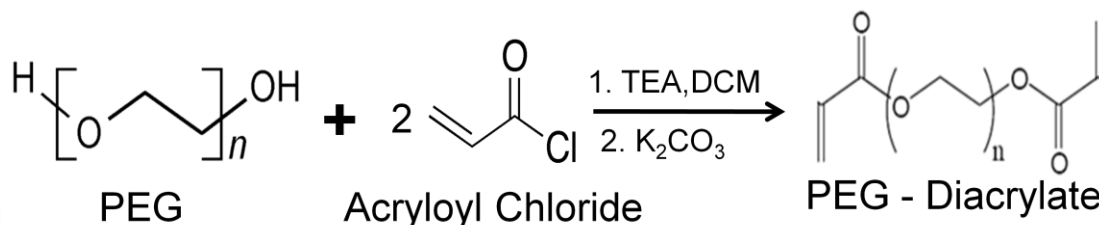


Figure 2-2: PEG-DA Synthesis. Reaction scheme for synthesizing poly(ethylene glycol) diacrylate (PEG-DA). Poly(ethylene glycol) (3400 Da) was reacted with excess acryloyl chloride in the presence of triethyl amine in DCM to form PEG-DA. PEG-DA was then washed with potassium carbonate to separate the chloride salt via phase separation.

2.2.2 Synthesis of Monoacrylate PEG-peptides and Degradable PEG-DA Hydrogels

Acrylate-poly(ethylene glycol)-succinimidyl carboxymethyl (PEG-SCM; Laysan) dissolved in dimethyl sulfoxide (DMSO; Cambridge Isotope Laboratories) was slowly dripped into a solution of cell-adhesive RGDS peptide (American Peptide) with *N, N*-Diisopropylethylamine (DIPEA; Sigma) in DMSO so that the final molar ratios were 1:1.2 (PEG-SCM: RGDS) and 1:2 (PEG-SCM: DIPEA) (Figure 2-3a). The resulting solution was rapidly mixed under argon for 24 h, cooled on ice and mixed with Millipore water. The monoacrylate-PEG-RGDS product was dialyzed against Millipore water for 12 h using a 3500 MWCO regenerated cellulose membrane (Spectrum Laboratories) and lyophilized to dryness. Similarly, the peptide QILDVPST (abbreviated CS-1, American Peptide) was reacted with PEG-SCM in exactly the same manner to produce acrylate-PEG-CS-1. Degradable PEG-DA hydrogels were synthesized, as reported previously⁴⁷, through the incorporation of a collagenase-sensitive peptide linker into the backbone of the base PEG-DA polymer chains. Specifically, the peptide GGGPQGIWGQGK (abbreviated PQ) was synthesized via solid phase peptide synthesis with standard F-Moc chemistry using an APEX396 peptide synthesizer (Aapptec). Successful peptide synthesis was confirmed with matrix assisted laser desorption ionization time of flight mass spectrometry (MALDI-ToF; Bruker Daltonics). The purified peptide was reacted with PEG-SCM via a procedure similar to monoacrylate PEG-peptide conjugation, with the final molar ratios of 2.1:1 (PEG-SCM: PQ) and 1:2 (PEG-SCM: DIPEA) (Figure 2-3b). Monoacrylate-PEG-peptide and collagenase degradable PEG-DA(abbreviated PEG-PQ) were both characterized via gel permeation chromatography (GPC, Polymer laboratories) with detectors for UV-vis and evaporative light scattering.

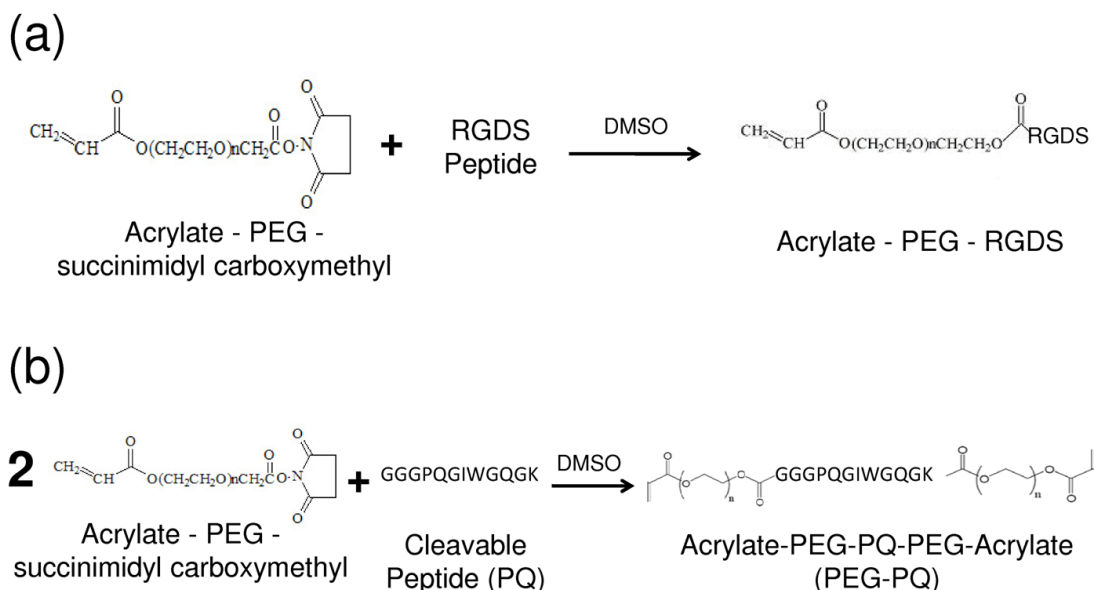


Figure 2-3: Synthesis of PEG-RGDS and PEG-PQ. (a) Acrylate-PEG-succinimidyl carboxymethyl was reacted with the RGDS peptide in DMSO to form acrylate-PEG-RGDS. (b) Acrylate-PEG-succinimidyl carboxymethyl was reacted with the enzymatically degradable peptide GGGPQGIWGQGK (abbreviated PQ) in DMSO in order to form acrylate-PEG-PQ-PEG-acrylate (abbreviated PEG-PQ).

2.2.3 Fluorescent Tagging of Monoacrylate PEG-peptides

Purified monoacrylate PEG-RGDS in 0.1M sodium bicarbonate (pH 9) was further reacted with Alexa Fluor® 488 carboxylic acid 2,3,5,6-tetrafluorophenyl ester (AF488-TFP; Invitrogen) in dimethylformamide at a 1:10 molar ratio (acrylate-PEG-RGDS:AF488-TFP) (Figure 2-4). This reaction was rapidly mixed for 2 hr and dialyzed for 12 h against Millipore water with a 3500 MWCO regenerated cellulose membrane. The resulting monoacrylate-PEG-RGDS-Alexa Fluor®488 was lyophilized to dryness and stored at -20 °C. This reaction was carried out in the same manner with Alexa Fluor® 532 carboxylic acid succinimidyl ester (AF532-SE; Invitrogen), or Alexa Fluor® 633 carboxylic acid succinimidyl ester (AF633-SE; Invitrogen) dissolved in 0.1M sodium bicarbonate buffer (pH 8.3) to form monoacrylate-PEG-RGDS-Alexa Fluor®532 and

monoacrylate-PEG-RGDS-Alexa Fluor®633, respectively. A similar procedure was followed to fluorescently label monoacrylate-PEG-CS1.

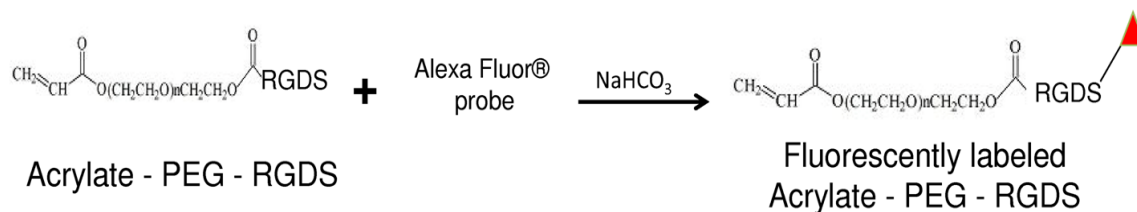


Figure 2-4: Fluorescent Acrylate-PEG-RGDS Synthesis. Acrylate-PEG-RGDS was reacted with an Alexa Fluor® probe to form fluorescently labeled acrylate-PEG-RGDS.

2.2.4 PEG-DA Hydrogel Fabrication

A glass coverslip was incubated in a solution of 75% sulfuric acid (VWR) and 25% hydrogen peroxide (30% w/w, VWR) for 1 h with gentle agitation. Coverslips were then rinsed with Millipore water and incubated in 85 mM 3-(Trimethoxysilyl)propyl methacrylate (Fluka) in ethanol (pH 4.5) to introduce surface methacrylate groups to the glass⁹⁸. Hydrogel molds were constructed by securing a 0.5 mm thick poly(tetra fluoroethylene) (PTFE) spacer between a methacrylated coverslip and a glass slide. A prepolymer solution of 10% (w/v) PEG-DA in HBS with 10 µl/ml of 300 mg/ml 2, 2-dimethoxy-2-phenylacetophenone (DMPAP) in *N*-vinyl pyrrolidone (NVP) was prepared. The prepolymer solution was injected into the mold and exposed to long wavelength ultraviolet light (B-200SP UV lamp, UVP, 365 nm, 10 mW/cm²) for 45 sec, forming a crosslinked and immobilized hydrogel on the methacrylated glass coverslip (Figure 2-5). Immobilized hydrogels were soaked in filtered HBS until further use. The degradable hydrogels were fabricated via the same procedure using 10% (w/v) collagenase degradable PEG-PQ.

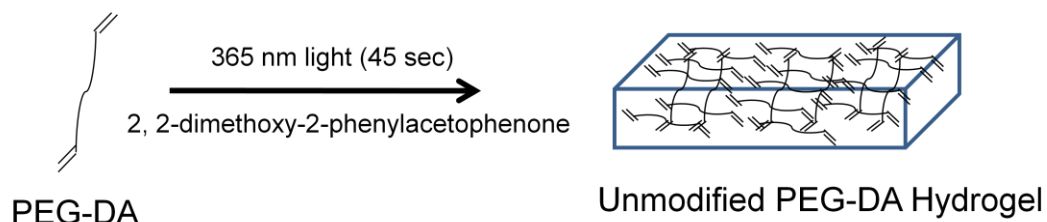


Figure 2-5: PEG-DA Hydrogel Formation. A hydrogel is formed by exposing PEG-DA to 365 nm light and photoinitiator 2,2-dimethoxy-2-phenylacetophenone.

2.2.5 Design of 3D Patterns of Fluorescent Monoacrylate PEG-RGDS

Patterns of desired dimensionality and concentration were specified using the region of interest (ROI) function on a Zeiss LSM 510 META NLO confocal microscope (Carl Zeiss Inc) by selecting the laser intensity, laser scan speed, microscope objective, and Z plane focus. Specifically, a 10X Plan-Apochromat objective lens (NA 0.4), a 20X Plan-Apochromat objective lens (NA 0.75) and a 63X Plan-Apochromat objective lens (NA 1.4) were utilized to create patterns of varying size. To tune the concentration of crosslinked fluorescent monoacrylate PEG-RGDS molecules, scan speeds of 204 $\mu\text{sec}/\text{pixel}$, 102 $\mu\text{sec}/\text{pixel}$ and 51 $\mu\text{sec}/\text{pixel}$ were utilized. Additionally, pattern concentrations were also varied using laser intensities of 25 $\text{mW}/\mu\text{m}^2$, 21 $\text{mW}/\mu\text{m}^2$, and 17 $\text{mW}/\mu\text{m}^2$. Unless otherwise specified, patterns were generally fabricated using the 20X objective with a scan speed of 204 $\mu\text{sec}/\text{pixel}$, and a laser intensity of 25 $\text{mW}/\mu\text{m}^2$. To fabricate continuous patterns in the Z direction, the focus was adjusted upwards 3 μm in between subsequent scans. Patterns shown were created using 3-5 scans each separated by 3 μm , unless otherwise specified. To create patterns of varying 3D shapes, the designed ROI was modified for differing Z planes.

2.2.6 Patterning PEG-RGDS using Two-Photon Laser Scanning Lithography

The TP-LSL methodology for fabricating 3D patterns of fluorescent monoacrylate-PEG-RGDS in PEG-DA hydrogels was outlined in Figure 1-18. A crosslinked, immobilized PEG-DA hydrogel was incubated in a solution of monoacrylate-PEG-RGDS-Alexa Fluor®488 (5-10 nmol/ml) in HBS with 10 µl/ml of 300 mg/ml DMAP in NVP for 30 min under gentle rocking conditions. The hydrogel was positioned on the stage of an LSM 510 META NLO confocal microscope (Carl Zeiss Inc.). A titanium/sapphire laser tuned to 720 nm was scanned across a pre-designed ROI to initiate crosslinking of free acrylate groups in desired, free-form 3D patterns. After patterning, the hydrogel was washed extensively with HBS under gentle rocking for 48 h to remove unbound fluorescent monoacrylate-PEG-RGDS and photoinitiator. The resulting patterns were imaged using traditional confocal microscopy (Zeiss5 LIVE, Plan-Apochromat 20x objective with 0.8 numerical aperture: for Alexafluor 488 excitation = 489 nm, emission BP filter = 500–525 nm; for Alexafluor 532 excitation = 532, emission BP filter = 560-675; for Alexafluor 633 excitation = 633 nm, emission long pass filter = 650 nm). Patterns were projected and analyzed using ImageJ (NIH Bethesda, MD). A background subtraction was applied to reduce the auto-fluorescence of the PEG-DA hydrogel.

To pattern multiple fluorescent peptides, an immobilized PEG-DA hydrogel was patterned with PEG-RGDS-Alexa Fluor®488 as described above. After washing, the hydrogel was incubated in a solution of monoacrylate-PEG-RGDS-Alexa Fluor®532 (5-10 nmol/ml) in HBS with 10 µl/ml of 300 mg/mL DMAP in NVP for 30 min with gentle rocking. Patterns of PEG-RGDS-Alexa Fluor®532 were created as before through the scanning of the 720 nm laser across designed regions of interest. The unbound

monoacrylate PEG-RGDS-Alexa Fluor®532 and photoinitiator were washed out for 48 h, allowing for the visualization of both fluorescent PEG-RGDS patterns via the confocal microscope. This technique was repeated with the incubation of monoacrylate-PEG-RGDS-Alexa Fluor®633, so that after laser scanning and washing, 3 different types of patterned fluorescent PEG-RGDS in close proximity to each other were visualized within a single PEG-DA hydrogel. In these studies, RGDS with the 3 fluorophores was simply used as a model peptide to demonstrate the feasibility of repetitive patterning of multiple moieties.

2.2.7 Patterning PEG-RGDS and PEG-CS-1 within a PEG-PQ Hydrogel

To pattern both PEG-RGDS and PEG-CS-1 into a PEG-PQ hydrogel, a procedure similar to that described in Section 2.2.4 and 2.2.6 was utilized. Briefly, an immobilized 10% PEG-PQ hydrogel was fabricated and permeated with a solution of monoacrylate-PEG-RGDS-Alexa Fluor®488 (5-10 nmol/ml) in HBS with 10 µl/ml of 300 mg/ml DMAP in NVP for 30 min under gentle rocking conditions. The hydrogel was positioned on the stage of an LSM 510 META NLO confocal microscope (Carl Zeiss Inc.) and a titanium/sapphire laser tuned to 720 nm was scanned across a pre-designed ROI to initiate crosslinking of free acrylate groups in desired, free-form 3D patterns. After 48 h washing, the hydrogel was incubated in a solution of monoacrylate-PEG-CS-1-Alexa Fluor®633 (5-10 nmol/ml) in HBS with 10 µl/ml of 300 mg/mL DMAP in NVP for 30 min with gentle rocking. Patterns of PEG-CS-1-Alexa Fluor®633 were created as before through the scanning of the 720 nm laser across designed regions of interest. The unbound monoacrylate PEG-CS-1-Alexa Fluor®633 and photoinitiator were washed out

for 48 hr. Both fluorescent PEG-RGDS and fluorescent PEG-CS1 were then visualized within a single PEG-PQ hydrogel microenvironment using confocal microscopy.

2.3 Results

2.3.1 Fabrication of Fluorescent RGDS Patterns of Varying Size

To establish the versatility of TP-LSL as a biomolecular patterning strategy, ROIs were designed to demonstrate the capability of the technique to create precise, fluorescent RGDS patterns over a large size range. Patterns of fluorescent RGDS were created within PEG-DA hydrogels utilizing the different fields of view of the 10X, 20X and 63X objectives to scan the 720 nm light over different ROIs. The results, as seen in Figure 2-6, show patterns that vary in size over nearly 3 orders of magnitude. A pattern created with the 10X objective (Figure 2-6a) spans 950 μm in both lateral directions. Additionally, the thin bars in this pattern indicate a high resolution on the order of 5-10 μm with the 10X objective, demonstrating the ability to create patterns spanning nearly 1 mm across the hydrogel with micron range control of feature size. To probe the lateral resolution limit of TP-LSL, a pattern was created using the 63X objective (Figure 2-6c). This pattern showed well defined features 1 -2 μm in width, demonstrating the ability to pattern peptides within PEG-DA hydrogels in a size range highly relevant to the cellular microenvironment.

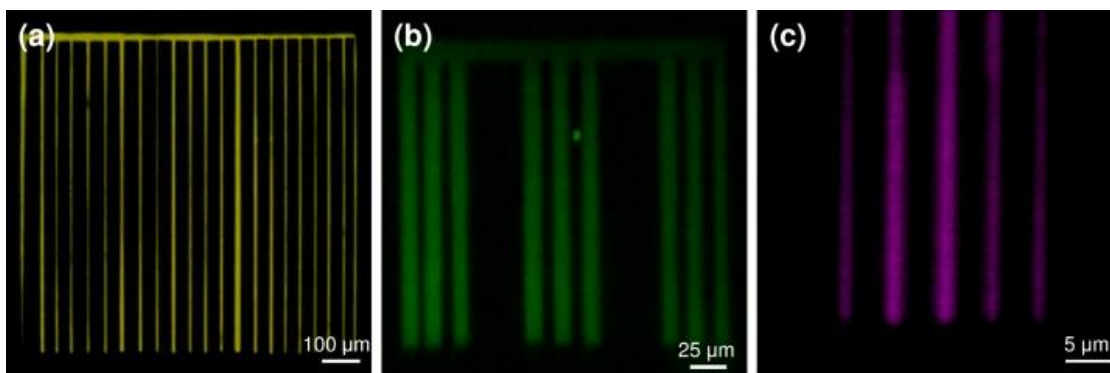


Figure 2-6: Fluorescent RGDS Patterns of Various Size. Confocal fluorescent images of patterned fluorescent PEG-RGDS within PEG-DA hydrogels. (a) PEG-RGDS-Alexa fluor®633 pattern fabricated using a 10x objective. Scale bar = 100 μm . (b) PEG-RGDS-Alexa fluor®488 pattern fabricated using a 20x objective. Scale bar = 25 μm . (c) PEG-RGDS-Alexa fluor®532 pattern fabricated using a 63x objective. Scale bar = 5 μm ¹¹⁵.

2.3.2 Axial Resolution of Fluorescent RGDS Patterning in PEG-DA Hydrogels

Patterns of fluorescent RGDS were also created within PEG-DA hydrogels to probe the axial resolution of TP-LSL. This test was performed for an array of microscope objectives with different numerical apertures. Simple ROIs were designed and a single scan of the 720 nm laser across the ROI was performed. This single scan resulted in crosslinking of fluorescent monoacrylate PEG-RGDS in a particular focal plane, and thus, all crosslinking that occurred represented the axial resolution limit. This resolution testing procedure was carried out for the 10X, 20X, and 63X microscope objectives with numerical apertures (NA) of 0.4, 0.75, and 1.4, respectively. Resulting patterns were imaged with a confocal microscope, and 3D projections (Figure 2-7a-c) were constructed to measure the smallest possible thickness of fluorescent RGDS patterns within PEG-DA hydrogels. Patterns fabricated from the 0.4 NA objective resulted in an axial resolution of approximately 10 μm , while the 0.75 NA and 1.4NA objectives resulted in approximate axial resolution limits of 5.9 μm and 5.4 μm respectively (Figure 2-7d). It should be

noted that patterns created with larger numerical aperture objectives not only have higher axial resolution, but also show a sharper contrast between patterned and non-patterned regions in the axial dimension.

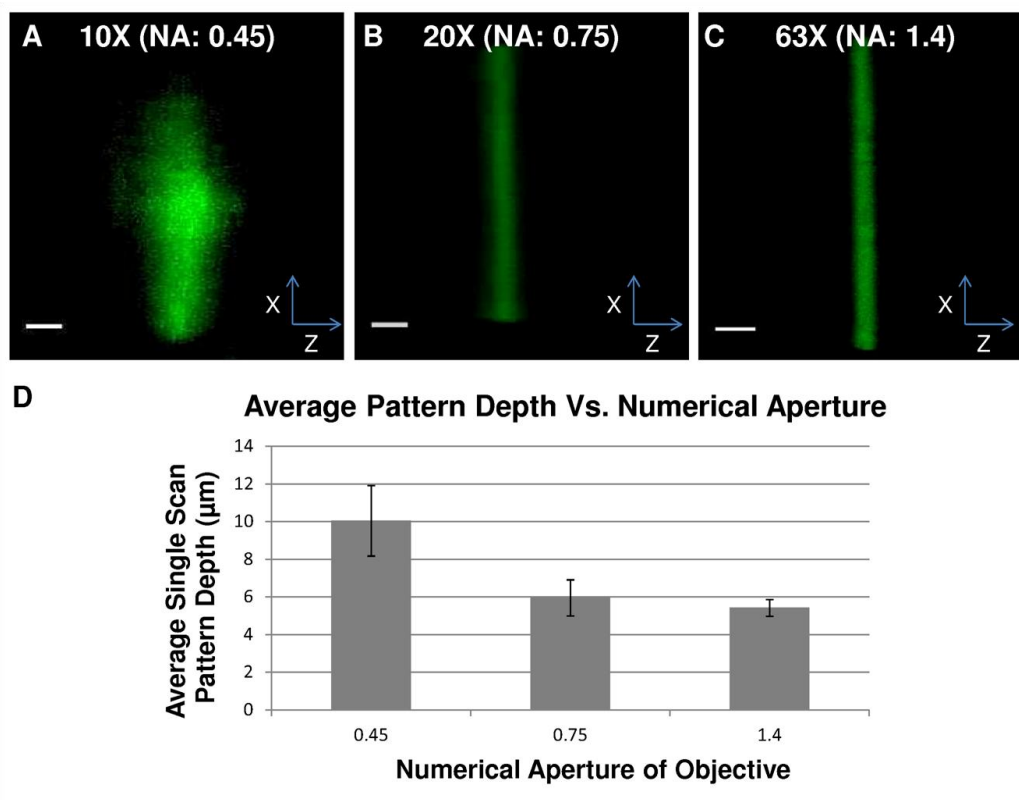


Figure 2-7: Axial Resolution of TP-LSL. (a-c). 3D projections of the axial resolution of patterned PEG-RGDS-Alexa fluor@488 within a PEG-DA hydrogel resulting from a single laser scan at one focal depth. Patterns created using (a) 10x objective with NA 0.45. (b) 20x objective with NA 0.75. (c) 63x objective with NA 1.4. All scale bars = 10 μm. (d) Plot of average pattern axial resolution from a single laser scan at a particular focal depth from objectives with a wide range of numerical apertures¹¹⁵.

2.3.3 Demonstration of the Three-Dimensionality of TP-LSL Patterns

To demonstrate the ability to pattern biomolecules such as RGDS into distinct, 3D forms, fluorescent RGDS was crosslinked into a spiral staircase pattern within a PEG-DA hydrogel (Figure 2-8). Specifically, 5 individual steps of the staircase were designed, each using a particular ROI. Each step was fabricated via 3 sequential scans of the 720

nm laser across the ROI, with each scan separated by a 3 μm increment in the axial direction. The axial resolution of TP-LSL within PEG-DA hydrogels is such that 3 scans separated by 3 μm forms a continuously patterned region. Between each step of the staircase, the focus was adjusted 6 μm axially and the new ROI was selected so that upon imaging with a confocal microscope, a projection was generated that allowed for the visualization of the three-dimensionality of the fluorescent RGDS staircase pattern within the PEG-DA hydrogel (Figure 2-8). It follows that TP-LSL may be further applied to confine biomolecules such as RGDS, or other peptides or proteins, to any desired 3D volume within a PEG-DA hydrogel network.

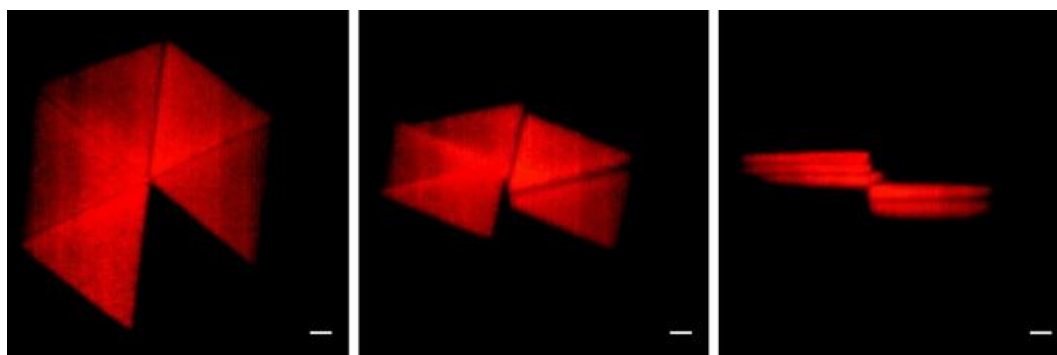


Figure 2-8: 3D Micropatterns via TP-LSL. 3D projections of patterned PEG-RGDS-Alexa fluor@488 within a PEG-DA hydrogel. All scale bars = 10 μm ¹¹⁵.

2.3.4 Controlling RGDS Concentration with Laser Scan Speed and Intensity

The LSM software allowed for increased versatility of TP-LSL in that the laser scan speed and laser intensity may be precisely specified to control the concentration of crosslinked RGDS. Patterns were created in which distinct ROIs were defined and each was patterned with a different laser scan speed. Three different Y-shaped ROIs were specified and patterned via the 720 nm laser at 3 distinct scan speeds with constant laser intensity. Specifically, the innermost region was patterned using a scan speed of 204

$\mu\text{sec}/\text{pixel}$, the middle region was patterned with a scan speed of $102 \mu\text{sec}/\text{pixel}$ and the outermost region was patterned with a scan speed of $51 \mu\text{sec}/\text{pixel}$. A fluorescence intensity profile of this pattern (Figure 2-9a) shows 3 distinct regions of fluorescence intensity in which longer laser dwell times on each pixel correlated with higher fluorescence intensity values. As the fluorescence intensity relates directly to the crosslinking of fluorescent RGDS molecules, TP-LSL provides a clear control of relative RGDS concentration within PEG-DA hydrogels. The degree of crosslinking of fluorescent RGDS may also be modified via laser intensity control. Figure 2-9b shows an array of 9 distinct square patterns of fluorescent RGDS within a PEG-DA hydrogel, each of which was fabricated via the selection of a unique combination of laser intensity and scan speed. Laser intensities utilized were $25 \text{ mW}/\mu\text{m}^2$, $21 \text{ mW}/\mu\text{m}^2$, and $17 \text{ mW}/\mu\text{m}^2$ while scan speeds were varied as described above. Fluorescence intensity measurements were taken for each patterned region and normalized to the pattern with the highest intensity (Figure 2-9c). It was shown that both laser intensity and scan speed have a direct correlation to patterned fluorescent RGDS, as fluorescence intensity values declined by up to 40 percent for decreasing scan speeds and decreasing laser intensities. The combination of laser intensity and scan speed may be referred to together as the applied energy over a given area or laser fluence. The designation of laser fluence specifies the amount of energy in the excitation focal volume, and therefore, positively correlates with the amount of crosslinking of acrylate-PEG-RGDS. Accordingly, this data relating laser scan speed and laser intensity to the fluorescence of RGDS (Figure 2-9c) may be utilized to pattern desired concentrations of biomolecules within hydrogel networks using TP-LSL.

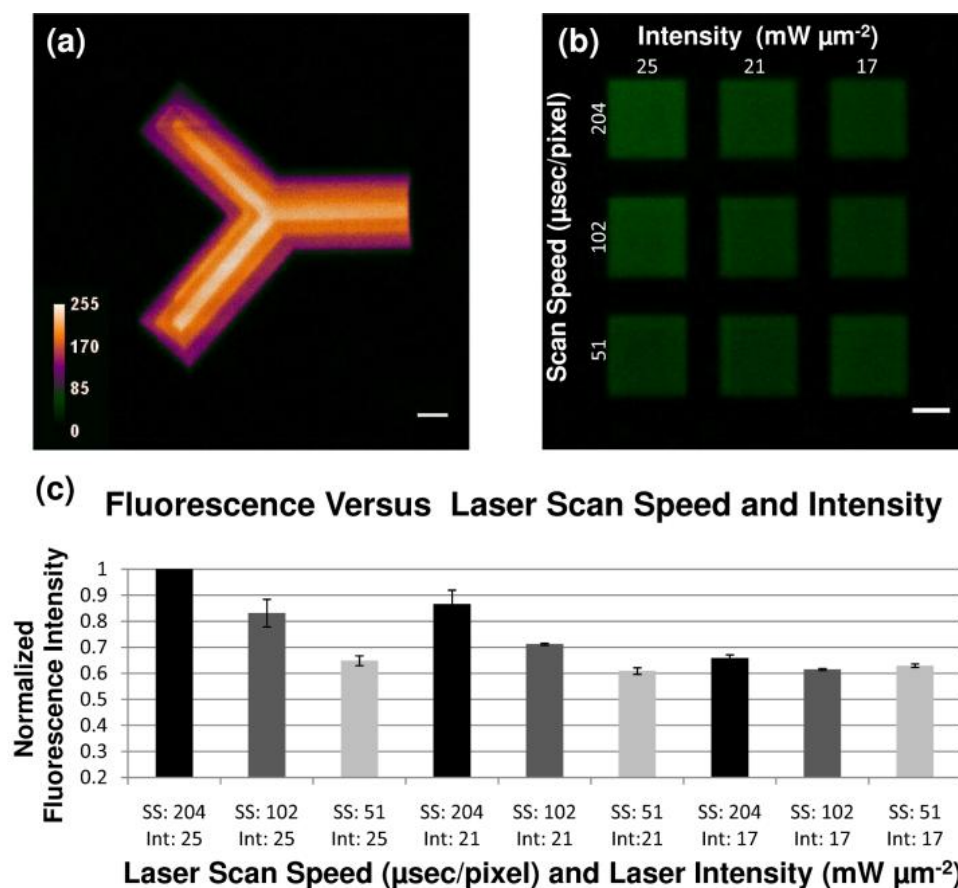


Figure 2-9: Controlling RGDS Concentration with Laser Scan Speed and Intensity. (a) Fluorescence intensity profile of patterned monoacrylate-PEG-RGDS-Alexafluor@488 with varying scan speeds. Outside pattern 204 $\mu\text{sec}/\text{pixel}$, middle pattern 102 $\mu\text{sec}/\text{pixel}$, and inside pattern 51 $\mu\text{sec}/\text{pixel}$. Scale bar = 25 μm . (b) Confocal fluorescent image of patterned monoacrylate-PEG-RGDS-Alexafluor@488 with varying scan speeds and laser intensities. Scale bar = 25 μm . (c) Plot of the effects of laser scan speed and intensity on observed normalized fluorescence of imaged pattern. Pattern with highest observed fluorescence normalized to 1¹¹⁵.

2.3.5 Patterning Multiple Fluorescent RGDS Variants

To show the feasibility of patterning multiple biomolecules into distinct 3D forms within a PEG-DA hydrogel network, several variants of fluorescent RGDS were utilized. PEG-RGDS-Alexa Fluor@488 was first allowed to diffuse into PEG-DA hydrogels and crosslinked into simple patterns via 720 nm light exposure across designed ROIs. Next, PEG-RGDS-Alexa Fluor@532 was allowed to diffuse into the gel, and a ROI juxtaposed

to the patterned PEG-RGDS-Alexa Fluor®488 was designed. After irradiation, the two different versions of fluorescent RGDS were observed side by side in a single PEG-DA hydrogel (Figure 2-10a). The versatility of TP-LSL was further demonstrated with the conjugation of a third fluorescent RGDS moiety, PEG-RGDS-Alexa Fluor®633 within the hydrogel. The 3 different varieties of PEG-RGDS were patterned in an overlapping manner so that there existed areas in which all 3 ligands were clearly present (Figure 2-10b-c).

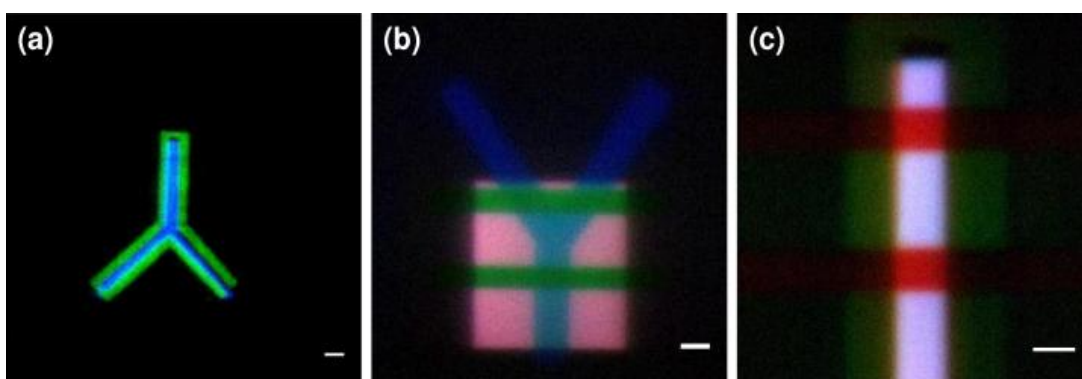


Figure 2-10: Patterning Multiple Fluorescent RGDS Variants. Confocal fluorescent images of patterns of multiple types of fluorescent monoacrylate PEG-RGDS within a PEG-DA hydrogel. (a) PEG-RGDS-Alexafluor®488 pattern juxtaposed to PEG-RGDS-Alexafluor®532 pattern. Scale bar = 25 μm . (b-c) PEG-RGDS-Alexafluor®488 pattern overlapping patterns of PEG-RGDS-Alexafluor®633 and PEG-RGDS-Alexafluor®532. Scale bars = 10 μm ¹¹⁵.

These fluorescent RGDS variants may also be patterned in a way that more explicitly demonstrates the inherent three-dimensionality of the TP-LSL strategy. To do this, each fluorescent RGDS variant was crosslinked into the gel at a unique axial depth. By changing the design of the ROI for each fluorescent RGDS variant, complex, 3D patterns were created in PEG-DA hydrogels utilizing different ligands. Figure 2-11 shows two such multi-ligand, 3D patterns after confocal imaging.

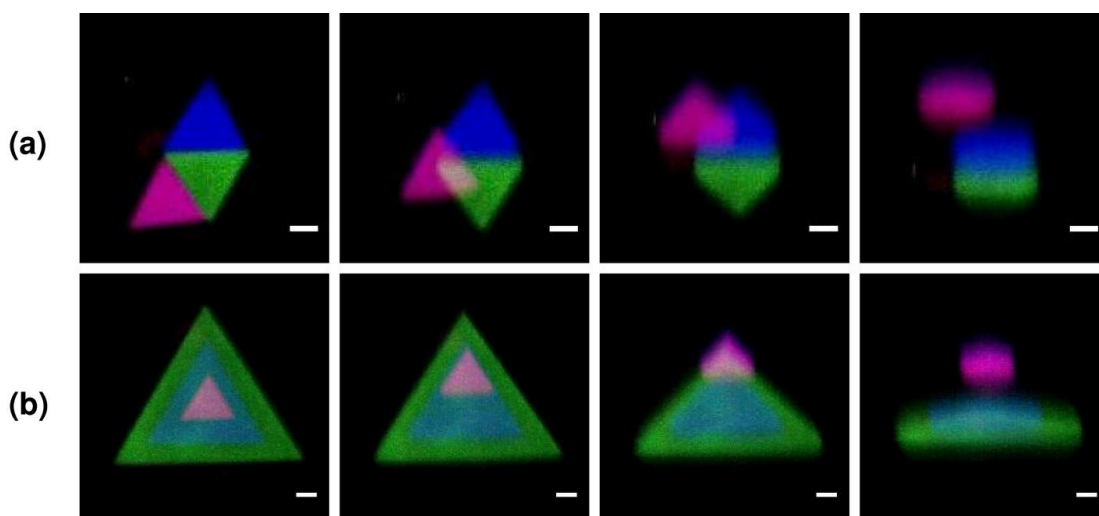


Figure 2-11: Patterning Multiple Fluorescent RGDSs Variants in 3D. (a-b) 3D projections of patterned PEG-RGDS-Alexa Fluor@488, PEG-RGDS-Alexa Fluor@633 and PEG-RGDS-Alexa Fluor@532. Images shown depict a single pattern viewed with an increasing angle of rotation. From left to right pattern is rotated 0°, 30°, 60°, and 90° away from the viewer. All Scale bars = 25 μm ¹¹⁵.

2.3.6 Patterning Different Bioactive Peptides within a Degradable Hydrogel

Microenvironment

To show the feasibility of fabricating a truly heterogeneous cellular microenvironment, two distinct, fibronectin-derived peptides, namely RGDS and CS-1, were patterned within a degradable PEG based hydrogel. Specifically, the peptide GGGPQGIWGQGK (abbreviated PQ) was synthesized and incorporated into an acrylate-PEG-PQ-PEG-acrylate macromer (abbreviated PEG-PQ). PEG-PQ hydrogels were then fabricated that were susceptible to degradation via cells secreting collagenase. PEG-RGDS-488 and PEG-CS-1-633 were next patterned into the degradable PEG-PQ gels in an iterative manner. In Figure 2-12, 3 distinct patterns of RGDS (green) and CS-1 (blue) within a degradable PEG-PQ hydrogel were imaged via confocal microscopy. Through

similar patterning of multiple bioactive adhesive ligands and growth factors within a single degradable hydrogel, TP-LSL may be utilized to design and engineer a variety of heterogeneous, 3D microenvironments within photosensitive, biodegradable materials.

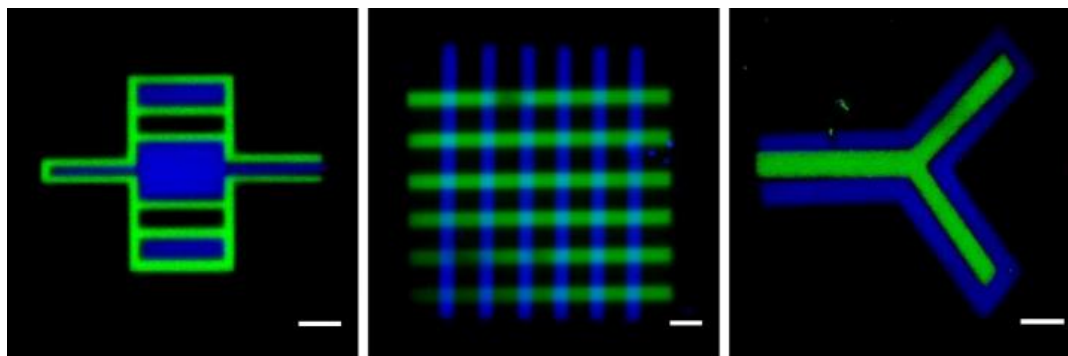


Figure 2-12: Patterning RGDS and CS-1 in a Degradable PEG Hydrogel. Confocal fluorescent images of patterns of PEG-RGDS- Alexafluor®488 (green) and PEG-CS-1- Alexafluor®633 (blue) within a collagenase degradable PEG-PQ hydrogel. All scale bars are 25 μm ¹¹⁵.

2.4 Discussion

The development of TP-LSL as a 3D microfabrication methodology has great potential to impact the field of bioengineering and biomedicine. Already, two-photon excitation technology has been utilized to pattern biomolecules within a variety of preformed photosensitive hydrogels^{45,58,98,113,116–118}. In several instances, a 3D biochemical cue has been presented to cells incorporated within TP-LSL patterned materials. For example, human dermal fibroblasts in a fibrin clot were first encapsulated in an enzymatically degradable PEG hydrogel⁵⁸. A branching micropattern of PEG-RGDS, approximately 100 μm in width, was then fabricated away from the clot using TP-LSL. Subsequent fibroblast migration was observed to be directly guided along the

micropattern as the cells extended processes and invaded only into regions of RGDS within the gel⁵⁸. TP-LSL has also been demonstrated to three-dimensionally direct neural cells¹¹⁸. Specifically, a scanning multiphoton laser and a digital micromirror device were utilized to crosslink biotinylated protein structures within hyaluroninc acid hydrogels¹¹⁸. An avidin-biotin bridge was then formed by washing in avidin followed by biotinylated biomolecules such as the cell adhesive IKVAV peptide. A set of 4 3D helixes decorated with the IKVAV peptide were fabricated in this manner and dorsal root ganglia cells were guided down the helix into the hydrogel.

While these works demonstrate the feasibility and promise of guiding cell behavior in hydrogels using a single, 3D patterned biochemical cue, they have yet to utilize the potential of the TP-LSL technique to guide cell motility and phenotype through the fabrication of complex physiological microenvironments. One reason for the low level of complexity thus far has been the lack of optimization of TP-LSL parameters and system capabilities. The work presented in this chapter has demonstrated the capability of two-photon laser patterning to create novel, cellular microenvironments consisting of multiple patterned biomolecules over a wide range of designated concentrations and 3D volumes.

Specifically, when designing a bioactive microenvironment, the maximum size range for pattern fabrication via TP-LSL was shown to be dependent on the field of view (in the XY lateral dimension) and the focal distance (in the Z dimension) of the objective through which the 720 nm laser passed. The choice of objective also correlated with the lateral and axial resolution of the TP-LSL patterning technique as the numerical aperture of the objective lens is a determinate of the two-photon excitation volume. Fabricated

patterns of biomolecules with minute feature size ($\sim 1 \mu\text{m}$) allowed for the creation of microenvironments highly relevant to individual cells. Future experiments will explore how small groups of cells respond to multiple types of adhesive ligands and growth factors presented on a 3D microscale. Further, detailed patterning over distances of hundreds of micrometers with large field of view objectives will allow for the control of cellular migration and phenotype to form basic 3D tissue structures. Fabricating patterns in a juxtaposed manner using a “quilt-work” type strategy will allow for the creation of biomolecule patterns across even larger volumes on the size order of human tissues.

Controlling the concentration of biomolecules within hydrogels, as demonstrated above, will also be crucial to cellular control. For example, while 2D cell migration has been studied in great detail, only recently have investigators begun to quantify 3D cell motility in response to biochemical factor presentation⁶⁹. The adjustment of laser scan speeds and intensities in TP-LSL will allow for the fabrication of 3D gradients of adhesive proteins and growth factors which can then be utilized to study the complex cellular migratory response. Additionally, nearly all cell types respond to unique concentrations of bioactive moieties, and the modulatable design of growth factor concentrations within biomaterials will allow for precise phenotypic control.

Perhaps even more essential to understanding complex cellular processes and recapitulating the *in vivo* cellular environment is the ability to three-dimensionally pattern multiple biomolecules of differing functionalities within a given biomaterial. This chapter demonstrates the robust capability of TP-LSL to accomplish this task as both the RGDS and CS-1 peptides were patterned within a single cellular microenvironment. RGDS, an amino acid sequence originally derived from the central cell binding domain of

fibronectin, and CS1, an amino acid sequence derived from the alternatively spliced type 3 connecting segment of fibronectin¹¹⁹, have both been utilized extensively to study cell behavior on a variety of 2D substrates. The patterning of these two peptides (as well as many other known adhesion proteins and peptides) into a degradable hydrogel will allow for the elucidation of novel relationships between adhesions sites and cell surface integrins with regards to cell proliferation and motility in 3D.

Additionally, there have been many reported cases where multiple bioactive factors work synergistically to produce a dramatic overall effect on cells. For example, the simultaneous surface presentation of fibrinogen and vascular endothelial growth factor (VEGF) gradients to endothelial cells has resulted in a four-fold increase in cell migration along the gradient compared with fibrinogen alone¹²⁰. Further, the combination of fibroblast growth factor (FGF)-2 and platelet derived growth factor (PDGF)-BB have been shown to synergistically induce stable vascular networks in an ischemic hind limb model¹²¹. The ability to pattern multiple growth factors, such as those listed above, into precise, 3D volumes will allow for the elucidation of novel synergetic relationships between biomolecules and will offer a high level of cellular phenotypic control. TP-LSL will also provide a means to pattern juxtaposed biomolecules that attract and affect differing cell types, and thus, allow for the organization of cells into three-dimensionally designed physiological microstructures.

Recently, other researchers have implemented the system capabilities and parameters of TP-LSL developed and presented within this chapter in order to begin introducing cells to more complex microenvironments. For example, high affinity binding proteins streptavidin/biotin and barstar/barnase were utilized with TP-LSL to

facilitate the 3D patterning of multiple bioactive proteins within an agarose hydrogel¹²². To do this, streptavidin and barnase were sequentially immobilized in unique micropatterns via two photon chemistry within an agarose hydrogel. The fusion proteins barstar-sonic hedgehog(SHH) and biotin-ciliary neurotrophic factor (CNTF) were next synthesized. The fusion proteins were then simply washed into the gel and immediately bound by their micropatterned binding partner, thus facilitating the control of bioactive proteins in 3D¹²². Neural precursor cells were then seen to be three-dimensionally guided within these gels to a depth of 85 micrometers. Researchers have also recently used TP-LSL to pattern a 3D gradient of vascular endothelial growth factor (VEGF) in agarose hydrogels¹²³. This was achieved using a macro program that continually increased laser power as patterning progressed in the Z dimension. When seeded on the surface of the hydrogels, primary brain microvascular endothelial cells were seen to form tubule like structures and three-dimensionally migrate over 200 μm down an optimal VEGF gradient¹²³. As research continues, TP-LSL will allow for the design of 3D patterned microenvironments with increasing complexity, ultimately allowing for the guidance of complex cellular structures, such as the microvasculature.

2.5 Conclusion

Cells in their natural environment respond to a myriad of protein signals that are presented within a 3D matrix. The signals are presented with micrometer precision over a large array of sizes. The signals also vary greatly with respect to their concentration throughout complex 3D volumes. In this work, we demonstrate the capability of two-photon laser scanning lithography (TP-LSL) to allow for the creation of complex cellular microenvironments with precise control of all these factors. Specifically, we

demonstrated the ability to fabricate patterns from 1 μm to nearly 1 mm in lateral size, and with an axial resolution of approximately 5 μm . We further showed the ability to pattern different concentrations of the adhesive ligand RGDS based on modulation of laser scanning properties. Finally, we demonstrated the ability to engineer 3D patterns of different types of biomolecules, first via the use of different fluorescent variants of RGDS, and then through the micropatterning of both RGDS and CS-1 within a single biodegradable, photosensitive hydrogel. The development of these abilities has enhanced the value of TP-LSL as a patterning technique and should lead the way towards the design and fabrication of heterogeneous, 3D cellular microenvironments for a variety of biomimetic applications. This thesis will now discuss the implementation of these TP-LSL patterning abilities to probe the fundamentals of cell migration, with the results both providing insight into how cells move and organize in three dimensions, as well as serving as a stepping stone toward using TP-LSL technology to guide cellular organization for tissue engineering applications.

Chapter 3: Quantitative Investigation of Cell Migration in PEG-Based Hydrogels using Two-photon Laser Scanning

Lithography

3.1 Introduction

Cell motility is critical for a variety of purposes within healthy human physiology. For example, embryonic development, wound healing, angiogenesis, and the regulation of the immune system are just some of the processes that rely on the ability of cells to migrate within the native extracellular matrix¹²⁴. Additionally, abnormal cell migratory behaviors are implicated in a number of devastating conditions including vascular disease, osteoporosis, multiple sclerosis, and metastatic cancer¹²⁴. An in-depth understanding of cell motility is therefore critical for applications ranging from tissue engineering to disease pathology and drug discovery. In this chapter, two-photon laser scanning lithography (TP-LSL) is utilized in combination with PEG-based hydrogels to define a new system to study cell motility and to begin to parse out the complex factors that dictate cell migration.

Much of what is known about cell migration is based upon observations of cells cultured on tissue culture plastic¹²⁵. Cells have been observed to migrate via the extension of protrusions (lamellipodia or filopodia), which utilize integrins to form adhesions to molecules in the extracellular matrix (e.g. fibronectin or laminin). These adhesions result in a cascade of intracellular events, one of which results in the generation of pulling forces on the actin cytoskeleton at the leading edge of the polarized cell body (Figure 3-1)¹²⁶. Simultaneously, adhesions at the trailing edge of the cell are dismantled and the cell begins to move forward.

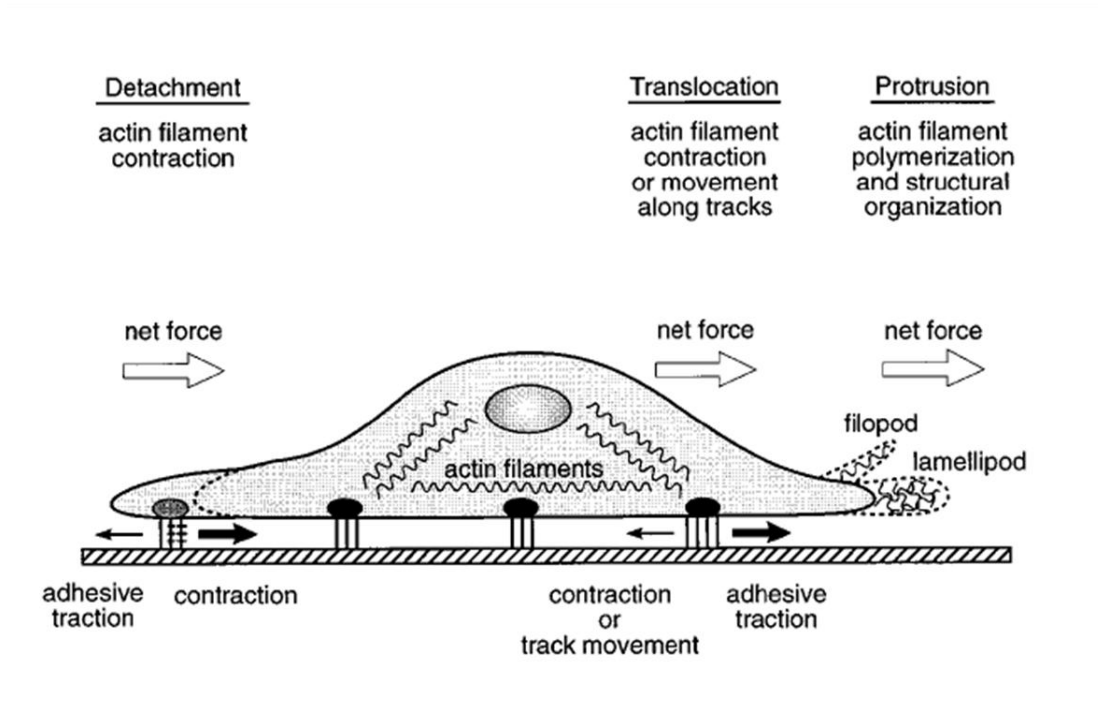


Figure 3-1: Illustration of the Forces Involved in Cell Migration. Protrusions (lamellipodia or filopodia) are formed via actin polymerization. These protrusions form adhesions to the substrate (black ovals represent focal adhesions). These adhesions create traction forces that generate an overall net force in the direction of cell migration. These adhesions also stimulate translocation of the cell body. Eventually, the magnitude of the generated traction forces are greater than the adhesive traction at the rear of the cell, resulting in the cell moving forward. Adapted from Lauffenburger and Horwitz¹²⁶.

Early researchers also determined that the concentration of adhesion molecules had a direct effect on cell migratory speed. In one study, various concentrations of fibronectin adsorbed onto glass were shown to have a biphasic effect on the migration speed of Chinese hamster ovary (CHO) cells, with the maximum migration speed occurring at an intermediate ligand concentration¹²⁷. This biphasic dependence was a result of the balance of forces between the leading cell edge attachment and the trailing cell edge detachment. Researchers have also observed a biphasic dependence of cell

migration speed on materials with differing mechanical properties, with maximal speeds occurring on materials of intermediate stiffness¹²⁸. Further, studies have demonstrated that cells migrating on softer 2D surfaces require a higher density of cell adhesion molecules to maintain maximum cell speed¹²⁸.

While 2D studies were a valuable first step to understanding cell motility, cells within the body do not migrate on flat, non-deformable surfaces. Rather, cells exist within a 3D microenvironment that regulates migration via a number of interconnected physical and biochemical mechanisms. In order to better mimic this complex microenvironment, scientists have moved towards the use of biomaterial systems to study cell motility. As discussed in Section 1.10, researchers have used biomaterials to observe dramatic differences between cells migrating on 2D surfaces and cells migrating within 3D matrices. For example, Cukierman et al. demonstrated that cells on a cell-derived 3D extracellular matrix migrated 1.5 times faster and with a less spread morphology when compared with cells cultured on 2D tissue culture plastic⁶⁸. Additionally, Zaman et al. showed that as 3D Matrigel matrices were softened, human prostate carcinoma cells migrated at maximal speeds when fewer adhesion molecules were present⁶⁹. This migration trend is in direct contrast with two-dimensional migration studies and is likely explained by the forces a 3D matrix places on all cell surfaces, with fewer stiff surfaces serving as a better environment for matrix degradation, remodeling, and subsequent motility⁶⁹.

While these results clearly demonstrate a difference between 2D and 3D cell migration, natural ECM matrices provide very little ability to control and tune matrix properties, making it difficult to parse out the factors responsible for differences in

motility. Cell migration in the native extracellular matrix can be linked to at least 5 different factors, namely adhesion molecules, chemotactic growth factors, matrix stiffness, matrix porosity, and the proteolytic susceptibility of the matrix¹²⁴. In collagen or Matrigel environments, increasing the stiffness of the hydrogel material is accomplished by increasing the overall percent weight of the hydrogel material. In addition to increasing the stiffness of the material, however, such a hydrogel would also have significantly altered adhesive ligand concentration, pore size, diffusion of growth factors, and proteolytic susceptibility. Further, studies comparing 2D cell migration on one material (e.g. tissue culture plastic) and 3D cell migration within a different material (e.g. Matrigel) are confounded by differences in biochemical growth factors present within a naturally derived matrix.

Bioactive PEG-based hydrogels may allow for the elucidation of many of these confounding factors¹²⁹. Enzymatically degradable PEG-PQ hydrogels are naturally non-adhesive and act as a blank slate into which custom bioactivity may be introduced. This property of these hybrid materials eliminates the confounding factor of unknown growth factor presentation to cells. The PEG-based hydrogel system also allows for the independent tuning of gel stiffness and adhesion molecule concentration via the incorporation of various quantities of adhesion peptides such as PEG-RGDS^{129,130}. Additionally, PEG-PQ hydrogels offer opportunities for photochemical fabrication of specifically designed geometrical patterns of PEG-RGDS to guide cell migration in both 2 and 3 dimensions on the same bioinert material. For example, previous studies have developed and optimized a technique known as two-photon laser scanning lithography (TP-LSL) (Section 1-16) in order to crosslink PEG-RGDS into 3D forms within PEG-PQ

hydrogels¹¹⁵. This technique involves permeating a hydrogel with PEG-RGDS (or any other acrylate-PEG-biomolecule), using a two-photon laser to covalently crosslink the PEG-RGDS into desired 3D forms, and then washing away unbound PEG-RGDS. This procedure results in high-resolution, 3D volumes of patterned bioactivity within the hydrogel network.

TP-LSL has been utilized previously to guide some simple behaviors of cells. For example, work by Hahn *et al.* showed that cell migration could be restricted to a 3D, patterned area of PEG-RGDS¹¹³. Similarly, Lee *et al.* demonstrated direct guidance of fibroblast migration via 3D PEG-RGDS channels within enzymatically degradable PEG-based hydrogels⁵⁸. While these works demonstrate the feasibility and promise of guiding cell behavior in hydrogels using a single, 3D patterned biochemical cue, they have yet to utilize the potential of the TP-LSL technique to study cell motility over various micropatterned conditions.

In this chapter, TP-LSL is implemented for the first time to guide and quantitatively study cell motility. Specifically, PEG-RGDS micropatterns of controlled size and concentration were fabricated both on the surface of non-degradable PEG-DA hydrogels and within the center of PEG-PQ hydrogels. HT1080 cells were then seeded onto micropatterned PEG-DA hydrogels (2D) or encapsulated directly adjacent to micropatterned PEG-PQ hydrogels (3D), and subsequent cell migration was observed. The PEG-RGDS patterns guided cell migration, allowing for the direct tracking of individual cells within a controlled microenvironment. 2D and 3D cell migration were directly compared in terms of cell speed, cell persistence and cell shape. Patterns of various size and volume were also utilized to manipulate cell persistence and guide cells

on the microscale. Finally, the cell migratory effects of varying factors such as PEG-RGDS ligand concentration and PEG-PQ hydrogel composition were analyzed to probe the confounding factors of cell migration. Overall, the incorporation of TP-LSL with PEG-based hydrogels serves as a novel tool to investigate cell motility within precisely designed biomimetic microenvironments. The studies presented in this chapter begin to elucidate many of the interwoven factors that affect how cells move within the extracellular matrix and lead the way toward a more complete understanding of cell motility.

3.2 Materials and Methods

3.2.1 Synthesis of Acrylate-PEG-Derivatives

The RGDS peptide (American peptide) was reacted overnight with acrylate-poly(ethylene glycol)-succinimidyl valerate (PEG-SVA) at a 1.2:1 (RGDS:PEG-SVA) molar ratio in HEPBS conjugation buffer in order to form acrylate-PEG-RGDS (PEG-RGDS). HEPBS conjugation buffer consisted of 20 mM n-(2-Hydroxyethyl)piperazine-N'-(4-butanesulfonic acid) (Santa Cruz Biotechnology), 100 mM sodium chloride, 2 mM calcium chloride, and 2 mM magnesium chloride at pH 8.5. To synthesize enzymatically degradable PEG hydrogel precursors, the peptide GGGPQGIWGQGK (abbreviated PQ) was first synthesized (Section 2.2.2) and then reacted overnight with PEG-SVA at a 1:2.1 (PQ:PEG-SVA) molar ratio in HEPBS conjugation buffer to form acrylate-PEG-PQ-PEG-acrylate (PEG-PQ). The resultant PEG-RGDS and PEG-PQ products were purified via dialysis and analyzed via GPC as described in Section 2.2.2.

3.2.2 Cell Maintenance

HT1080s (ATCC) were maintained in culture with Eagle's minimal essential medium (EMEM) (ATCC) supplemented with 10 % fetal bovine serum, 2 mM L-glutamine, 1 U/ml penicillin, and 1 $\mu\text{g/ml}$ streptomycin. Cells were cultured at 37 °C with 5% CO₂ and the media was replenished every 2 days. Cells were used from passages 2- 6.

3.2.3 Ninhydrin Assay

Hydrogel molds were assembled using a glass slide exposed to Sigmacoat (Sigma), two 750 μm PDMS spacers, and a methacrylate-modified coverslip (see Section 2.2.4 for methacrylation of glass coverslips). 6 μl of a hydrogel precursor solution consisting of 5% PEG-DA (6000 Da, see Section 2.2.1 for synthesis) with 3.4 $\mu\text{l/ml}$ NVP, 1.5 % v/v triethanolamine (Fluka BioChemika) and 10 μM eosin Y (Sigma) in HBS was injected into the hydrogel mold. Each gel was exposed to white light (Fiberlite, Dolan Jenner) for 25 s to form crosslinked, immobilized hydrogels. Gels to be patterned were soaked in 20 mM PEG-RGDS with 10 $\mu\text{l/ml}$ of 300 mg/ml DMAP in NVP for 15 min. The hydrogels were then patterned using TP-LSL (Section 1.16) with the same laser parameters that were later utilized to pattern gels for cell migration studies (720 nm wavelength with a 60 $\text{mW}/\mu\text{m}^2$ laser intensity and a 12.5 $\mu\text{s}/\text{pixel}$ laser scan speed). A total volume of 0.75 mm^3 was patterned within each hydrogel with a laser scan occurring every 3 μm in the Z direction to create continuous patterns. Hydrogels were washed in HBS for 2 days with at least 4 buffer changes to remove unpatterned PEG-RGDS.

In order to determine the concentration of PEG-RGDS crosslinked into the hydrogel via TP-LSL, a standard curve was created in which each standard reference point contained a non-patterned PEG-DA hydrogel, as well as a known concentration of

PEG-RGDS. Concentrations of PEG-RGDS used for standards were 125, 93.75, 32.25 and 0 μM . Standards and samples were frozen and lyophilized overnight to remove photoinitiator noise. All standards and samples were then incubated with hydrochloric acid at 150°C for 12 h to dissolve the hydrogels and to break up peptides into individual amino acids. The samples and standards were then placed on the rotovap to remove all HCl. Samples and standards were then dissolved in 0.1 M sodium citrate (pH 5), sonicated, centrifuged, and mixed with the Ninhydrin reagent at a 1:1 ratio. Samples and standards were then boiled for 20 min, before their absorbance was read at 570 nm. Assay of each standard and patterned sample was conducted in triplicate. To calculate the patterned ligand concentration, the number of moles of PEG-RGDS was interpolated using the PEG-RGDS standard curve. This number of moles was then divided by the patterned volume to obtain the final pattern concentration, which was then compared to the original 20 mM PEG-RGDS soaking concentration to estimate the conjugation efficiency of TP-LSL.

3.2.4 Fabrication of PEG-RGDS Patterns to Guide 2D Cell Migration

Methacrylate groups were covalently linked to glass coverslips as previously described (Section 2.2.4). A hydrogel precursor solution of 5% PEG-DA (molecular weight 6000 Da) with 3.4 $\mu\text{l/ml}$ NVP, 1.5 % v/v triethanolamine (Fluka BioChemika) and 10 μM eosin Y (Sigma) was made in HBS. Two 380 μm polydimethylsiloxane (PDMS) spacers were pressed against a glass slide that had been incubated in Sigmacoat (Sigma). A methacrylated coverslip was then sealed against the PDMS spacers to form a hydrogel mold. 6 μl of hydrogel precursor solution was injected into the mold and

exposed to white light (Fiberlite, Dolan Jenner) for 25 s, yielding a crosslinked, non-degradable, PEG-DA hydrogel.

Immobilized PEG-DA hydrogels were incubated in 5 mM PEG-RGDS in HBS along with 50 μ M PEG-RGDS-633 (see Section 2.2.3 for synthesis) and 10 μ l/ml of 300 mg/ml DMAP in NVP for 15 min. (In experiments where variation of PEG-RGDS was tested, the soaking concentrations contained either 0.5 mM, 1 mM, 5 mM, or 20 mM PEG-RGDS). The hydrogels were then placed on the stage of a Zeiss LSM 710 Multi-photon microscope and patterned via TP-LSL (Section 1.16). Four rectangular regions of interest were designated, with lengths of 500 μ m and widths of 10, 25, 50, and 100 μ m, respectively. The microscope was then focused on the hydrogel surface, and a titanium/sapphire laser was tuned to 720 nm and set with an intensity of 60 mW/ μ m² and a laser scan speed of 12.5 μ s/pixel. Scanning over the regions of interest resulted in precise excitation of photoinitiator molecules and subsequent crosslinking of PEG-RGDS to the PEG-DA hydrogel surface in the exact shape specified by the regions of interest. To ensure PEG-RGDS was crosslinked to the surface of the hydrogel, the laser was scanned every 3 μ m for a distance 51 μ m above and below the perceived hydrogel surface. On each patterned hydrogel, the stage was translated so that 3 sets of rectangular patterns were fabricated that were connected by larger (600 x 600 μ m) patterned squares (Figure 3-2). These square PEG-RGDS micropatterns served as larger areas upon which cells could adhere and then migrate onto smaller PEG-RGDS micropatterns of interest. After laser scanning, patterned hydrogels were washed in HBS under gentle rocking for 48 h with at least 4 buffer changes to remove unbound PEG-RGDS.

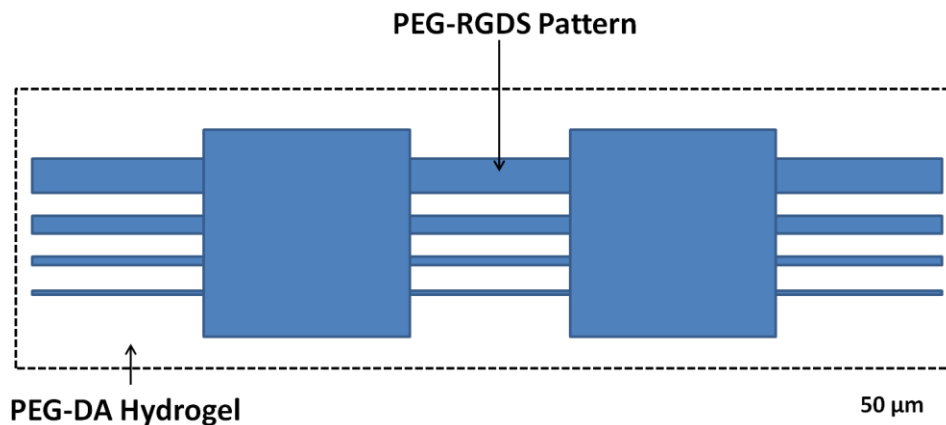


Figure 3-2: Diagram of PEG-RGDS Pattern on Surface of PEG-DA Hydrogel. TP-LSL was utilized to fabricate rectangular and square micropatterns of PEG-RGDS (blue) onto the surface of a PEG-DA hydrogel. 3 sets of 4 rectangles were patterned with the rectangles having dimensions of 500 μm in length and 100, 50, 25, and 10 μm in width. The rectangular patterns were connected via large square patterns of PEG-RGDS with 600 x 600 μm dimensions. These patterns were then used to monitor controlled HT1080 migration on hydrogel surfaces.

3.2.5 Seeding and Visualization of HT1080s on 2D PEG-RGDS Surface Patterns

HT1080s at approximately 90% confluency were fluorescently labeled via a 1 h incubation with 1 μg/ml green CMFDA Cell Tracker® (Invitrogen) in EMEM. After incubation, cells were washed with PBS and fresh media was added. HT1080s were then harvested and seeded onto PEG-DA hydrogels whose surfaces had been patterned with PEG-RGDS. HT1080s were seeded at cell densities of 70,000 cells/cm² for hydrogels patterned using 20 mM PEG-RGDS, 90,000 cells/cm² for hydrogels patterned using 5 mM PEG-RGDS and 110,000 cells/cm² for hydrogels patterned using 0.5 mM and 1 mM PEG-RGDS. After seeding, cells were incubated in fresh media and allowed to adhere. After 24 h, the hydrogels were washed gently with PBS to remove non-adherent cells and imaged. The migration of HT1080s on PEG-DA hydrogel surfaces was monitored using a confocal microscope (Zeiss5 LIVE, Plan-Apochromat 20x objective with 0.8 numerical

aperture: for green CMFDA Cell Tracker excitation = 489 nm, emission BP filter = 500–525 nm; for Alexafluor 633 excitation = 633 nm, emission long pass filter = 650 nm).

Time-lapse microscopy was performed with an image being acquired every 2 min for 6 h.

The hydrogels were maintained at 37°C with 5 % CO₂ throughout image acquisition.

3.2.6 Fabrication of PEG-RGDS Patterns to Guide 3D Cell Migration

Hydrogel molds were assembled using a glass slide exposed to Sigma coat, 380 μm thick PDMS spacers, and a methacrylate-modified coverslip as described previously. 6 μl of hydrogel precursor solution consisting of 5% PEG-PQ with 3.4 μl/ml NVP, 1.5 % v/v triethanolamine (Fluka BioChemika) and 10 μM eosin Y (Sigma) in HBS was injected into the mold. 10% PEG-PQ was also utilized to study the effects of hydrogel composition. The molds were then exposed to white light (Fiberlite, Dolan Jenner) for 25 s forming immobilized PEG-PQ hydrogels. These hydrogels were incubated in 5 mM PEG-RGDS in HBS, along with 50 μM PEG-RGDS-633 (see Section 2.2.3 for synthesis) and 10 μl/ml of 300 mg/ml DMAP in NVP for 15 min. (In experiments where variation of PEG-RGDS was tested, the soaking concentrations contained either 1 mM, 5 mM, or 20 mM PEG-RGDS). The hydrogels were then patterned via TP-LSL. Four rectangular regions of interest were once again selected, with lengths of 500 μm and widths of 10, 25, 50, and 100 μm, respectively (Figure 3-3a). The microscope was focused in a middle axial plane of the hydrogel, and a titanium/sapphire laser irradiating at 720 nm with a 60 mW/μm² laser intensity and a 12.5 μs/pixel laser scan speed was utilized to crosslink PEG-RGDS into the designed structures. Care was taken to ensure that each pattern reached all the way to the lateral edge of the gel to allow for cell migration.

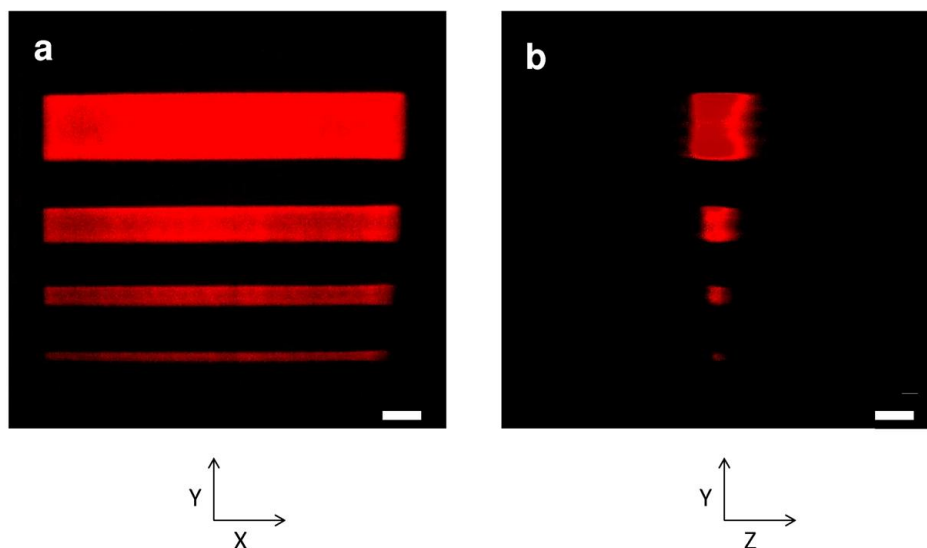


Figure 3-3: 3D Patterns of PEG-RGDS Vary in Width and Height. PEG-RGDS micropatterns within a PEG-PQ hydrogel are shown. (a) Straight on (XY) view of micropatterns showing a constant 500 μm length and various widths of 100, 50, 25, and 10 μm . (b) Cross sectional (YZ) view of micropatterns showing that the patterns have controlled widths and heights. From top to bottom the YZ dimensions of the patterns are 100 x 100 μm , 50 x 50 μm , 25 x 25 μm , and 10 x 10 μm . Scale bar = 50 μm .

The depth of each pattern was also varied. The 100 μm wide pattern was iteratively scanned with a 3 μm adjustment between each scan until the pattern depth reached 100 μm . The 50 μm , 25 μm and 10 μm patterns were fabricated in a similar way so that final pattern dimensions were: 100 x 100 x 500 μm , 50 x 50 x 500 μm , 25 x 25 x 500 μm , and 10 x 10 x 500 μm (Figure 3-3b). After laser scanning, patterned hydrogels were washed in HBS under gentle rocking for 48 h with at least 4 buffer changes to remove unbound PEG-RGDS.

3.2.7 Guiding Cell Migration into 3D PEG-RGDS Micropatterns

HT1080s at approximately 90 % confluency were fluorescently labeled (as described in Section 3.2.5) with green CMFDA cell tracker® (Invitrogen). A hydrogel

precursor solution of 10 % PEG-PQ with 3.4 $\mu\text{l/ml}$ NVP, 1.5 % v/v triethanolamine (Fluka BioChemika) 10 μM eosin Y (Sigma) and 3.5 mM PEG-RGDS (synthesis described in Section 3.2.1) was made in HBS. Fluorescently labeled HT1080s were harvested using a standard trypsin/EDTA solution and suspended in the precursor solution with a cell density of 30,000 cells/ μl . Hydrogel molds were fabricated using a 380 μm thick PDMS spacer and a glass slide exposed to Sigmacoat®. The coverslip with the attached patterned hydrogel was placed face down onto the spacer so that a mold was formed between the spacer and the existing patterned hydrogel. 6 μl of the cell-containing precursor solution was injected into the mold and exposed to white light (Fiberlite, Dolan Jenner) for 25 s, yielding a crosslinked, cell-laden PEG-PQ hydrogel directly adjacent to the PEG-PQ hydrogel with patterned PEG-RGDS (Figure 3-4). The hydrogels were then immersed in EMEM and maintained at 37°C and 5% CO₂ for 12 h to allow cells to adhere and begin migration into the hydrogel with patterned PEG-RGDS. The 3D migration of HT1080s was monitored using a Zeiss 5 LIVE confocal microscope (Zeiss5 LIVE, Plan-Apochromat 20x objective with 0.8 numerical aperture: for green CMFDA Cell Tracker excitation = 489 nm, emission BP filter = 500–525 nm; for Alexafluor 633 excitation = 633 nm, emission long pass filter = 650 nm). Time-lapse microscopy was performed with a z stack of images being acquired every 10 minutes for 6 h. The hydrogels were maintained at 37°C with 5 % CO₂ throughout image acquisition.

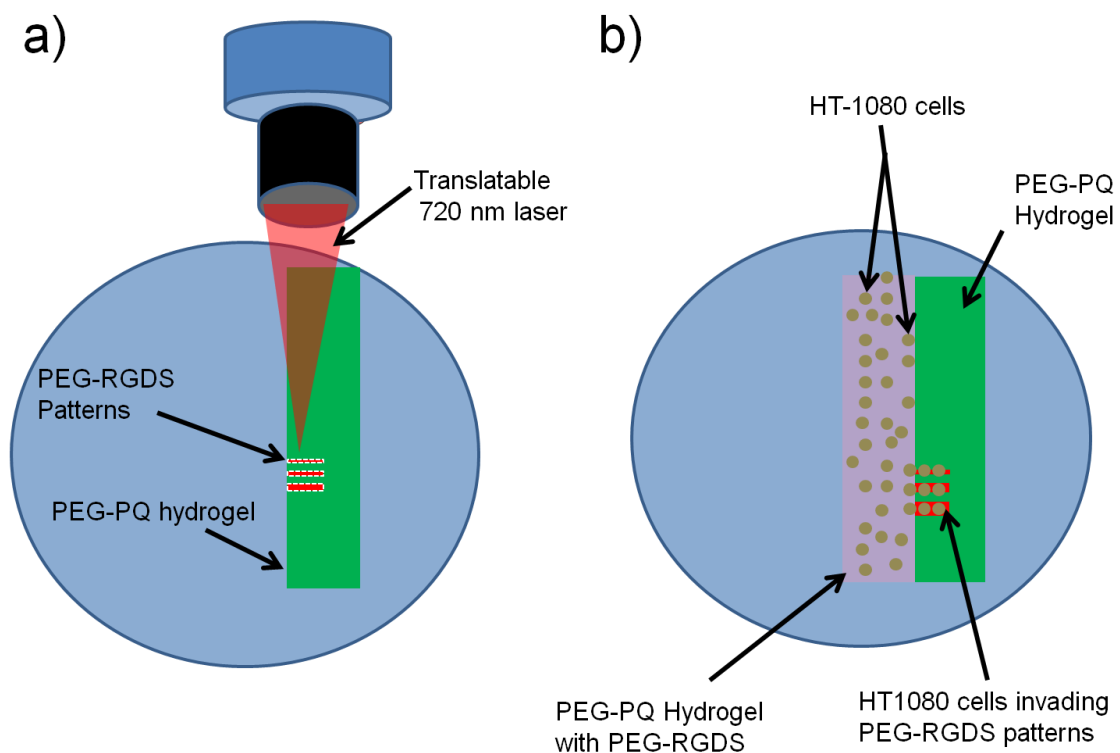


Figure 3-4: Guiding HT1080s into PEG-RGDS Micropatterns within PEG-PQ Hydrogels. (a) PEG-RGDS patterns of various dimensions (red) were fabricated using two-photon laser scanning lithography within an immobilized PEG-PQ hydrogel (green) (b) HT1080s were photoencapsulated within a different PEG-PQ hydrogel with PEG-RGDS throughout (purple). The cellularized hydrogel was immobilized directly adjacent to the patterned hydrogel, and HT1080s were observed to migrate into PEG-RGDS patterns.

3.2.8 Staining Nuclei and F-Actin to Visualize Cell Structure

After 18 h in culture, gels were incubated in 4% paraformaldehyde for 20 min and then washed with PBS. The gels were incubated in 0.5% Triton X-100 for 30 min to permeabilize the cells, and then washed again with PBS. To block non-specific binding, the gels were incubated 1% bovine serum albumin (BSA) in PBS for 30 min. After incubation, the gels were washed in PBS and incubated in 2 μ M DAPI with 1:100 rhodamine phalloidin (Invitrogen) in PBS for 12 h. Cell structure within hydrogels was

then visualized on a confocal microscope (Zeiss5 LIVE, Plan-Apochromat 20x objective with 0.8 numerical aperture: for rhodamine phalloidin excitation = 532 nm, emission BP filter = 560–675 nm; for DAPI excitation = 405 nm, emission band pass filter = 415-580 nm).

3.2.9 Analysis of Cell Migration

The migration of HT1080s was analyzed using Imaris (Bitplane) software. Cells were tracked using an autoregressive motion gapclose 3 algorithm. All cells that were tracked for at least 2 h were considered for analysis. With the exception of the experiment that varied pattern width, cells were analyzed on or within 100 μm wide patterns. Imaris was used to calculate average cell migration speed, average cell persistence, and average cell guidance ratio. Cell migration speed was defined as the total distance a cell traveled divided by the total time (Equation 3-1). Cell persistence was defined as the total cell displacement from its starting position divided by the total distance a cell traveled (Equation 3-2). Cell guidance ratio was defined as the total distance a cell travels in the direction parallel to the pattern divided by the total distance a cell travels (Equation 3-3). Cell area and cell circularity were calculated using ImageJ (National Institutes of Health) to analyze images of HT1080s fixed and stained with DAPI and phalloidin (Section 3.2.8). This analysis was performed by first tracing the perimeter of each cell. Cell area was then calculated as the total number of square micrometers within the cell tracing. Cell circularity was also calculated (Equation 3-4). The value of cell circularity reflects how closely a cell resembles a circle. A cell circularity of 1 indicates a perfect circle while a value approaching 0 indicates an increasingly elongated polygon.

$$\text{Migration Speed} = \text{Cell Distance Traveled} \div \text{Migration Time}$$

Equation 3-1: Cell Migration Speed.

$$\text{Persistence} = \text{Cell Displacement} \div \text{Cell Distance Traveled}$$

Equation 3-2: Cell Persistence.

$$\text{Migration Ratio} = \text{Cell Distance Traveled Parallel to Pattern} \div \text{Cell Distance Traveled}$$

Equation 3-3: Cell Migration Ratio.

$$\text{Circularity} = (4 \times \pi) \times (\text{Cell area} \div \text{Cell Perimeter}^2)$$

Equation 3-4: Cell Circularity

HT1080s were evaluated for cell speed, cell persistence, cell guidance ratio, cell area, and cell circularity under a variety of conditions. Cells migrating on 2D surfaces were compared to those migrating within 3D hydrogels. Cells were also analyzed on or within various pattern widths, various PEG-RGDS concentrations, various PEG hydrogel compositions, and at various time points. When comparing more than 2 groups, one-way ANOVA and subsequent post hoc analysis via the Bonferonni method was used to statistically analyze differences. When comparing only 2 groups, a student's T test was utilized to determine significance. In all cases, P values of < 0.05 were considered significant.

3.3 Results

3.3.1 Quantification of PEG-RGDS Concentration in TP-LSL Patterned Hydrogels

The overarching goal of this chapter was to develop TP-LSL as a tool to investigate many of the confounding factors that influence cell migration. In order to utilize TP-LSL as a technique to micropattern biomaterials for the quantitative study of cell motility, it was first necessary to assess the final concentration of PEG-RGDS crosslinked into PEG-based hydrogels. A ninhydrin-based assay was utilized to quantitate the amount of RGDS crosslinked within a designated volume of a PEG-DA hydrogel. The ninhydrin chemical, otherwise known as 2,2-dihydroxyindane-1,3-dione, reacts with free amines to produce a deep purple colored product, with the number of amines present correlating linearly with the absorbance of the solution at 570 nm. The ninhydrin assay was performed by first creating a set of PEG-RGDS standards. The PEG-RGDS standards were then dissolved in a strong acid to degrade the peptides into individual amino acids with free amines. The standards were reacted with the ninhydrin reagent and the absorbance was read at 570 nm in order to create a standard curve relating absorbance to PEG-RGDS concentration (Figure 3-5a).

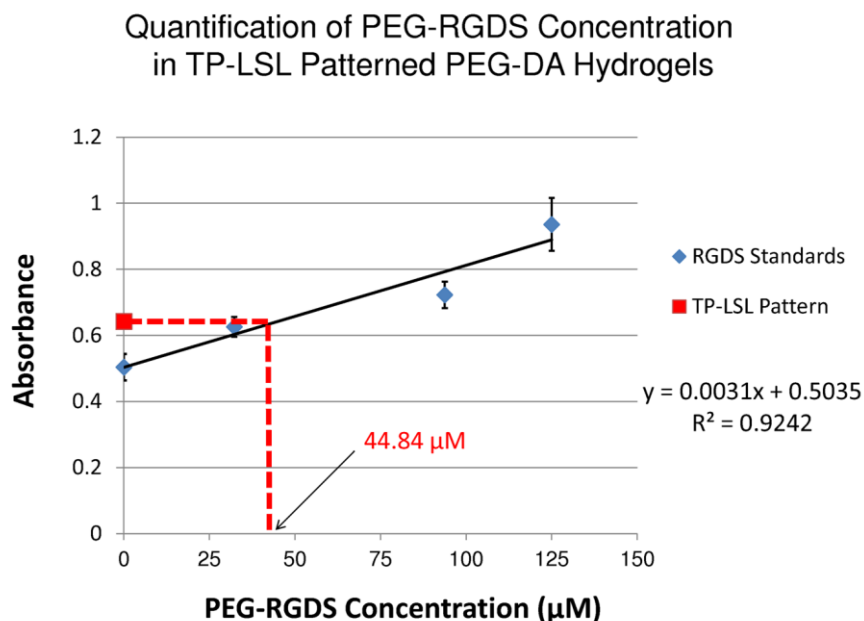


Figure 3-5: Quantification of PEG-RGDS Concentration in TP-LSL Patterned Hydrogels. 5% PEG-DA hydrogel samples were fabricated and permeated with 20 mM PEG-RGDS. TP-LSL was then used to pattern a 0.75 mm³ volume of PEG-RGDS within each hydrogel. Standards with various known amounts of PEG-RGDS were also made. Standards and samples were reacted with the Ninhydrin reagent at a total volume of 0.05 ml and assayed for absorbance at 570 nm. Standards were used to create a curve which was fitted with a linear equation in order to determine how much PEG-RGDS was present in the patterned samples. The concentration of PEG-RGDS within the patterned region was shown to be 2.98 mM. This amounts to a conjugation of approximately 15% of the original PEG-RGDS soaking solution.

Patterned samples were next obtained by soaking 20 mM PEG-RGDS into PEG-DA hydrogels and using TP-LSL to pattern a volume of 0.75 mm³. After rinsing, the patterned hydrogels were similarly dissolved in acid, reacted with Ninhydrin, and assayed for absorbance at 570 nm. This absorbance reading was then applied to the standard

curve of PEG-RGDS to determine the concentration of PEG-RGDS (Figure 3-5a). The concentration of PEG-RGDS within the 0.75 mm^3 patterned volume was then calculated and determined to be 2.98 mM PEG-RGDS. This functional PEG-RGDS concentration indicates that approximately 15% of the original 20 mM PEG-RGDS that was soaked into the PEG-DA hydrogels was covalently conjugated using the TP-LSL patterning process. For the remainder of this chapter, a 15% conjugation efficiency was utilized to approximate conjugation at conditions that were below the detection limits of the ninhydrin assay.

3.3.2 Comparing 2D and 3D Cell Migration using TP-LSL and PEG-Based Hydrogels

In order to investigate the inherent differences between 2D and 3D cell migration, cell motility on and within micropatterned PEG-based hydrogels was investigated. In all cases, the fibrosarcoma-derived HT1080 cell line was utilized. HT1080s are commonly used to study cell motility in 3D¹³¹⁻¹³³, and the results of the current studies using HT1080s may be directly compared to the previously reported literature. Further, HT1080s are a highly invasive cancer cell line that can be employed to study the unique migratory behaviors of metastatic tumor cells¹³². Finally, HT1080s migrate rapidly and release large amounts of proteases, including MMP-2 and MMP-9,¹³³ which allows for significant 3D migration through PEG-PQ hydrogels within a relatively short 6 h time period.

To investigate 2D cell migration, $100 \times 500 \text{ }\mu\text{m}$ wide regions of PEG-RGDS were micropatterned onto the surface of 5% PEG-DA (6000 Da) hydrogels. Fluorescently labeled HT1080s were then seeded onto the patterned hydrogel surfaces, allowed to

adhere for 12 h, and monitored for cell migration via time-lapse confocal microscopy. To probe 3D cell migration, 100 x 100 x 500 μm regions of PEG-RGDS were micropatterned within 5% PEG-PQ hydrogels, with the pattern extending to the peripheral edge of the hydrogel. Fluorescently labeled HT1080s were then encapsulated within a separate PEG-PQ hydrogel directly adjacent to the 3D micropatterned hydrogel. Cells were allowed to adhere and migrate into the PEG-RGDS micropatterns for 12 h before samples were taken to a confocal microscope to monitor cell migration via time-lapse microscopy. A soaking concentration of 5 mM PEG-RGDS with an immobilized PEG-RGDS concentration of 750 μM was utilized for both 2D and 3D patterning.

Representative images of labeled HT1080s migrating in 2D and 3D PEG-RGDS micropatterns are shown in Figure 3-6a. In both cases, the movement of each cell was tracked over a 6 h period with the passage of time indicated by the changing color of the tracking lines with early times indicated by blues and reds and later times indicated by yellows and whites (Figure 3-6a). Cells migrating on non-degradable PEG-DA surfaces changed their position in only the X and Y dimensions while cells migrating within enzymatically degradable PEG-PQ hydrogels changed position in the X, Y, and Z dimensions. An analysis of cell speed indicated that HT1080s migrated over 5 times faster on 2D hydrogel surfaces than within 3D PEG-PQ hydrogels (80 $\mu\text{m}/\text{h}$ for 2D, 14 $\mu\text{m}/\text{h}$ for 3D) (Figure 3-6b).

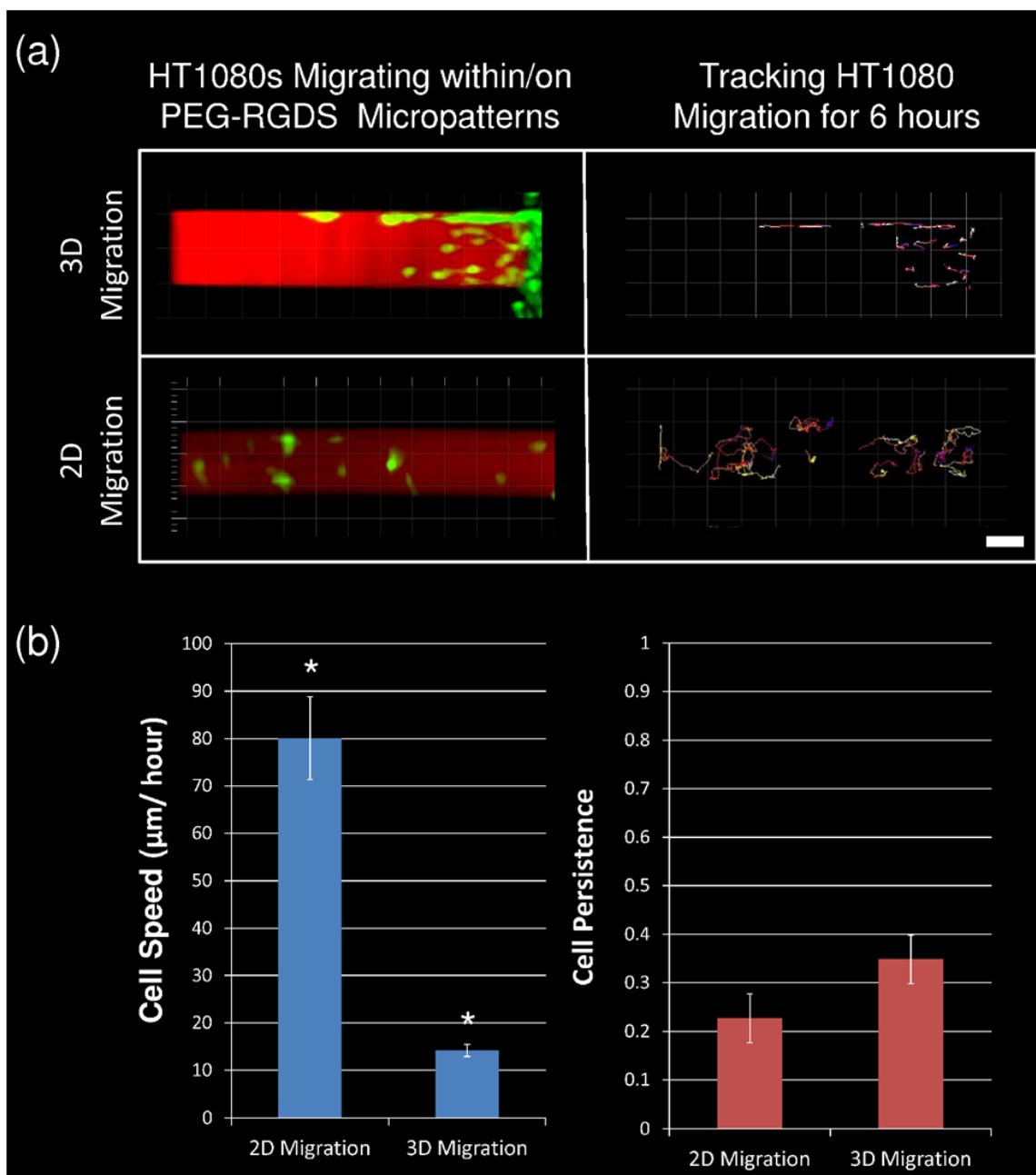


Figure 3-6: Differences in Cell Speed and Persistence between 2D and 3D Cell Migration. (a) HT1080s (green) are depicted migrating within a PEG-PQ hydrogel (3D) or on the surface of a PEG-DA hydrogel (2D) 1 day after cell seeding. HT1080s are confined to a 100 μm wide pattern of PEG-RGDS (red). HT1080 cells were tracked for 6 h with the passage of time indicated by color changes from blue to red to yellow to white. All images are representative. Scale bar = 50 μm . (b) Cell tracking data was used to calculate cell speed and cell persistence for both 2D and 3D cell migration. Cell speed was seen to be significantly increased with 2D migration ($*p < 0.05$), while cell persistence trended higher with 3D migration.

An analysis of how much cell movement contributed to total cell displacement, known as cell persistence, was also performed. Average cell persistence was seen to trend higher in 3D as opposed to on 2D surfaces, although this difference was not statistically significant (Figure 3-6b). This indicates that the cells may persist in the same direction longer when migrating within a matrix than when migrating on a surface. A closer investigation of the size and shape of the migrating HT1080s was next conducted. Migrating cells on both 2D hydrogel surfaces and within 3D hydrogels were fixed and stained with DAPI and phalloidin to visualize the nuclei and actin cytoskeleton (Figure 3-7a). HT1080s were observed to be smaller and more elongated in 3D than they were on 2D surfaces. These differences were quantified in terms of total cell area and cell circularity (Figure 3-7b). Average cell area decreased from $36 \mu\text{m}^2$ on 2D hydrogel surfaces to $18 \mu\text{m}^2$ within 3D hydrogels. Cell circularity, which measures how closely a cell approximates a circle, dropped from nearly 0.7 to 0.4 (with 1 representing a perfect circle).

This experiment quantitatively demonstrates the striking differences between 2D and 3D cell migration. Specifically, cells migrate faster and with a more spread morphology on 2D surfaces than they do within a 3D matrix. This experiment also demonstrates the feasibility of using TP-LSL patterns to study cell motility, leading the way for an array of novel experiments to probe how cells move within precisely designed biomaterial microenvironments.

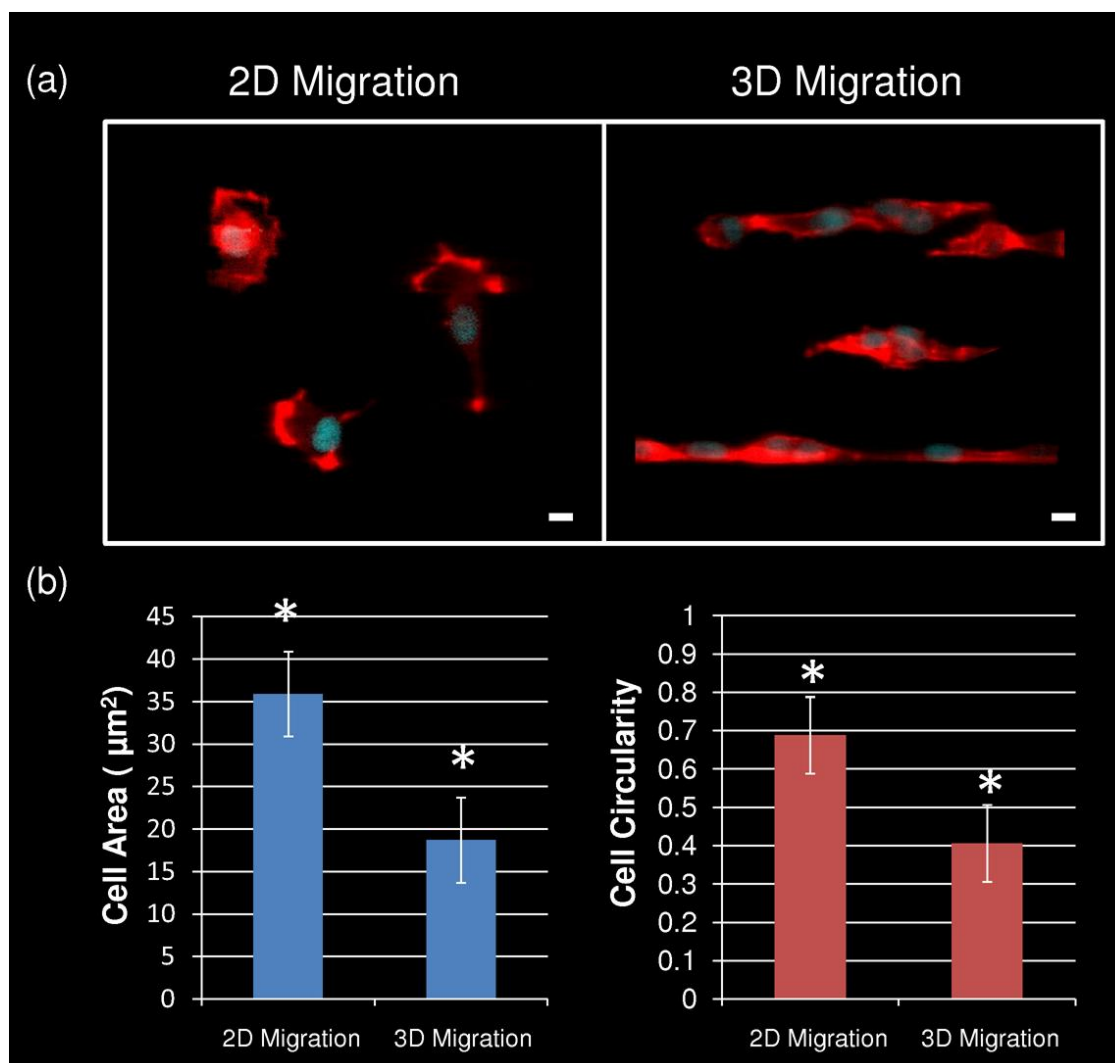


Figure 3-7: Differences in Cell Size and Shape between 2D and 3D Cell Migration.

HT1080s were seeded onto PEG-DA surfaces (2D) with PEG-RGDS micropatterns. HT1080s were also encapsulated adjacent to PEG-PQ hydrogels with PEG-RGDS micropatterns. (a) Cells were allowed to migrate for 12 h on/within PEG-RGDS patterns before they were stained with DAPI and phalloidin to visualize the nuclei and actin cytoskeleton. All images are representative. Scale bar = 10 μm . (b) Cell area and cell circularity were quantified for both 2D and 3D cell migration. Total cell area and overall cell circularity were significantly greater for cells on 2D hydrogel surfaces as compared to cells migrating through micropatterned 3D hydrogels. (* $p < 0.05$)

3.3.3 Controlling 2D and 3D Cell Migration with PEG-RGDS Patterns of Varying Size

TP-LSL was utilized to micropattern PEG-RGDS tracks of various sizes in order to apply an increasing degree of control to the migratory path of mobile cells in both 2 and 3 dimensions. Specifically, to guide 2D cell migration, PEG-RGDS was patterned into four rectangular regions with lengths of 500 μm and widths of 10, 25, 50, and 100 μm , respectively. For 3D migration, patterns contained the same lengths and widths, but also varied in their height so that the final pattern dimensions were: 100 x 100 x 500 μm , 50 x 50 x 500 μm , 25 x 25 x 500 μm , and 10 x 10 x 500 μm (Figure 3-3). A soaking concentration of 5 mM PEG-RGDS with a functional PEG-RGDS concentration of 750 μM was utilized for both 2D and 3D patterning. Fluorescently labeled HT180s were seeded onto the micropatterned PEG-DA hydrogels to observe 2D cell migration. To observe 3D migration, fluorescent HT180s were encapsulated directly adjacent to 3D PEG-RGDS micropatterns.

Representative images show that the PEG-RGDS micropatterns successfully applied an increasing degree of control on HT1080 cell migration in both 2D and 3D (Figure 3-8a). Cells were tracked for 6 h and their migration paths were confined to the area (2D) or volume (3D) of micropatterned PEG-RGDS. Migration tracks of cells are shown in the normal straight on view (XY) as well as a side view (YZ) (Figure 3-8a). The YZ view demonstrates how HT1080s migrating in 3D are confined to their PEG-RGDS micropattern in both the XY dimension and the YZ dimension. Cells migrating on the smallest 3D PEG-RGDS patterns (10 x 10 x 500 μm) are so limited in the yz direction that their tracks begin to resemble straight lines similar to those of cells migrating on the smallest 2D micropatterns.

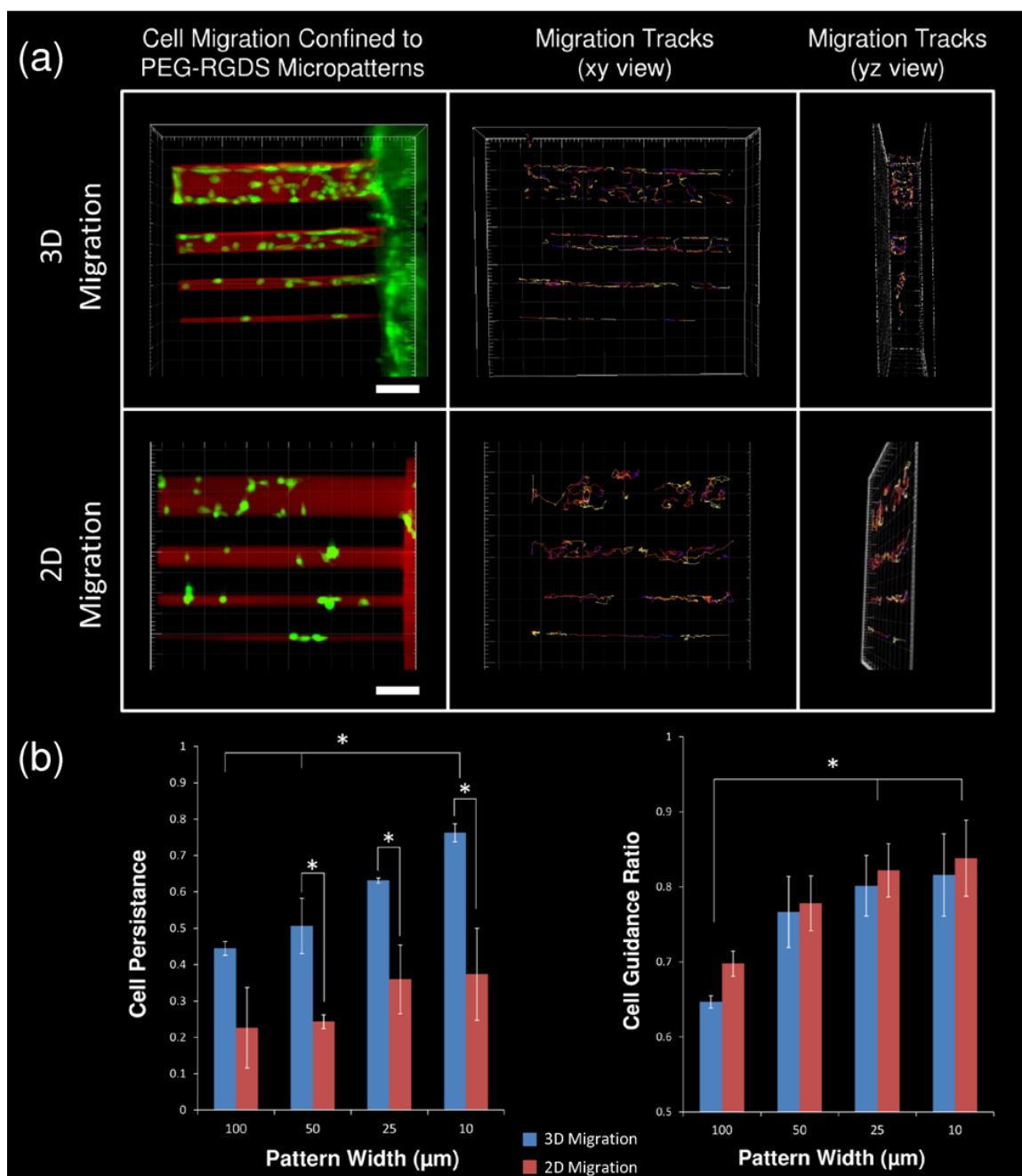


Figure 3-8: Guiding Cell Migration with PEG-RGDS Micropatterns of Varying Size. (a) In 3D, HT1080s (green) were guided within PEG-PQ hydrogels by patterns of PEG-RGDS (red) that vary in width and height. In 2D, HT1080s were guided on the surface of PEG-DA hydrogels by patterns of PEG-RGDS that vary in width. HT1080 cells were then tracked for 6 h with the passage of time indicated by color changes from blue to red to yellow to white. All images are representative. Scale bar = 100 μm. (b) Cell tracking data was used to calculate cell persistence and cell guidance ratio for both 2D and 3D cell migration. Both cell persistence and cell guidance ratio were significantly increased as pattern dimensions decreased. Cell persistence was significantly greater for 3D migration while there was no significant difference in cell guidance ratio between 2D and 3D migration. (* $p < 0.05$).

In order to quantitatively analyze the effects of changing the size of PEG-RGDS micropatterns, cell persistence and cell migration ratio were analyzed. The persistence of cells migrating within 3D hydrogels was seen to increase significantly as the pattern dimensions were decreased. A similar trend was present for cells migrating on 2D hydrogel surfaces, although considerably less pronounced. This trend is expected as the decreasing pattern dimensions influence the cells to progress farther in a given direction, thereby increasing the contribution of their distance traveled to their overall displacement. Interestingly, cell persistence was markedly decreased on patterned 2D hydrogel surfaces as opposed to within 3D hydrogels.

The cell guidance ratio measures how well the cells are guided in the direction of the pattern, regardless of ultimate cell displacement. The cell guidance ratio for cells migrating in both 2D and 3D increased as pattern dimensions were decreased. In this case, however, the discrepancy between 2D and 3D cell migration was no longer present. Specifically, the cell guidance ratio between 2D and 3D cell migration was statistically identical for all of the different sized patterns. The combination of the persistence and migration ratio results indicate that while cells in 2D and 3D are both increasingly guided by the micropatterns of smaller dimensions, cells on 2D surfaces have a higher tendency to reverse their migration direction than those in 3D. After reversing direction, 2D cells continue to migrate parallel to the pattern but have a decreased displacement, resulting in decreased persistence while at the same time maintaining a high cell guidance ratio. Overall, this experiment has demonstrated the ability of TP-LSL to guide cell migration with high precision and stands as an example of the types of studies scientists can conduct to test the effects of micropatterned geometries on cell motility.

3.3.4 Variation of PEG-RGDS Concentration to Manipulate Cell Migration

The use of TP-LSL and PEG-based hydrogels allows for the independent modulation of PEG-RGDS concentration to manipulate cell migration. In this section, the effect of various PEG-RGDS concentrations on cells migrating on hydrogel surfaces (2D) and within enzymatically degradable hydrogels (3D) is examined. For 2D migration, PEG-DA hydrogels were surface patterned with PEG-RGDS and seeded with HT1080s. For 3D migration, PEG-PQ hydrogels were patterned with PEG-RGDS patterns on the periphery, and HT1080s were encapsulated directly adjacent to those patterns. Hydrogels (for both 2D and 3D) were patterned using various soaking concentrations to achieve a range of functional PEG-RGDS concentrations. Specifically, hydrogels were patterned with 0.5 mM, 1 mM, 5 mM, and 20 mM soaking concentrations of PEG-RGDS resulting in functional PEG-RGDS concentrations of 75 μ M, 150 μ M, 750 μ M, and 3000 μ M, respectively. Cell migration was then observed via time-lapse microscopy, and each cell was analyzed for cell speed and cell persistence. HT1080s migrating on 2D surfaces were observed to be significantly affected by changing PEG-RGDS concentration. Specifically, cell speed varied biphasically, with the maximum cell speed occurring at intermediate PEG-RGDS concentrations (Figure 3-9a). This observation is in agreement with previous studies of 2D cell migration that report a biphasic dependence of cell speed on adhesive molecule concentration due to the balance of forces between leading cell edge attachment and the trailing cell edge detachment^{127,129}.

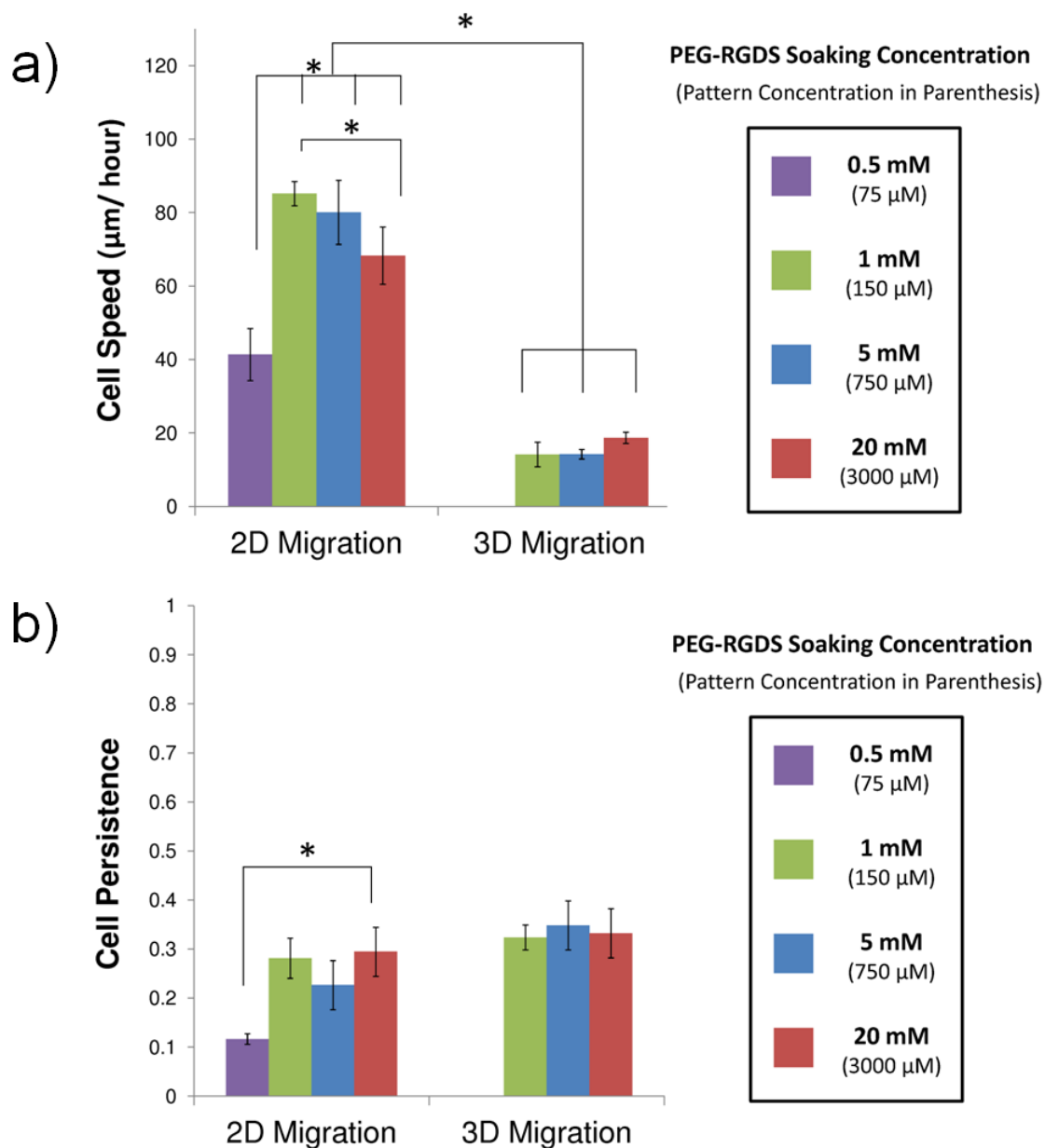


Figure 3-9: Cell Speed and Persistence as a Function of PEG-RGDS Concentration.

In 2D, HT1080s were tracked while migrating on PEG-DA surfaces with 100 μm wide patterns of various PEG-RGDS concentrations. In 3D, cells were tracked while migrating within PEG-PQ hydrogels with 100 x 100 μm patterns of various PEG-RGDS concentration. The initial soaking concentrations of PEG-RGDS are displayed with the functional concentration of patterned PEG-RGDS below in parenthesis. (a) Cell speed in 2D was seen to have a biphasic dependence on PEG-RGDS concentration while cell speed in 3D did not depend on PEG-RGDS concentration. Cell speed was higher in 2D than in 3D for every PEG-RGDS concentration. (b) Cell persistence was seen to increase in 2D between low and high PEG-RGDS concentrations. PEG-RGDS concentration did not affect cell persistence in 3D. Cell persistence trended higher in 3D than in 2D. (* $p < 0.05$).

In agreement with previous results, migration speed was significantly lower for 3D cell migration than 2D cell migration at every tested PEG-RGDS concentration. However, the cell speed of HT1080s migrating in 3D was not greatly influenced by PEG-RGDS as it was in 2D. When examining cell persistence (Figure 3-9b), cells on 2D surfaces exhibited a lower persistence at the lowest concentration of PEG-RGDS, but a persistence trend was not detected above this low threshold level. The persistence of HT1080s migrating in 3D was also not significantly related to changes in PEG-RGDS concentration.

An analysis of the size and shape of the migrating HT1080s was next performed. Specifically, migrating cells on 2D hydrogel surfaces with each of the PEG-RGDS concentrations were fixed and stained with DAPI and phalloidin to visualize the nuclei and actin cytoskeleton (Figure 3-10a). HT1080s were smaller and more circular on low concentrations of PEG-RGDS and became increasingly larger and irregular as the PEG-RGDS concentration was increased. These differences were quantified in terms of total cell area and cell circularity (Figure 3-10b-c). Average cell area increased from $26 \mu\text{m}^2$ on the lowest tested PEG-RGDS concentration to $47 \mu\text{m}^2$ on the highest tested PEG-RGDS concentration. The average cell circularity decreased from 0.8 on the low PEG-RGDS concentration to below 0.5 on the high PEG-RGDS concentration (with 1 representing a perfect circle). These differences in cell size and shape likely result from increased spreading of cells on surfaces with higher concentrations of PEG-RGDS.

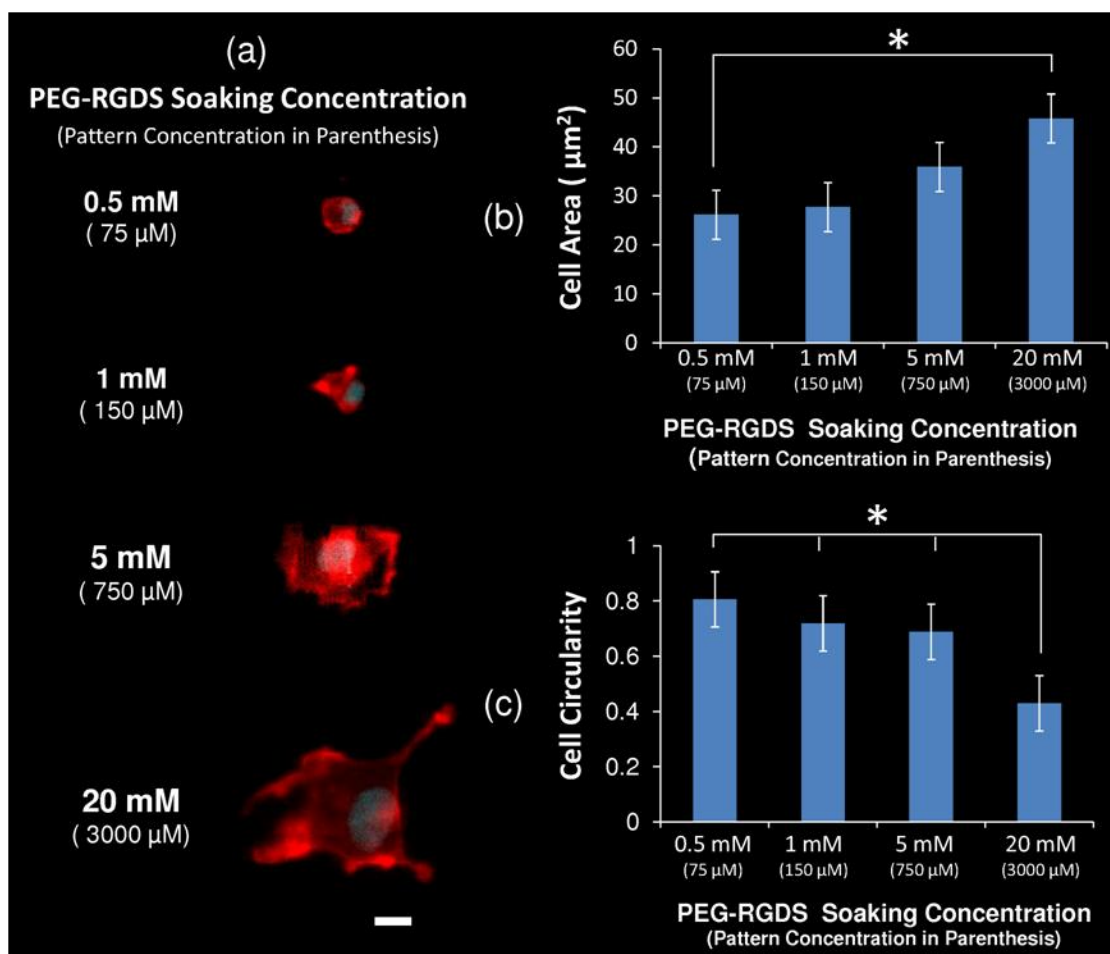


Figure 3-10: PEG-RGDS Concentration Affects Cell Morphology on 2D PEG-DA Surfaces. HT1080s were seeded onto PEG-DA hydrogels that were micropatterned with various concentrations of PEG-RGDS. The initial soaking concentrations of PEG-RGDS are displayed with the functional concentration of patterned PEG-RGDS below in parenthesis. (a) Cells were allowed to migrate for 12 h on each of the PEG-RGDS patterns before they were stained with DAPI and phalloidin to visualize the nuclei and actin cytoskeleton. All images are representative. Scale bar = 10 μ m. (b-c) Cell area and cell circularity were quantified as a function of PEG-RGDS concentration. On higher concentrations of PEG-RGDS, cells exhibited significantly increased total areas while overall cell circularity significantly decreased. (* $p < 0.05$).

In contrast to 2D migration, the size and shape of cells migrating in 3D did not vary significantly with PEG-RGDS concentration. In these samples, nearly all observed cells appeared similarly small and elongated as they migrated through the PEG-PQ hydrogels (see Figure 3-7 for size and shape of 3D cell migration). While variation of PEG-RGDS concentration did not affect 3D cell migration in terms of cell migration speed, cell persistence, or cell shape, a significant dependence was observed in terms of total displacement of the leading cell into the PEG-RGDS pattern. Specifically, migrating HT1080s were imaged for each different PEG-RGDS concentration exactly 12 h after cell encapsulation next to the 3D micropatterns (Figure 3-11a). The leading cell (the cell which had migrated farthest into the pattern) invaded a significantly greater distance into the pattern at an intermediate concentration of PEG-RGDS (750 μM functional concentration) than at either a high or low PEG-RGDS concentration. Upon quantification, the displacement of leading cell migration in an intermediate PEG-RGDS micropattern was determined to be over 300 μm . Contrastingly, the leading cell in the high PEG-RGDS concentration migrated 220 μm into the pattern while the leading cell in the low PEG-RGDS concentration migrated only 115 μm . This biphasic dependence of maximal leading cell displacement on PEG-RGDS concentration may reflect that leading cells are better able to degrade and migrate through the PEG-PQ hydrogel when ligated by an intermediate concentration of adhesive ligand. A similar result was reported by Gobin *et al.* who utilized a modified Boyden chamber assay to demonstrate that more human dermal fibroblasts migrated the required distance when an intermediate concentration of PEG-RGDS was used¹²⁹. The leading cell displacement results in the current study as well as the results reported by Gobin *et al.* focus only on the farthest cells

migrating at an end point of the assay. In each of these cases, leader cells degrade a pathway within the matrix for later migrating cells to follow. These later migrating cells likely moved through the matrix with an approximately equivalent speed and persistence that was no longer directly related to PEG-RGDS concentration. Overall, this study has shown the ability to modulate the cell adhesive ligand concentration within micropatterns. This control is independent from other confounding factors such as mechanical stiffness and biochemical stimulation and demonstrates how cells respond to increasing amounts of adhesive molecules within a biomimetic, micropatterned environment.

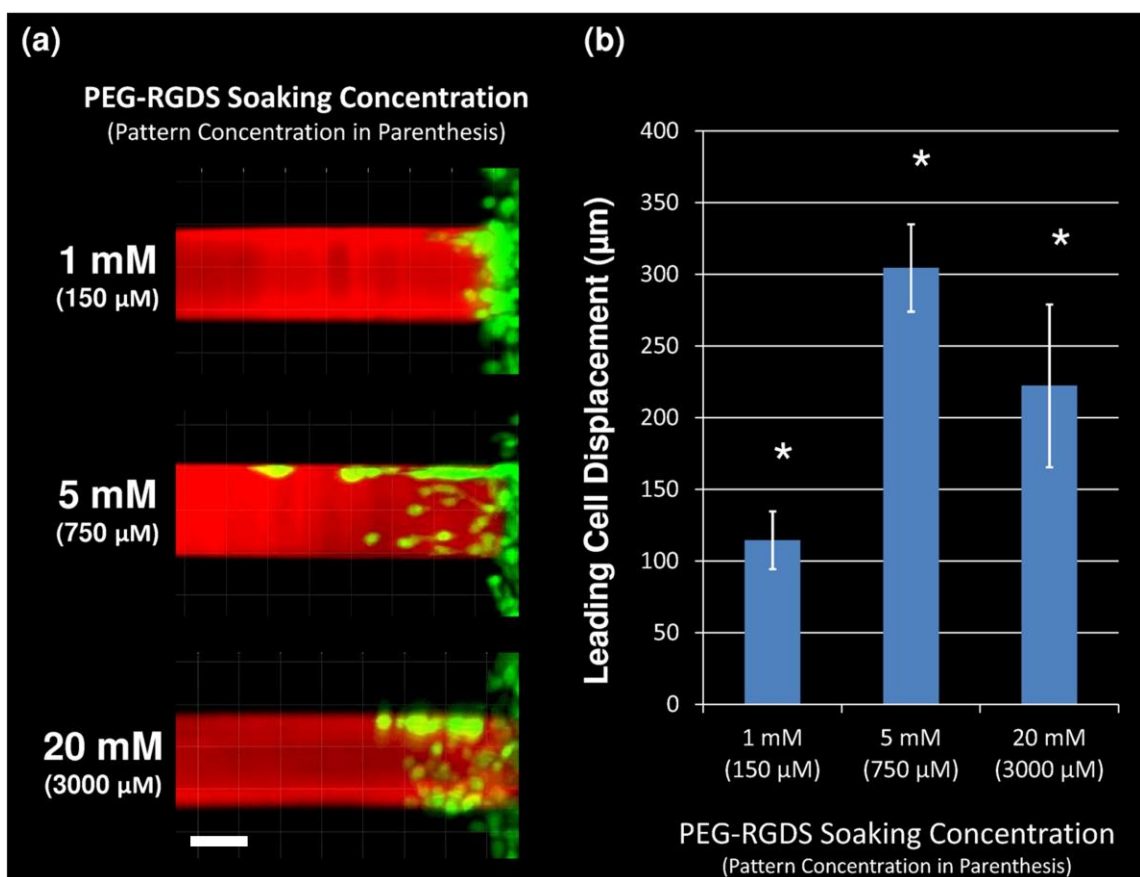


Figure 3-11: Leading Cell Displacement in 3D Micropatterns varies with PEG-RGDS Concentration. (a) After 1 day, HT1080s (green) have migrated into 3D micropatterns of PEG-RGDS (red) within PEG-PQ hydrogels. PEG-RGDS micropatterns vary in concentration. The soaking concentration of PEG-RGDS is indicated with the functional PEG-RGDS concentration of each pattern below in parenthesis. All images are representative. Scale bar = 50 μm. (b) The total displacement of the leading cell along each 3D micropattern is quantified. Leading cell displacement has a significant (* $p < 0.05$) biphasic dependence on PEG-RGDS concentration.

3.3.5 Cell Speed and Persistence within 3D Hydrogels Increase over Time

HT1080 cell migration within 3D PEG-PQ hydrogels was studied at early and late time points in order to determine the effects of the passage of time within the system. Specifically, 100 x 100 x 500 μm patterns of PEG-RGDS (functional concentration of 750 μM) were fabricated within PEG-PQ hydrogels with the pattern reaching all the way to the periphery of the hydrogel. Fluorescently labeled HT1080s were then encapsulated

within a PEG-PQ hydrogel directly adjacent to the 3D PEG-RGDS patterns. After 12 h (day 1) cells had moved into the micropattern and were taken to a confocal microscope and monitored for migration via time-lapse microscopy. HT1080s were also monitored for migration 36 h (day 2) after cell encapsulation. Representative images of HT1080s migrating through PEG-RGDS patterns at day 1 and day 2 are shown in Figure 3-12a. An increased number of cells were present at day 2 and cells had migrated all the way to the end of the 500 μm long pattern. Cells were tracked on both day 1 and day 2 with the passage of time indicated by the changing color of the tracking lines with early times indicated by blues and reds and later times indicated by yellows and whites. In both cases cell were analyzed for cell speed and cell persistence. Both cell speed and cell persistence were seen to be significantly increased on day 2 as opposed to day 1 (Figure 3-12b). Specifically, cell speed was increased from an average of 14 $\mu\text{m}/\text{h}$ on day 1 to 22 $\mu\text{m}/\text{h}$ on day 2. Cell persistence was also increased from 0.34 to 0.45, indicating that a larger percentage of cell movement contributed to overall displacement from the cell starting position.

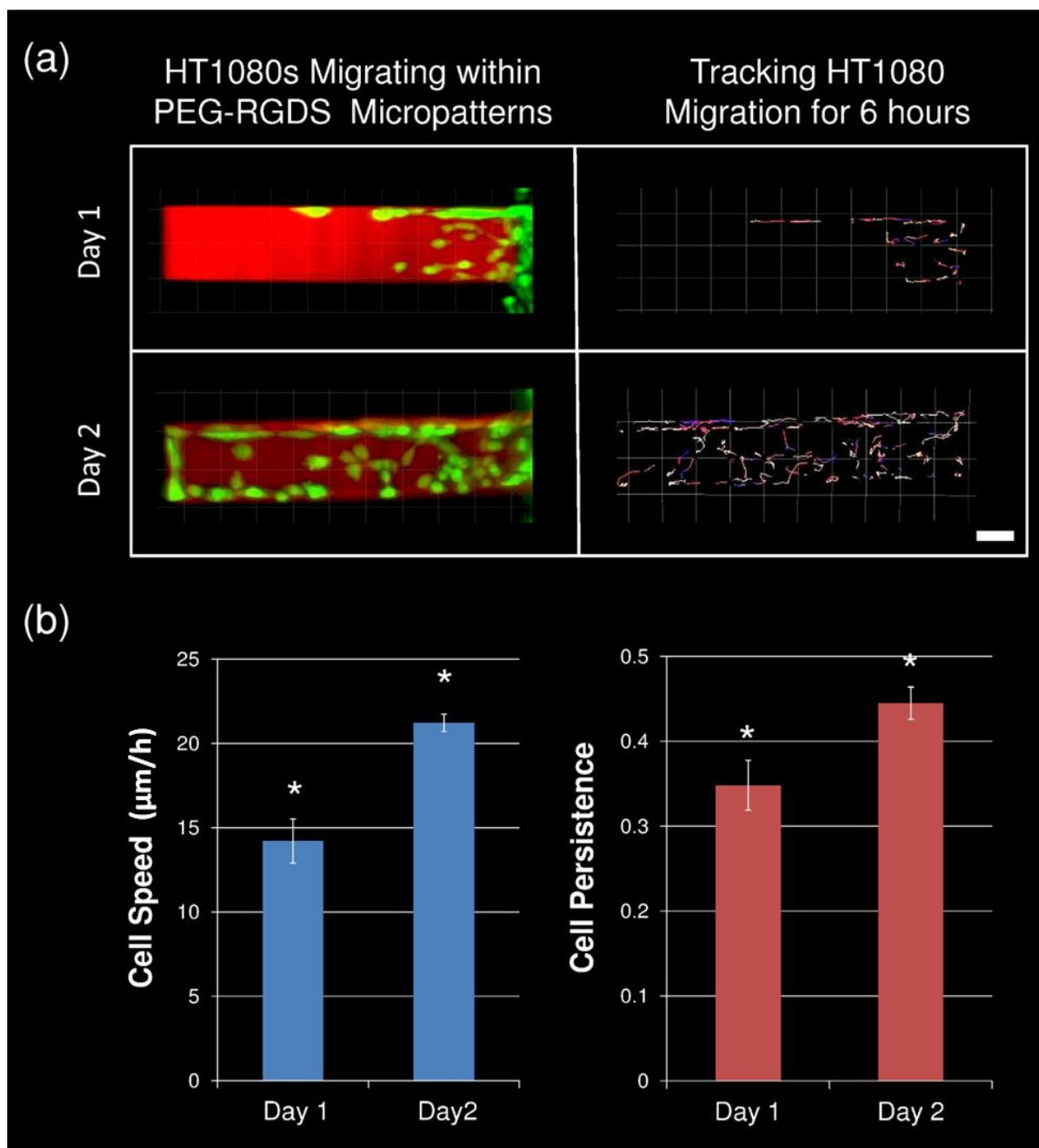


Figure 3-12: HT1080 Migration Speed and Persistence Increase Over Time. (a) HT1080s (green) are shown migrating within PEG-RGDS micropatterns (red) both 1 day and 2 days after cell seeding. HT1080 cells were then tracked for 6 h on both days, with the passage of time indicated by color changes from blue to red to yellow to white. All images are representative. Scale bar = 50 μm . (b) Cell tracking data was used to calculate cell speed and cell persistence on both day 1 and day 2. Both cell speed and cell persistence were significantly increased (* $p < 0.05$) from day 1 to day 2.

These increases might be explained by increased degradation of the PEG-PQ matrix within the PEG-RGDS patterned region, leading to increased pore size and reducing the need for cells to secrete enzymes to degrade the matrix before moving. These observations demonstrate the ever changing microenvironment of motile cells as they degrade and deposit matrix, and show the potentials of TP-LSL and PEG hydrogels as tools to monitor cell migration over time.

3.3.6 Hydrogel Composition Affects Leading Cell Displacement into Hydrogel

The PEG-based hydrogel system allows for the straightforward variation of the hydrogel composition while keeping the concentration of adhesive ligand constant. In this section, PEG-PQ hydrogels of 2 different dry weight percentages (5% and 10%) were micropatterned with PEG-RGDS channels and 3D cell migration was again accessed via time-lapse confocal microscopy. The PEG-RGDS micropatterns used were 100 x 100 x 500 μm in dimensions and the functional concentration of PEG-RGDS was 750 μM . Representative images of HT1080 migration into the patterned hydrogels 12 h after cell encapsulation are shown in Figure 3-13a. Very few cells were observed to migrate into the 10% PEG-PQ hydrogels (elastic modulus of 42 kPa¹³⁴) while migration into the 5% PEG-PQ hydrogels (elastic modulus of 21.5kPa¹³⁴) was robust. Due to a lack of cells migrating in 10% hydrogels, cell speed and persistence were not quantified. Rather, to quantify differences in cell migration, the total displacement of the leading cell into the PEG-RGDS pattern for each of the hydrogel was measured. Leading cell displacement was approximately 12 times greater for 5% PEG-PQ hydrogels as compared to 10% PEG-PQ hydrogels (300 μm vs. 25 μm) (Figure 3-13b).

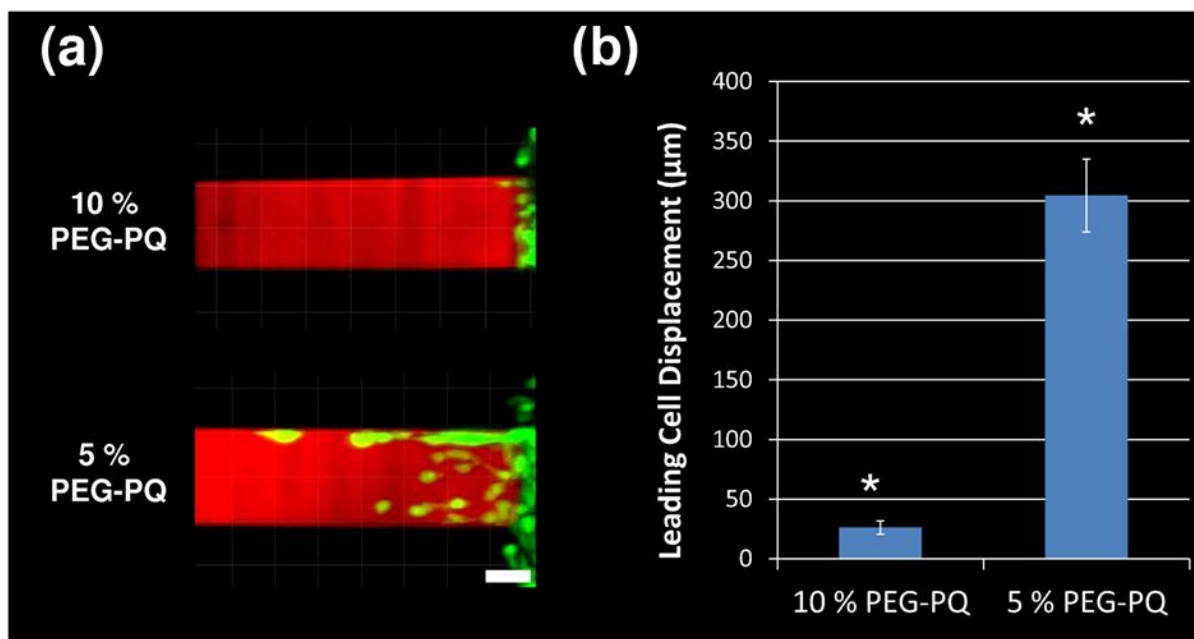


Figure 3-13: Leading Cell Displacement in 3D Micropatterns Varies with PEG-PQ Hydrogel Composition. (a) After 1 day, HT1080s (green) have migrated into 3D micropatterns of PEG-RGDS (red) within PEG-PQ hydrogels. The weight percent of PEG-PQ hydrogels was varied. All images are representative. Scale bar = 50 μm . (b) The total displacement of the leading cell along each 3D micropattern is quantified. Leading cell displacement is significantly ($*p < 0.05$) greater in 5 % PEG-PQ hydrogels as compared to 10% PEG-PQ hydrogels.

This invasion difference may be attributed to the increased number of PEG-PQ chains that must be degraded for cells to migrate within 10% PEG-PQ hydrogels as opposed to 5% PEG-PQ hydrogels. Increased mechanical stiffness of the 10% hydrogel (elastic modulus of 42 kPa¹³⁴) compared to those of 5% hydrogels (elastic modulus of 21.5 kPa¹³⁴) could also play a role in the decreased invasion of HT1080s. This experiment demonstrates that hydrogel composition can be varied independently of cell adhesion molecule concentration. Further, dramatic differences in cell migration based on

the weight percent of the hydrogel are shown, which should lead the way for future studies to investigate the precise role of mechanical stiffness and proteolytic susceptibility on cell migration within micropatterned biomaterials.

3.4 Discussion

New technologies to investigate complex biological phenomena have become increasingly important across the bioengineering discipline. More specifically, a detailed understanding of cell motility will be critical to both the advancement of tissue engineering as well as the discovery of new therapeutic strategies to combat disease¹²⁴. In this chapter, TP-LSL has been applied to systematically study cell migration in 2 and 3 dimensions through the micropatterning of PEG-based hydrogels. Specifically, PEG-RGDS was patterned onto the surface of PEG-DA hydrogels to study 2D migration and within the interior of enzymatically degradable PEG-PQ hydrogels to study 3D migration.

A ninhydrin-based assay was utilized to determine that TP-LSL has a conjugation efficiency of 15%, which allowed for the approximation of the functional PEG-RGDS concentration in all micropatterned hydrogels. While the assay was performed in PEG-DA hydrogels, the photochemical crosslinking mechanism of PEG-RGDS is identical in PEG-PQ hydrogels, and thus a similar crosslinking efficiency would be expected. HT1080s were observed to migrate at faster speeds and with lower persistence on 2D PEG-DA hydrogel surfaces when compared to 3D migration within PEG-PQ hydrogels. Further, cells migrating in 3D were smaller and more elongated than those in 2D. These observations are likely due to the steric hindrances placed on cells migrating within a 3D matrix. In 2D, cells are free to spread out and move around on a flat surface without

having to degrade a matrix and then navigate over and around 3D obstacles. Without these hindrances, cells in 2D move faster and reverse direction more rapidly, leading to decreased persistence. Cells migrating in 3D however must secrete enzymes to degrade the hydrogel before they can migrate. Even after local matrix degradation, cells must deform through irregular 3D pathways, leading to a slower speed, a more elongated shape, and more difficulty reversing direction.

The use of TP-LSL in combination with PEG-based hydrogels to investigate difference between 2D and 3D cell migration offered several advantages over traditional approaches. In traditional studies comparing 2D and 3D cell migration, confounding factors make it difficult to draw direct conclusions or trends. For example, when comparing 2D tissue culture plastic to 3D naturally derived matrix, cells experience differences in substrate stiffness, pore size, proteolytic susceptibility, adhesive ligand concentration, and biochemical growth factors¹²⁴. With all of these variables, it is difficult to parse out the cause of observed differences in cell migration. In the PEG-based hydrogel system presented in this chapter, identical concentrations of PEG-RGDS are presented in both 2D and 3D. Additionally, the non-adhesive nature of PEG ensures that no other biochemical factors influence the results. Finally, the 5% PEG-DA (6000 Da) and 5% PEG-PQ (~7800 Da) hydrogels used in this study have similar mechanical properties^{134,135} (elastic modulus ~ 20-25 kPa) and pore sizes (on the order of nanometers). Therefore, the only true differences between 2D and 3D cell migration in this study are the effects of the biomaterial matrix on all sides of the cells (3D) rather than only below them (2D). The TP-LSL system also has the advantage of increasingly precise guidance of cells in both 2D and 3D. The dimensions of PEG-RGDS patterns

were narrowed from 100 μm to 10 μm so that cell persistence and cell migration ratio were increased and the cell direction was precisely guided. This ability to precisely guide cells in 3D will be important for a variety of purposes as research continues. For example, the ability to dictate exactly where cells migrate will be critical for testing how cells respond in controlled biomaterial microenvironments such as engineered cancer models or biomaterial tissue constructs.

This chapter also investigated the effects of varying the concentration of PEG-RGDS on both 2D and 3D cell migration. On patterned 2D hydrogel surfaces, cell speed was seen to have a biphasic dependence on PEG-RGDS concentration. These results have been well documented on a variety of surfaces^{127,129}, and are a result of the balance of forces between leading cell edge attachment and the trailing cell edge detachment during cell migration. Cell persistence on 2D surfaces was not strongly correlated with PEG-RGDS concentration, a result also in agreement with previous studies^{124,136}.

For cells migrating within enzymatically degradable PEG-PQ hydrogels, PEG-RGDS concentration was not seen to significantly affect cell speed or persistence. This result initially appears to be in conflict with previous studies that have reported a biphasic dependence of adhesive ligand concentration on cell speed and persistence for cells migrating in 3D^{69,137}. However, in the studies reported in this chapter, PEG-RGDS concentration had biphasic effect on the displacement of the leading cell migrating into the PEG-RGDS micropatterns, with the maximum cell displacement occurring at intermediate PEG-RGDS concentrations. Functionally, this means that leading HT1080 cells follow the reported biphasic model^{69,137} as they are better able to degrade and move through the PEG-PQ hydrogel when ligated by an intermediate concentration of adhesive

ligand. HT1080s that migrate into the hydrogel after the leading cells were observed to follow behind leading cells where the matrix has already been degraded. These cells may migrate via a different mechanism in which cell speed is not dependent on PEG-RGDS concentration. In fact, HT1080s have previously been reported to possess the ability to migrate via an amoeboid-like mechanism that was only weakly dependent on cell adhesion¹³². Future studies will investigate migration modes in further detail via an examination of focal adhesion structure under various micropatterned conditions.

3D cell migration was also investigated both 1 day and 2 days after initial encapsulation of cells. Cells migrating within micropatterns of a fixed level of PEG-RGDS demonstrated increases in cell speed and cell persistence on day 2 as opposed to day 1. This result could be explained by the increased degradation of the hydrogel within the PEG-RGDS pattern as cells continue to invade and migrate over an additional 24 h. This degradation would lead to increased pore size and reduce the need for cells to secrete enzymes to disperse the matrix before moving. This result is in agreement with previous work that has demonstrated increased MMP activity increases cell persistence in 3D collagen matrices¹³⁸.

Finally, the displacement of leading cells was investigated in PEG-PQ hydrogels of different percent weights. Cell displacement into the PEG-RGDS micropattern was shown to be significantly increased in 5% PEG-PQ hydrogels as opposed to 10% hydrogels after 12 h. This effect may be due to the increased number of PEG chains that must be degraded within higher percentage PEG-PQ hydrogels before cells are able to move. However, the increased mechanical stiffness of a 10% hydrogel compared to a 5% hydrogel also plays a role in decreased cell displacement as high substrate stiffness has

previously been shown to decrease cell speed in 3D⁶⁹. Previous work by Lee *et al.* has developed an enzymatically degradable PEG-based hydrogel with a fluorogenic substrate that allows for real-time, fluorescence-based monitoring of hydrogel degradation⁵⁷. Future studies will use these hydrogels in combination with PEG-RGDS patterns to investigate exactly how the matrix is degraded when cells invade, and thus help to define the roles of matrix degradation versus matrix stiffness. Additionally, matrix stiffness and matrix degradation will be further decoupled by investigating cell migration within non-degradable PEG-DA hydrogels with microscopic pores¹³¹ so that material stiffness may be tested without the effects of proteolysis.

This chapter has, for the first time, utilized TP-LSL and PEG-based hydrogels to conduct a quantitative study of cell migration. While this work stands as an important step towards more controlled studies of cell motility *in vitro*, a number of exciting future studies will reveal even more about how cells move within increasingly complex biomaterial microenvironments. Further work is necessary in order to completely elucidate the effects of cell adhesion, material stiffness, pore size, proteolytic degradation, and bioactive growth factors on cell motility. The effect of bioactive growth factors in particular was not tested in this chapter. Numerous peptides and proteins with various functionalities have already been incorporated into PEG-based hydrogels^{47,48,134,139,140}, and future studies will use TP-LSL to pattern these molecules to probe their effect on cell migration. New experiments will also explore the effects of complex geometries of adhesive ligands on cell migration. For example, islands of PEG-RGDS of various size, shape and spacing will be micropatterned in both 2D and 3D in order to probe how cells migrate when presented with gaps in adhesive ligand.

Additionally, while HT1080s were utilized in this chapter, it will be important to test the migratory properties of different cell types. In fact, determining key differences in cell migration between various cell types will be critical for both organizing cells into complex tissues as well as investigating a number of diseases caused by aberrant cell motility.

3.5 Conclusion

The movement of cells within the human body is critical to a number of physiologic processes and a central component of life itself. A strong understanding of the mechanisms and environmental factors that contribute to cell migration is important for a variety of purposes from understanding and treating disease to designing and developing engineered tissue therapeutics. In this work, TP-LSL and PEG-based hydrogels have been utilized to guide cell migration under controlled conditions in order to quantitatively study cell motility. PEG-RGDS channels were micropatterned within PEG-DA and PEG-PQ hydrogels and the migration of HT1080 cells were tracked in both 2 and 3 dimensions. HT1080s were shown to migrate faster and with lower persistence on 2D surfaces, while cells migrating in 3D were smaller and more elongated. Further, cell migration was shown to have a biphasic dependence on PEG-RGDS concentration and cells moving within PEG-RGDS micropatterns were seen to move faster and with more persistence over time. Finally, markedly less cell displacement into PEG-RGDS micropatterns was seen for PEG-PQ hydrogels with higher weight percents. These results begin to parse out many of the traditional confounding factors that affect cell migration and establish TP-LSL as a strong tool to probe cell behavior within 3D engineered biomaterials. This thesis will now build on the established ability to guide cell behavior

in vitro through the implementation of TP-LSL to guide biomimetic cellular organization for microvascular tissue engineering applications.

Chapter 4: Three-Dimensional Biomimetic Patterning in

Hydrogels to Guide Cellular Organization

A significant portion of this chapter was previously published in:

J.C. Culver*, **J.C. Hoffmann***, R.A. Poche', J.H. Slater, J.L. West, and M.E. Dickinson. 2012. Three-Dimensional Biomimetic Patterning in Hydrogels to Guide Cellular Organization. *Advanced Materials* 24: 2344-48.

*These authors contributed equally to this work.

4.1 Introduction

Within the human body, intricate networks of microvessels allow for the exchange of gases, nutrients and wastes that ultimately keeps tissues and organs viable and functional. The development of a similar artificial microvascular network within biomaterial scaffolds will be necessary to engineer complex, biomimetic tissues for use as a therapeutic solution for diseased patients. As discussed in Chapter 1, a variety of biomaterial approaches have been utilized to develop an environment favorable for the assembly of a complex microvasculature. Enzymatically degradable, acrylate-based PEG hydrogels, known as PEG-PQ hydrogels, have been particularly successful in engineering vessel tubules on the microscale. For example, human umbilical vein endothelial cells (HUVECs) and mesenchymal progenitor 10T1/2 cells were photo-encapsulated within PEG-PQ hydrogels with acrylate-PEG-RGDS²⁸. In a process reminiscent of vasculogenesis, the HUVECs were then seen to form complex networks of lumenized tubes (Figure 4-1a) that were physically supported by long, wrapping 10T1/2 cells²⁸. The 10T1/2 cells upregulated smooth muscle α -actin, indicating differentiation towards a pericyte-like phenotype (Figure 4-1b)²⁸. These complex vessel networks were also shown

to be supported by a layer of collagen IV and laminin²⁸, which are typical extracellular matrix molecules present on the basement membrane of capillaries. These engineered vessel networks have even shown the ability to support the flow of media containing fluorescent dextran molecules within a microfluidic system, thus indicating their promise for use as a microvascular system to support the exchange of gases, nutrients, and wastes within engineered tissues¹⁴¹.

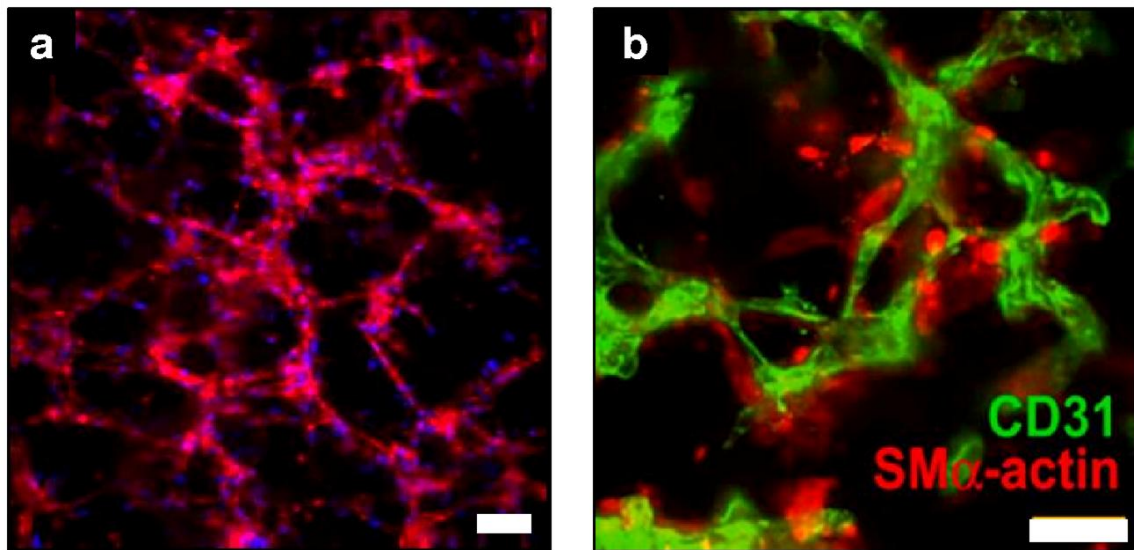


Figure 4-1: Tubule Networks in PEG-Based Hydrogels. HUVECS and 10T1/2s encapsulated within a PEG-PQ hydrogel have assembled into stable tubule networks. a) DAPI (blue) and phalloidin (red) staining highlight the nuclei and f-actin organization of cellular tubule networks within a PEG-PQ hydrogel after 28 days in culture. b) Staining for CD31 (green) and smooth muscle α -actin (red) highlight the endothelial cell tubules that are supported by the smooth muscle α -actin of 10T1/2 cells within a PEG-PQ hydrogel. Scale bars = 50 μ m. Adapted from Moon *et al.*²⁸

While promising, engineered microvessels within PEG-PQ hydrogels have thus far failed to physically resemble the microvasculature from endogenous tissues. Specifically, HUVECs and 10T1/2s within PEG-PQ hydrogels have been observed to form random and somewhat disorganized microvascular networks. Contrastingly, the

orientation of microvessels within the body is highly organized and tissue specific, with a myriad of unique microvascular structures precisely designed to meet the functional demands of each endogenous tissue. Within the body, each tissue has a microvasculature with a unique vessel density and vessel orientation, with the vessel density precisely regulating oxygenation and nutrient delivery requirements, and the vessel orientation often directly contributing to specific tissue functions⁹. For example, the capillaries within the lung, liver, spleen and kidney assemble into unique function-based orientations that are considerably denser than needed to meet gas and nutrient exchange requirements⁹.

Since precisely organized vascular structures are a vital component of endogenous tissues, it follows that in order to develop functional engineered tissue constructs, it will be necessary to not only form an intricate network of microvessels, but also to spatially guide the formation of those engineered microvessels to mimic specific endogenous structures. Toward this end, this chapter develops a process that utilizes confocal images from tissues to guide two-photon laser scanning lithography (TP-LSL) in order to generate highly complex, three-dimensional, and biologically relevant micropatterned materials.

For many specialized tissues, there is now a wealth of information describing 3D architecture in structural and molecular detail, at times even in the form of quantitative maps defined using high-resolution microscopy and sophisticated image processing techniques¹⁴²⁻¹⁴⁵. These images are highly detailed blueprints that may be used to construct advanced scaffold materials to precisely mimic specialized tissue features. However, despite the sophisticated techniques available to define these complex

blueprints, similarly sophisticated techniques to fabricate 3D scaffolds with a matching level of structural complexity at micron-scale resolution have yet to be developed. This chapter reports a novel technique to accomplish this task using image-guided TP-LSL patterning in order to create truly biomimetic scaffolds that closely model endogenous microenvironments, such as the microvasculature. This process was applied iteratively for immobilization of multiple moieties within a single scaffold. Further, when vascular cells were homogeneously seeded in a hydrogel material with immobilized cell adhesion peptides presented in a pattern derived from images of a tissue microvascular network, the cells rapidly (<24 h) organized into a network matching the original tissue image with good fidelity, thus leading the way for the development of biomimetic microvascular networks critical for the success of engineered functional tissues.

4.2 Materials and Methods

4.2.1 Mice

6-8 week old CD-1 outbred mice (Charles River) were used as a source for all tissues. All animal protocols were approved by the Institutional Animal Care and Use Committee (IACUC) at Baylor College of Medicine.

4.2.2 Retinal Imaging

Mice were anesthetized with 500 mg/kg avertin and injected intracardially with lysine-fixable, tetramethylrhodamine labeled 70 kDa dextran (Invitrogen). Injections were followed by eye enucleation and fixation in 4 % paraformaldehyde overnight at 4 °C. Subsequently, the eyes were washed in 1X PBS and the retinæ were removed from the eye cups and cut into four quadrants with a #10 scalpel. This allowed for flat

mounting of the intact retinal sheet under a glass coverslip using Fluoromount-G (Southern Biotech). Vessels in the tissue were imaged using a Zeiss LSM 510 META confocal microscope and a Plan-Apochromat 20x/0.75 NA objective lens.

4.2.3 Cerebral Cortex Imaging

Mice were anesthetized with 500 mg/kg avertin and injected intracardially with lysine-fixable, tetramethylrhodamine labeled 70 kDa dextran (Invitrogen). After 3 minutes, mice were sacrificed by decapitation, and the heads were fixed whole in 4 % paraformaldehyde overnight at 4 °C. Brains were then carefully dissected from the skull, and sliced into coronal sections using a vibratome (Leica) at a thickness of 100 µm. Tissue sections were mounted flat under a glass coverslip using Fluoromount-G (Southern Biotech). Vessels in the tissue were imaged using a Zeiss LSM 710 Duoscan confocal microscope and an Achromplan 20x/0.45 NA objective lens.

4.2.4 Heart Imaging

Mice were anesthetized with 500 mg/kg avertin and injected intracardially with a 1:1 mixture of lysine-fixable, tetramethylrhodamine labeled 70 kDa dextran (Invitrogen) and an anticoagulant solution containing 3.0 mg/ml ethylenediaminetetraacetate (IBI Scientific) and 0.5 mg/ml heparin sodium salt (Sigma) in PBS. After 3 minutes, each mouse was sacrificed by decapitation, and their hearts were excised from the chest before being fixed whole in 4 % paraformaldehyde overnight at 4 °C. Hearts were then sliced into longitudinal sections using a vibratome (Leica) at a thickness of 100 µm. Tissue sections were mounted flat under a glass coverslip using Fluoromount-G (Southern Biotech). Vessels in the tissue were imaged using a Zeiss LSM 510 META confocal microscope and a Plan-Apochromat 63x/1.4 NA Oil objective lens.

4.2.5 Subependymal Zone Imaging

Mice were sacrificed and the subependymal zone (SEZ) was dissected from fresh brain tissue¹⁴. The SEZ was then fixed for 20 min at room temperature in 4 % paraformaldehyde before being subjected to standard immunostaining protocols. Tissue was washed 3 x 10 min in PBS at room temperature, then blocked and permeabilized for 1 h at room temperature in PBS/0.1 % Triton X-100 (Promega) containing 2 % donkey serum (Sigma). Next, tissue was rocked overnight at 4 °C while being incubated with the following primary antibodies in PBS with 0.1 % Triton X-100 and 2 % donkey serum: Rabbit anti-human Ki67 [1:100] (Abcam – Cat #ab16667), and Rat anti-mouse CD31 [1:100] (BD-Pharmingen – Cat #550274). The next day, the tissue was washed 3 x 10 min in PBS with 0.1 % Triton X-100 at room temperature, and then incubated for 1.5 h at room temperature with DAPI [1:500] (Invitrogen) and the following secondary antibodies in PBS with 0.1 % Triton X-100 and 2 % donkey serum: Donkey anti-Rabbit IgG Alexa-568 [1:500] (Invitrogen – Cat #A10042) and Donkey anti-Rat IgG Alexa-488 [1:500] (Invitrogen – Cat#A11006). Finally, tissue was washed 3 x 10 min in PBS/0.1 % Triton X-100 at room temperature before being mounted flat on glass slides using Fluoromount-G (Southern Biotech). Samples were allowed to set, and then imaged using a Zeiss LSM 510 META confocal microscope and a Plan-Apochromat 20x/0.75 NA objective lens.

4.2.6 Synthesis and Fluorescent Labeling of PEG-IKVAV

Acrylate-PEG-IKVAV has been synthesized previously¹⁴⁶. Briefly, the IKVAV peptide (derived from laminin) was synthesized using solid phase peptide synthesis with an Apex396 peptide synthesizer (Aapptec) and characterized using MALDI-ToF. Fmoc-Lys(ivDde)-OH (NovaBiochem) was used as the protected lysine residue during the

synthesis and the ivDde protecting group was left on the lysine amine after peptide cleavage from the resin. The IKVAV peptide was reacted with PEG-SCM and DIPEA in DMSO and purified and characterized in the same manner as RGDS (Section 2.2.2). The protecting group was then cleaved via 3 x 10 min mixing steps with 2 % hydrazine in DMF, before undergoing dialysis (3500 MWCO regenerated cellulose membrane, Spectrum Laboratories) and lyophilization. Acrylate-PEG-IKVAV in 0.1 M sodium bicarbonate (pH 8.3) was reacted with Alexa Fluor® 633 carboxylic acid succinimidyl ester (633-SE; Invitrogen) in DMF at a 1:4 molar ratio (acrylate-PEG-RGDS:633-SE). After 2 h of rapid mixing, the product, acrylate-PEG-IKVAV-Alexa Fluor®633 (abbreviated PEG-IKVAV-633) was once again dialyzed and lyophilized and stored at -20 °C until needed for use.

4.2.7 Fabrication of PEG-PQ Hydrogel

Methacrylate-modified coverglass was obtained as described in Section 2.2.4. A separate supply of glass was then treated in Sigmacoat® (Sigma) to generate a hydrophobic surface. Molds were fabricated by securing a poly(tetra fluoroethylene) spacer (approximately 125 µm in thickness) between an acrylated piece of coverglass and water repellent piece of coverglass (Figure 4-2a). PEG-PQ was synthesized and purified as described in section 2.2.2. A solution of 10% (w/v) PEG-PQ in HBS with 10 µl/ml of 300 mg/ml 2, 2-dimethoxy-2-phenylacetophenone (DMAP) in *N*-vinyl pyrrolidone (NVP) was then prepared and injected into the mold (Figure 4-2b). The solution was exposed to long wavelength ultraviolet light (B-200SP UV lamp, UVP, 365 nm, 10 mW/cm²) for 45 sec (Figure 4-2c). After removal from the mold, a crosslinked

and immobilized hydrogel was formed on the methacrylate-modified glass coverslip (Figure 4-2d). Immobilized hydrogels were soaked in filtered HBS until further use.

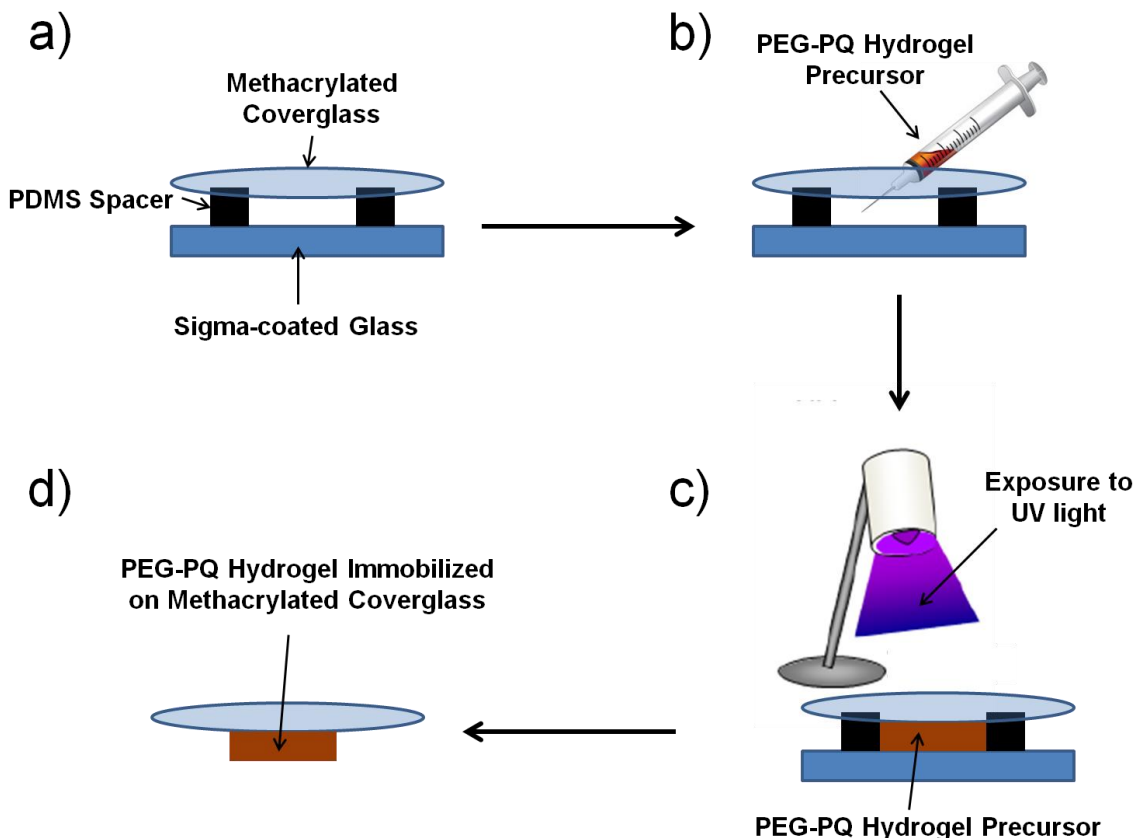


Figure 4-2: Fabrication Methodology for Immobilized PEG-PQ Hydrogels. (a) A mold consisting of a glass slide previously incubated in Sigmacoat, PDMS spacers, and a methacrylate-modified coverslip was formed. (b) PEG-PQ hydrogel precursor solution was injected into the mold. (c) The precursor solution inside the mold was exposed to UV light for 45 s. (d) The mold was removed and a PEG-PQ hydrogel immobilized on a methacrylate-modified coverslip was formed.

4.2.8 Mosaic Reconstruction of Imaged Structures Using LSM ROIs

Custom-written scripts were developed using MATLAB (MathWorks) to spatially control the scanning laser of a Zeiss LSM 510 or Zeiss LSM 710 Multiphoton microscope so that it traces out the shape of labeled features of endogenous tissues, such as labeled microvasculature. The source code for these scripts is included in the appendix. One subroutine utilized by this software package is a modification of a published segmentation algorithm¹⁴⁸.

The software achieves mosaic reconstruction in a stepwise fashion (see Figure 4-4). Briefly, the software starts with a z-stack of cross sectional images of labeled tissue, and for each cross section it converts the 8-bit image into a binary image using pre-processing techniques. The software then divides the vessel structure in each of these images into shapes that have a user-defined width. Next, each of these shapes are approximated with quadrilaterals and used to define ROIs. Finally, the software creates one overlay file for each cross section; these overlay files are formatted so that they can be interpreted within the Zeiss ZEN or AIM software as a list of ROIs. On the Zeiss LSM 710 Multiphoton microscope, we also needed to use custom-written ZEN macros to classify these as type “Acquisition” ROIs so that they could be used to spatially define where the laser scanned through each sample.

4.2.9 Image-Guided TP-LSL Patterning Methodology

The synthesis of PEG-RGDS-488 was described in detail in section 2.2.2. Fabricated PEG-PQ hydrogels immobilized on glass coverslips were incubated in 50-100 nmol/ml of PEG-RGDS-488 in HBS with 10 μ l/ml of 300 mg/ml DMAP in NVP for 30 min. The hydrogel was then placed on the stage of a Zeiss LSM 510 or Zeiss LSM 710

Multiphoton microscope outfitted with a Plan-Apochromat 20x/0.75 NA objective lens or a W Plan-Apochromat 20x/1.0 NA DIC VIS-IR objective lens, and the stage was adjusted to bring the bottom of the hydrogel into focus. In order to pattern a single vessel image throughout the gel, the generated region of interest was selected, and for the Zeiss LSM 510, the titanium/sapphire laser was tuned to 720 nm with a 25 mW/ μm^2 laser intensity and a 102 $\mu\text{sec}/\text{pixel}$ laser scan speed. Alternatively, for the Zeiss LSM 710, a laser intensity of 60 mW/ μm^2 and a laser scan speed of 25 $\mu\text{sec}/\text{pixel}$ was utilized. The two-photon laser then excited photoinitiator molecules in precise locations designated by the overlay file, resulting in the crosslinking of free acrylate groups on PEG-RGDS-488 to free acrylate groups in the PEG-PQ hydrogel. After the scanning of a single 2D slice, the focus of the microscope was repeatedly adjusted 3-6 μm axially and scanned again to confer the desired depth to the pattern. After scanning was completed, the hydrogel was washed in HBS under gentle rocking for 48 h with at least 4 buffer changes to remove unbound PEG-RGDS-488. In order to pattern a 3D vessel bed, a new generated region of interest was selected for each successive scan as the focus was adjusted axially through the z-axis. In all cases, the distance of the focal adjustment corresponded exactly with the distance between the vessel image slices from which the regions of interest were derived. Patterns were visualized after washing using a confocal microscope (Zeiss5 LIVE, Plan-Apochromat 20x objective with 0.8 numerical aperture: for Alexafluor 488 excitation = 489 nm, emission BP filter = 500–525 nm), and z-stacks were analyzed using AIM Image Examiner (Carl Zeiss), ImageJ (NIH Bethesda, MD), and Imaris (Bitplane).

4.2.10 Patterning the Endogenous SEZ Microenvironment with Multiple Peptides

PEG-PQ hydrogels were permeated with PEG-RGDS-488 and DMAP in NVP as in Section 4.2.9. The generated overlay file from PECAM-1 immunostaining of the murine subependymal zone vessels was then selected and a pattern was fabricated using the titanium/sapphire laser tuned to 720 nm as described previously. Unbound PEG-RGDS-488 was washed away overnight and hydrogels were permeated with 50-100 nmol/ml of PEG-IKVAV-633 in HBS with 10 μ l/ml of 300 mg/ml DMAP in NVP for 30 min. The hydrogels were then imaged using a 488 nm laser and aligned precisely on the multiphoton microscope so that the vessel pattern coincided exactly with the PECAM-1 staining region of interest on the computer screen. The generated overlay file from the Ki67 immunostaining of the murine subependymal zone neural progenitors was then selected, and a pattern was fabricated using the titanium/sapphire laser tuned to 720 nm as described previously. Both juxtaposed patterned biomolecules within the PEG-PQ hydrogels were next washed overnight and imaged simultaneously using a confocal microscope (Zeiss5 LIVE, Plan-Apochromat 20x objective with 0.8 numerical aperture: for Alexafluor 488 excitation = 489 nm, emission BP filter = 500–525 nm; for Alexafluor 633 excitation = 633 nm, emission long pass filter = 650 nm).

4.2.11 Cell Maintenance

Human umbilical vein endothelial cells (HUVECs, Lonza) were maintained in culture with endothelial cell growth medium 2 (EGM-2, Lonza) supplemented with 2 % fetal bovine serum, GA-1000 (gentamicin and amphotericin-B), ascorbic acid, epidermal growth factor, fibroblast growth factor, heparin, hydrocortisone, insulin-like growth factor, vascular endothelial growth factor, (Bulletkit, Lonza), 2 mM L-glutamine, 1 U/ml

penicillin, and 1 $\mu\text{g}/\text{ml}$ streptomycin (GPS, Sigma). 10T1/2 cells (American Type Culture Collection) were grown and maintained in Dulbecco's modified Eagle's medium (DMEM, Gibco) with supplements of 10 % fetal bovine serum and GPS. HUVECs were used through passage 6 and 10T1/2s were used through passage 18. Cells were maintained at 37° C with 5 % CO₂ and the medium was replenished every 2 days.

4.2.12 Encapsulation of HUVECs and 10T1/2s into Hydrogels

Cells were fluorescently labeled prior to encapsulation via a 1 h incubation with 1 $\mu\text{g}/\text{ml}$ red CMFDA Cell Tracker®(Invitrogen) in EGM-2 (for HUVECs) or with 1 $\mu\text{g}/\text{ml}$ green CMFDA Cell Tracker® (Invitrogen) in DMEM (for 10T1/2s). After incubation, cells were washed with PBS and fresh media was added. A hydrogel precursor solution of 7.5 % PEG-PQ with 3.4 $\mu\text{l}/\text{ml}$ NVP, 1.5 % v/v triethanolamine (Fluka BioChemika) and 10 μM eosin Y (Sigma) was made in HBS. Fluorescently labeled HUVECs and 10T1/2s were then harvested and suspended in the precursor solution at a 4:1 ratio with a final cell density of 30,000 cells/ μl . Hydrogel molds were fabricated using 280 μm thick spacers inserted between a glass slide exposed to Sigmcoat® and a methacrylated coverslip. 4 μl of the precursor solution was injected into the mold and exposed to white light (Fiberlite, Dolan Jenner) for 25 s, yielding a crosslinked and immobilized cellularized hydrogel (Figure 4-3a). Hydrogels were immediately immersed in EGM-2 media for 1 h before patterning.

4.2.13 Patterning Cellularized Hydrogels

Cellularized hydrogels were incubated in a solution of 5 $\mu\text{mol}/\text{ml}$ PEG-RGDS and 85 nmol/ml PEG-RGDS-633 in HBS with 10 $\mu\text{l}/\text{ml}$ of 300 mg/ml DMAP in NVP for 15 min. The hydrogel was then placed on the stage of a Zeiss LSM 710 Multiphoton

microscope and patterned as described previously. A heating chamber was utilized to maintain a 37 °C environment during patterning. A single cortex microvasculature ROI was chosen and the laser was scanned sequentially as the focus was repeatedly adjusted 3 μm axially until a total pattern depth of 150 μm was reached (Figure 4-3b). The hydrogel was then immersed in EMB-2 media with 3 media changes in the first 24 h to wash out unbound PEG-RGDS (Figure 4-3c). HUVECs and 10T1/2s were then given time to form tubules that aligned with the PEG-RGDS patterns (Figure 4-3d). Cell migration and organization was monitored using a confocal microscope (Zeiss5 LIVE, Plan-Apochromat 20x objective with 0.8 numerical aperture: for green CMFDA Cell Tracker excitation = 489 nm, emission BP filter = 500–525 nm; for red CMFDA Cell Tracker excitation = 532 nm, emission BP filter = 560-676 nm; for Alexafluor 633 excitation = 633 nm, emission long pass filter = 650 nm).

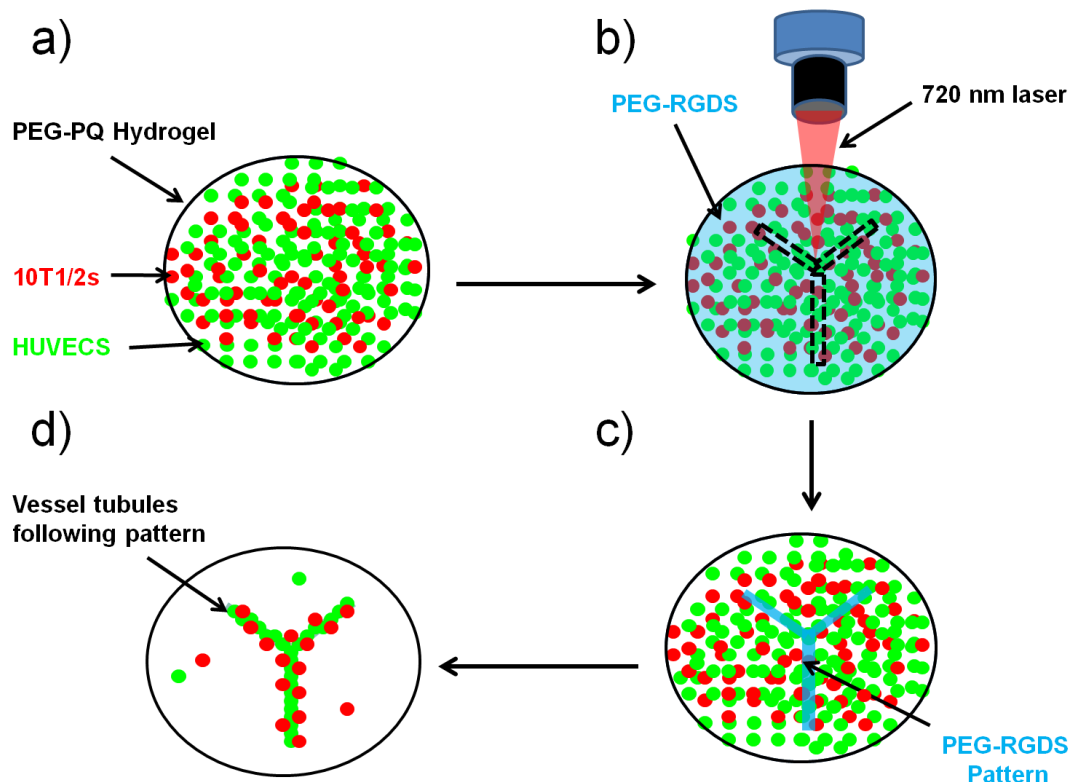


Figure 4-3: Methodology for Patterning Cellularized Hydrogels to Guide Tubule Formation. a) HUVECS (green) and 10T1/2s (red) are photo-encapsulated within a PEG-PQ hydrogel. b) The cell-laden hydrogel is permeated with PEG-RGDS (blue) and TP-LSL is used to crosslink PEG-RGDS into a biomimetic pattern. c) The non-bound PEG-RGDS is washed away, leaving a PEG-RGDS micropattern. d) Over time, the HUVECS and 10T1/2s assemble into vessels that align with the PEG-RGDS micropattern.

4.2.14 Immunohistochemistry on Cellularized Hydrogels

To examine apoptotic activity and tubule structure in guided cellularized hydrogels, immunohistochemical staining for nuclei, f-actin, and caspase 3 was performed. After 2 days in culture, the gels were incubated in 4% paraformaldehyde for 20 min and then washed with PBS. The gels were exposed to 0.5% Triton X-100 for 30 min to permeabilize the cells, and washed again with PBS. To block non-specific binding, the gels were incubated in 3% normal donkey serum (Sigma) in PBS for 1 h.

The gels were next incubated in rabbit anti-caspase 3 (Abcam) at a 1:200 dilution in PBS with 3% bovine serum albumin (BSA) for 12 h at 4°C. After incubation, the gels were washed in PBS 5 times with a buffer change every 60 min. To visualize the primary antibody, the gels were incubated in a 1:400 dilution of Alexafluor 488 donkey anti-rabbit IgG (Invitrogen) in PBS with 3% BSA for 12 h at 4°C. Gels were again washed for 5 h with PBS with a buffer change every 60 min. Finally gels were incubated in 2 μ M DAPI with 1:100 rhodamine phalloidin (Invitrogen) in PBS for 12 h, and visualized on a confocal microscope (Zeiss5 LIVE, Plan-Apochromat 20x objective with 0.8 numerical aperture: for Alexafluor 488 excitation = 489 nm, emission BP filter = 500–525 nm; for rhodamine phalloidin excitation = 532 nm, emission BP filter = 560–675 nm; for DAPI excitation = 405 nm, emission band pass filter = 415-580 nm).

4.2.15 Demonstration of Cell Alignment with PEG-RGDS Pattern

To visually demonstrate the alignment of HUVECs and 10T1/2s with the PEG-RGDS pattern, the image of the RGDS pattern was skeletonized by first applying a threshold to the pattern image and then converting the image to a binary format. A skeletonize plug-in in ImageJ (NIH Bethesda, MD) was then utilized to create the line based pattern outline. The pattern skeleton was overlaid with both the original PEG-RGDS pattern image as well as the images from the cellularized hydrogel. To quantify this alignment, the two channels corresponding to the HUVECs and 10T1/2s were merged into a single channel using the “merge channels” function in ImageJ. The images of the patterned PEG-RGDS and the merged image of the cells were aligned and the degree of correlation between the two images quantified using the Mander’s correlation coefficient measured with the JACoP plugin in ImageJ¹⁴⁹.

4.3 Results

4.3.1 Development of Image-Guided TP-LSL Methodology

In order to develop biomimetic micropatterned materials, photocrosslinkable, acrylate-terminated PEG hydrogels have been employed. These materials have been rendered biodegradable through the incorporation of a matrix metalloproteinase-sensitive peptide (GGPQGIWGQGK, abbreviated PQ) into the backbone of a PEG-diacrylate derivative¹⁵⁰. Hydrogels formed from this polymer, once again referred to as PEG-PQ hydrogels, can act as a biodegradable “blank slate” into which custom designed 3D patterns of bioactive molecules may be incorporated via spatially controlled crosslinking of acrylate-modified cell adhesion peptides, growth factors, and other signaling molecules^{48,113,139}. As discussed in previous chapters, these acrylate-terminated moieties are amenable to 3D micropatterning via TP-LSL. In traditional TP-LSL, a tightly focused near infrared laser beam is raster scanned through a bulk PEG-PQ hydrogel permeated with an acrylate-modified biomolecule and photoinitiator. Upon excitation of the photoinitiator, the acrylated biomolecules are covalently crosslinked to the hydrogel scaffold via addition polymerization, and then unbound biomolecules are subsequently washed away. The non-linear nature of two-photon absorption confines this reaction to a very small volume at the focal plane of the focused laser beam¹⁵¹, enabling precise 3D control of the crosslinking reaction. Using galvanometers to direct the x-y position of the laser and piezoelectric focusing along the z plane, TP-LSL has been used to generate simple biomolecular patterns in acrylate-modified PEG hydrogels, with features as small as 1 μm in the lateral direction and 5 μm in the axial direction^{113,115}. Variation of laser intensity allows control over the concentration of the immobilized biomolecule, and

iterative patterning has been employed to immobilize multiple biomolecules in distinct patterns¹¹⁵.

To fabricate highly complex and biologically relevant micropatterns via TP-LSL, this chapter develops and implements a software package that translates an image into geometries that can be interpreted by a laser scanning microscope in order to drive the laser for precise image-guided patterning. When using 3D confocal images of tissue, each image “slice” can be translated into scanning instructions for one layer of equal thickness of the hydrogel scaffold. This process, known as image-guided TP-LSL, relies heavily on computational methods to handle and analyze structural data and is summarized in Figure 4-4. In this example, high resolution, 3D images of endogenous capillaries were utilized as pattern templates, with the resolution of the initial image dictating the maximum biomolecule pattern resolution within the hydrogel scaffolds. Each endogenous capillary template was obtained using confocal microscopy to image murine capillaries from a variety of tissues that were labeled through an intravascular injection of fluorescently labeled dextran (Figure 4-4a-b). A custom-made package of MATLAB scripts was then implemented to analyze the architecture of the vessels (see appendix for code). The vessel architecture was reconstructed in three dimensions using a mosaic of simple shapes to closely approximate the vascular structure for each optical section (Figure 4-4c). Next, the software exported this information as overlay files. Each overlay file, corresponding to a single optical slice, was written in the proper format for it to be read and interpreted by the Zeiss ZEN software package to define a region of interest (ROI) for each of the simple shapes that made up the calculated mosaic (Figure 4-4c). Finally,

custom-made ZEN macros were developed to classify these as “Acquisition” type ROIs, which were then used to spatially define where the laser scanned through each sample.

Initially, this process was utilized to pattern hydrogels (Figure 4-4d-e) with a vessel structure that remained constant throughout the z dimension, allowing us to assure that the axial spacing between patterning planes was appropriate to generate contiguous biomolecular patterns. To create such a pattern, a single overlay file was chosen, and used to repeatedly pattern multiple z-planes of a hydrogel throughout a total thickness of approximately 80 μm . In this example, a PEG-PQ hydrogel was first permeated with fluorescently labeled acrylate-PEG-Arg-Gly-Asp-Ser (PEG-RGDS-488). This biomolecule was then crosslinked into a pattern that mimics a cross section of vessels imaged in the retina (Figure 4-4e). RGDS was chosen as our patterned molecule because of its role in cell adhesion, and its demonstrated ability to guide endothelial cell migration in degradable hydrogels¹²³. A merged overlay between the original vessel cross section and the patterned hydrogel demonstrated that this process can recapitulate the structure from an endogenous vessel bed with high fidelity and excellent continuity (Figure 4-4f).

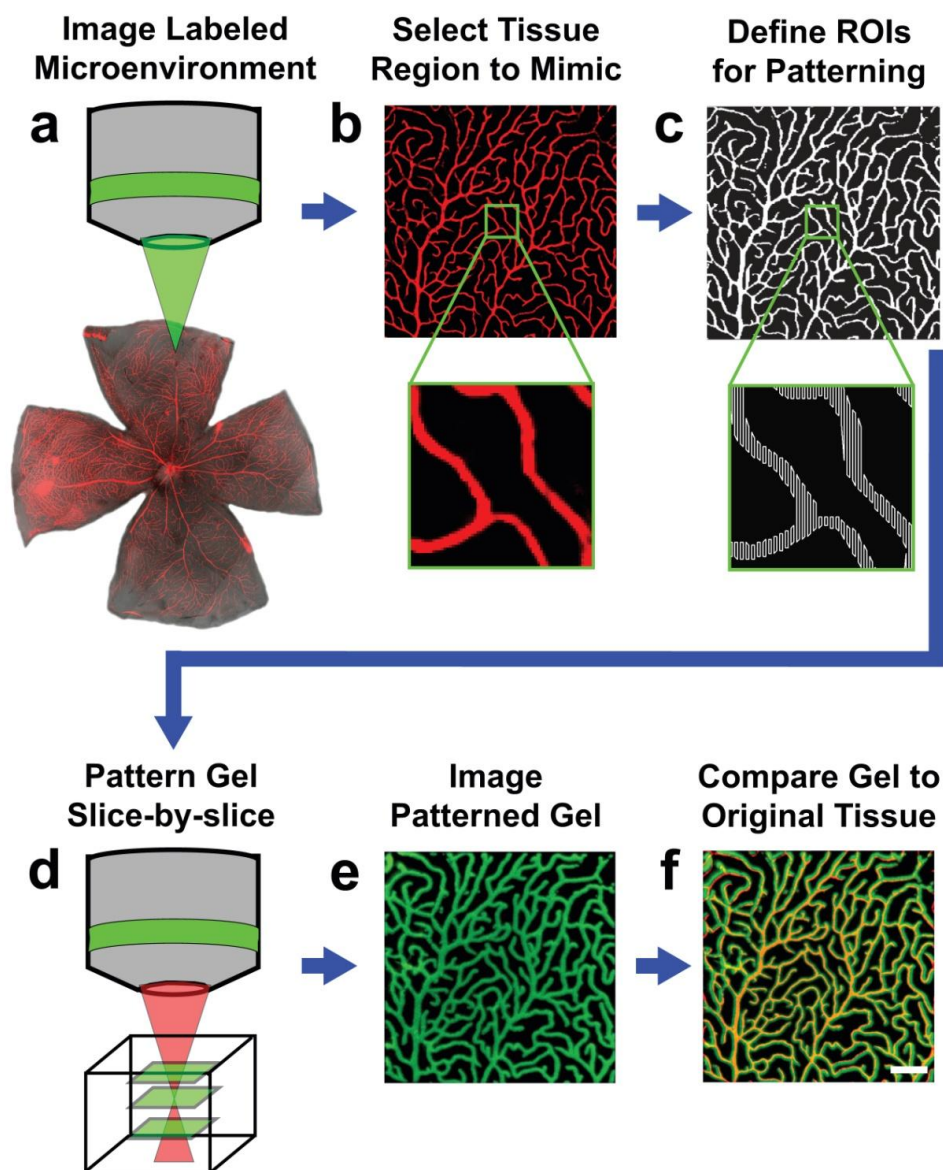


Figure 4-4: Image-Guided TP-LSL Methodology. (a) Fixed tissue with a labeled microenvironment was imaged in 3D using confocal microscopy (retinal microvasculature labeled with fluorescent Dextran is shown in this example). (b) An image from a single optical section of the retinal vessels. (c) A computational mosaic of regions of interest (ROIs) that precisely mimics the imaged optical section of the retinal vessels. (d) The mosaic of ROIs was used to control the scanning of the laser scanning microscope to pattern a single plane of the hydrogel. This patterning was repeated using the same mosaic of ROIs in multiple overlapping optical planes to expand the axial thickness of the 2D pattern. To pattern a 3D vascular structure, images from sequential optical sections of the vessel bed would be sequentially patterned to the corresponding plane in the hydrogel. (e) Imaged hydrogel after 2D patterning with PEG-RGDS-488. (f) Merge of the original vessel image (a) and the patterned hydrogel (e) demonstrating excellent patterning fidelity. Scale bar = 100 μm .

4.3.2 Three-Dimensional Patterning of Endogenous Vessel Features

Image-guided TP-LSL was next implemented for 3D patterning of endogenous vessel features derived from a variety of tissue types including the retina, cerebral cortex, and heart. Microvessels from each of these unique tissues were labeled with fluorescent dextran. A unique overlay file for each z-position within a 3D confocal image of vasculature was then generated and these files were iteratively utilized to three-dimensionally pattern PEG-PQ hydrogels. Each successive plane of the hydrogel was patterned with the appropriate spacing in the axial direction so that a one-to-one relationship between the endogenous vessel structure and the patterned structure was achieved. Optimal results were obtained when patterned z-planes in the hydrogel were spaced 3 μm apart. After washing unbound PEG-RGDS-488 from the PEG-PQ hydrogels, patterns were imaged via confocal microscopy. Inspection of projected images (Figure 4-5) demonstrates successful 3D biomimetic patterning of vasculature from the retina (Figure 4-5a-c), cerebral cortex (Figure 4-5d-f), and heart (Figure 4-5g-i). In each case, the 3D imaged endogenous vessels (Figure 4-5a,d,g) were precisely mimicked by 3D PEG-RGDS-488 hydrogel patterns (Figure 4-5b,e,h). A merge of the projected images of the endogenous vessels (red) with the projected patterned hydrogels (green) emphasizes nearly 100 percent overlap (yellow), thus demonstrating the high fidelity of the patterning process (Figure 4-5c,f,i).

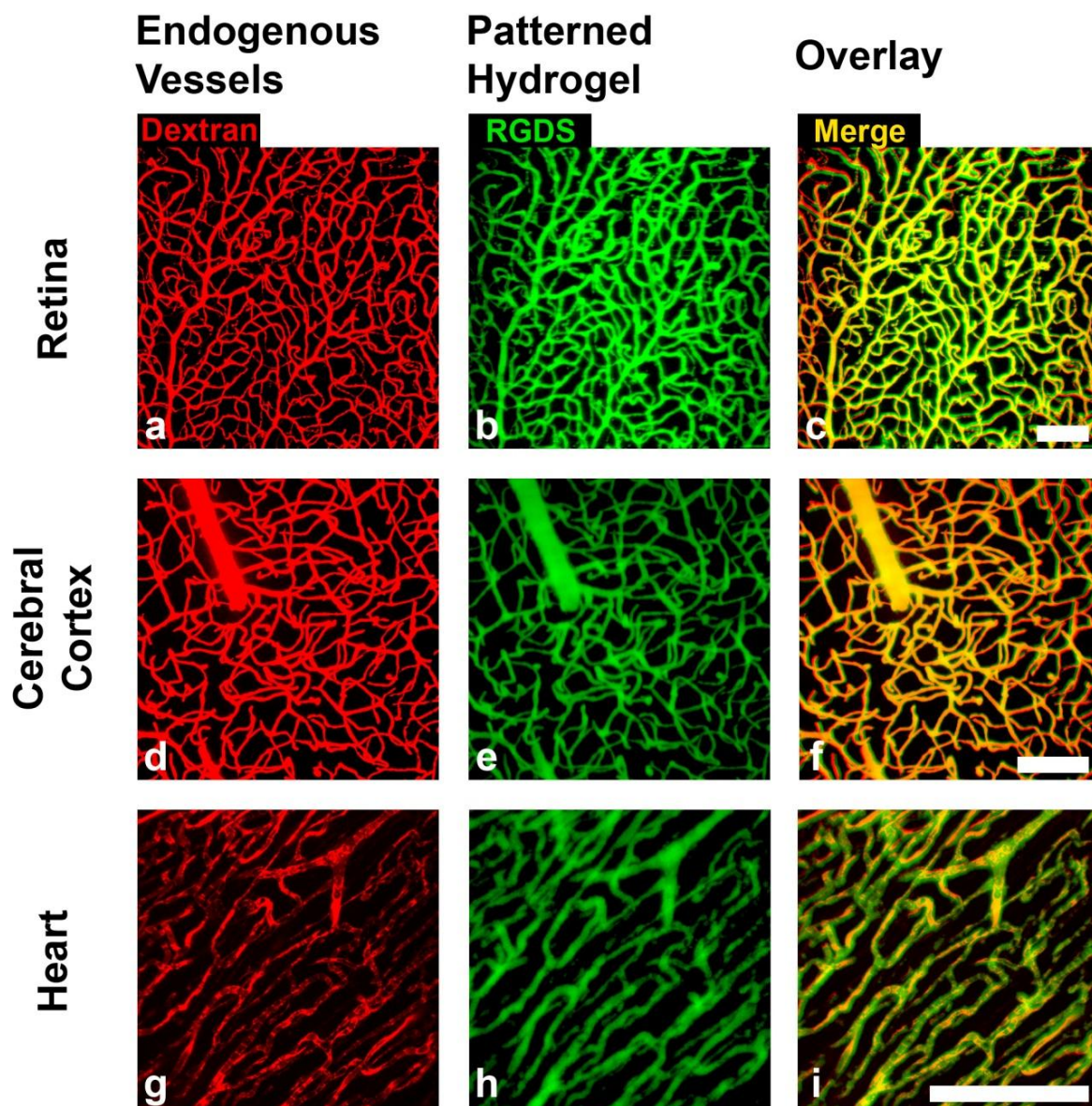


Figure 4-5: 3D Patterning to Recapitulate Multiple Tissue Types. All panels are maximum intensity projections of three-dimensional images. The high fidelity of 3D patterning via image-guided TP-LSL is demonstrated via mimicry of vessels in the retina (a-c), cerebral cortex (d-f), and heart (g-i). Images of the vessel beds in each of these tissues as labeled by fluorescent dextran are shown in (a), (d), and (g). Shown in (b), (e), and (h) are images of gels that were patterned in 3D with PEG-RGDS-488. The excellent fidelity of the patterning process is demonstrated by the overlay of each pair of images in (c), (f), and (i). Scale bars = 100 μm .

The microvascular structures patterned here vary dramatically in size and spatial orientation, and were chosen to demonstrate that image-guided TP-LSL is capable of fabricating hydrogels with complex patterns that mimic vessels over a range of length scales in a variety of vessel densities and orientations. Overall, inspection of hydrogel patterned images revealed that excellent lateral patterning fidelity was achieved. To assess axial patterning fidelity, xy, xz, and yz cross sections of the 3D hydrogels were compared to matched cross sections of the original vessel beds (Figure 4-6).

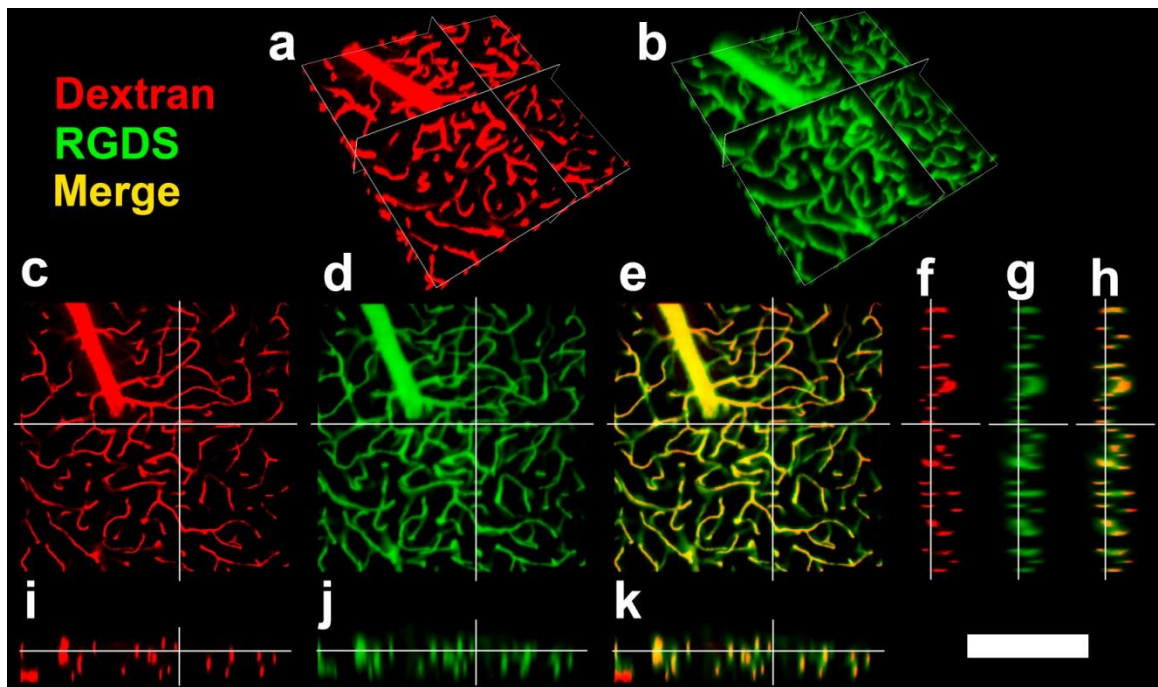


Figure 4-6: Lateral and Axial Fidelity of the 3D Patterning Process. (a) Orthogonal cross sectional planes cutting through a 3D reconstruction of vessels in the cerebral cortex. (b) Orthogonal cross sectional planes cutting through a 3D reconstruction of a hydrogel that was patterned to mimic these vessels. The locations of the orthogonal cross sections in (a) and (b) were coordinated between the two data sets using morphological landmarks. Each of the orthogonal cross sectional planes was then shown *en-face* to demonstrate the structure of the original vessel bed (c,f,i) and the patterned hydrogel (d,g,j). An overlay of each of these image pairs is also shown (e,h,k), and the overlap between the image of the vessel bed and the image of the patterned gel in each orthogonal plane demonstrates the fidelity of the patterning process. Scale bar = 200 μm .

Inspection of these cross sections demonstrated excellent patterning fidelity in all 3 dimensions. It should be noted, however, that close examination did reveal an approximately 5 μm expansion of patterned feature sizes in the axial direction. This limitation was expected due to the two-photon absorption point spread function¹⁵¹. Specifically, the two-photon absorption point spread function, which measures the extended, hazy cloud around an unresolved point image, predicts that features will be expanded due to resolution limits. It should be noted, however, that images used to create patterns represented only the lumens of vessels and therefore a slight expansion of patterned features may be beneficial to account for the thickness of the capillary wall. Taking this factor into consideration, the patterning parameters presented here allow for the recapitulation of even the smallest individual capillaries imaged within these 3D vascular beds.

4.3.3 Patterning Multiple Biochemical Features of a Complex Tissue

To further extend this novel image-guided photopatterning technology, it was desirable to fabricate materials that recapitulate multiple biochemical features of a complex tissue. As an example, iterative TP-LSL patterning was used to engineer hydrogels that mimicked both the neural and vascular components of the subependymal zone (SEZ) neural stem cell (NSC) niche. The SEZ is a unique brain microenvironment where NSCs persist throughout adult life in close association with capillaries. Numerous studies have shown that angiocrine factors released by the microvasculature in this niche are critically important for NSC maintenance^{143,152}, and recent evidence suggests that the close association of NSCs with the microvasculature and its laminin-rich microdomains is functionally important for regulating neurogenesis^{142,143,153}. The importance of these

structural relationships between the NSCs and the vessels in this region makes imitating the NSC niche an excellent application for this image-guided TP-LSL method.

For a blueprint of the NSC niche, a high-resolution image of vessels and neural progenitor cells in an *en-face* view of the SEZ was obtained¹⁵⁴. After dissecting out the SEZ from the brains of mice, the tissue was immunostained with antibodies against PECAM-1 to mark the blood vessels and Ki67 to mark the neural progenitor cells (Figure 4-7a).

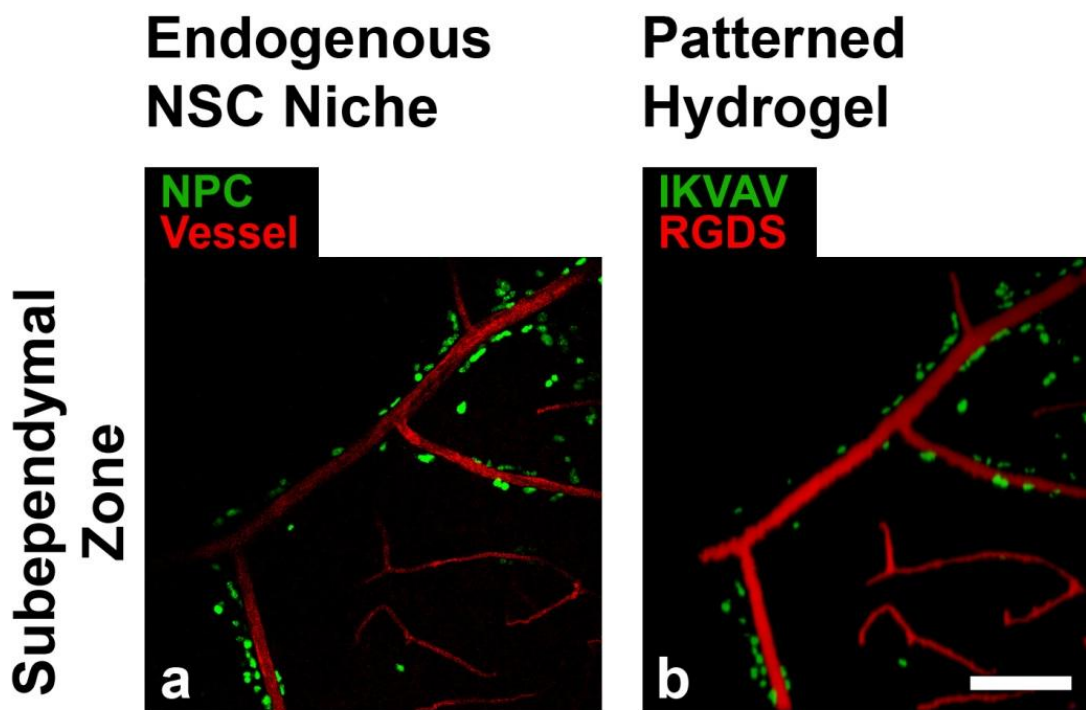


Figure 4-7: Recapitulating the Subependymal Zone Vascular Niche Microenvironment. (a) An *en-face* view of the mouse subependymal zone neural stem cell niche after immunostaining, with vasculature stained using antibodies against pecam-1 (pseudocolored red), and neural progenitor cells stained using antibodies against Ki67 (pseudocolored green). (b) A patterned PEG-PQ hydrogel is shown in which a PEG-RGDS-488 pattern (pseudocolored red) recapitulates the PECAM-1 vessel staining and a PEG-IKVAV-633 pattern (pseudocolored green) recapitulates the Ki67 neural progenitor cell staining. Scale bar = 100 μm .

Although Ki67, a cell-cycle marker of proliferative cells, is in general not neural specific, by co-immunostaining with other markers, previous work has verified that it can be used in the SEZ as a dependable marker of neural progenitor cells^{142,143}. To mimic these two distinct biochemical patterns, iterative TP-LSL was then utilized to pattern a hydrogel with two distinct peptides, each with a unique fluorescent label. PEG-RGDS was patterned to once again mimic the vessel architecture, but the peptide Ile-Lys-Val-Ala-Val (IKVAV) conjugated to PEG-monoacrylate was utilized for the Ki67 pattern. The IKVAV peptide, derived from the α_1 chain of laminin, was chosen to mimic the laminin-rich microdomains that regulate neurogenesis in the NSC niche^{142,153}. Both molecules were effectively patterned within the PEG-PQ hydrogel, with the PEG-RGDS-488 pattern mimicking the vascular PECAM-1 staining, and the PEG-IKVAV-633 pattern mimicking the neural progenitor Ki67 staining (Figure 4-7b). These results demonstrate that image-guided TP-LSL can be successfully employed to engineer biomaterials that faithfully recreate multiple essential elements of endogenous cellular microenvironments.

4.3.4 Engineering a Biomimetic Microvasculature

An overarching goal of this thesis is to develop bioactive biomaterials that can spatially control cellular organization to recapitulate tissue structures. Specifically, the ability to spatially control the formation of intricate microvascular networks derived from real tissue structures is an important step toward forming functional tissue engineered therapeutics. As discussed previously in this chapter, when HUVECs and mesenchymal progenitor 10T1/2 cells are encapsulated within homogeneous, unpatterned PEG-PQ hydrogels with PEG-RGDS, the cells are observed to organize into capillary-like tubule

structures²⁸. However, these tubules have been shown to be random and disorganized in their structure. The development of image-guided TP-LSL offers an opportunity to spatially control the organization of engineered microvascular networks to mimic tissue-derived capillary structures. Specifically, image-guided TP-LSL has been utilized to spatially pattern PEG-RGDS in order to dictate the organization of cellular tubule structures, guiding vessel network formation to mimic the microvasculature of the cerebral cortex. Fluorescently-labeled HUVEC and 10T1/2 cells were homogeneously entrapped in PEG-PQ hydrogels by mixing with the PEG-PQ polymer solution prior to crosslinking. The cell-laden hydrogels were then subjected to image-guided TP-LSL to immobilize PEG-RGDS using a pattern based on images from cerebral cortex capillaries (Figure 4-8a). After 24 h in culture, cellular organization into vessel networks was assessed via confocal microscopy.

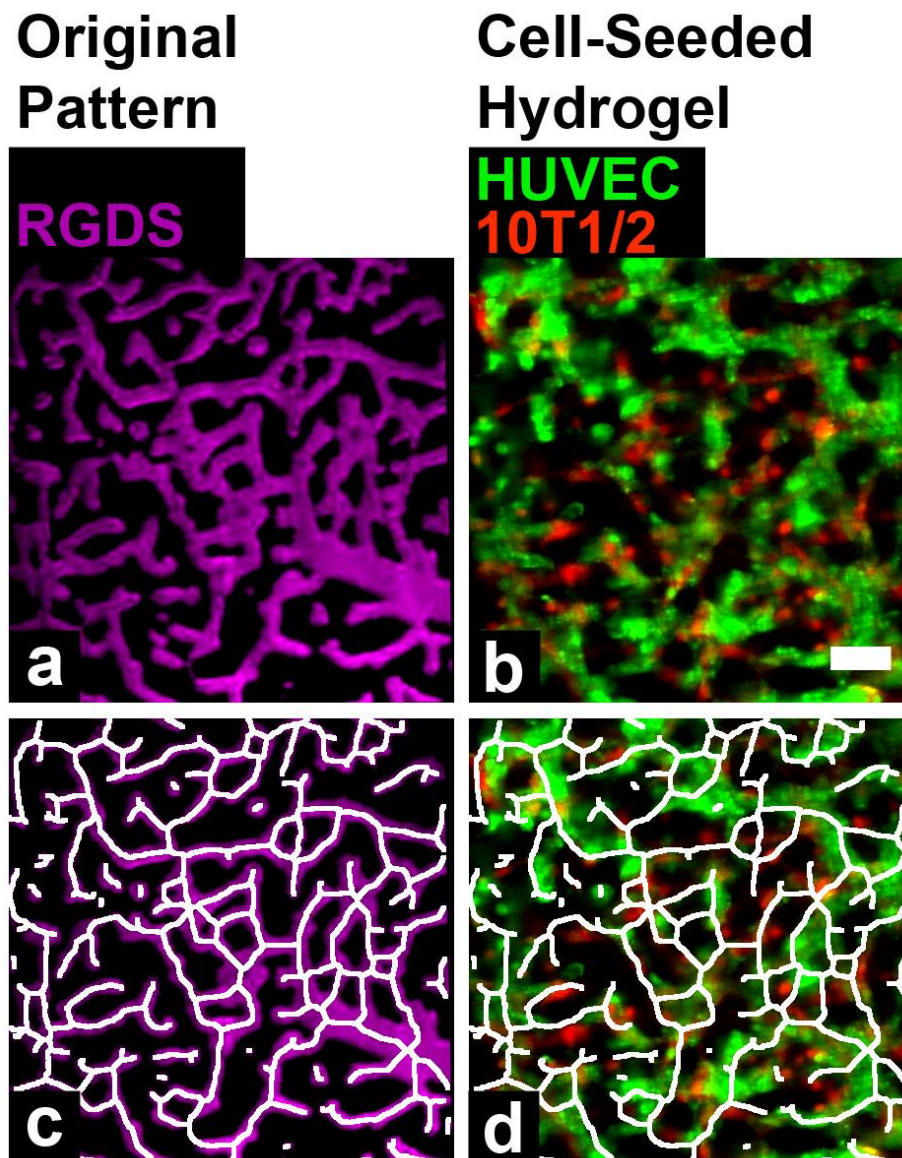


Figure 4-8: Guiding Vascular Network Formation in Cellularized Hydrogels.

(a) A degradable PEG-PQ hydrogel with a fluorescent PEG-RGDS pattern (magenta) mimicking the vasculature from the cerebral cortex. (b) HUVECs (green) and 10T1/2s (red) have formed intricate tubule networks that after 24 hours align with the PEG-RGDS pattern of the cerebral cortex vasculature. (c) An artificial skeletonized tracing to highlight the pattern structure. (d) The skeletonized tracing of the pattern has been overlaid with the organized HUVECs (green) and 10T1/2s (red) to demonstrate excellent alignment of the tubules to the patterned structure. Scale bar = 50 μm .

The results demonstrated that HUVECs and 10T1/2s (Figure 4-8b) organized into complex tubule networks in the patterned hydrogel. To assess the degree to which the cells followed the RGDS pattern, the image of the PEG-RGDS pattern was skeletonized (Figure 4-8c) and the skeleton was overlaid atop the image of the cells (Figure 4-8d). This comparison between the cells and the skeletonized pattern qualitatively demonstrates that the engineered vessel networks in this hydrogel closely mimic the arrangement of the cerebral cortex vasculature in our source image. To quantify this degree of overlap, the Mander's correlation coefficient was measured using the JACoP plugin in ImageJ¹⁴⁹; our measured value indicated that 92.3 % of the patterned PEG-RGDS co-localized with HUVECs and 10T1/2s, thereby affirming a high degree of spatial control over tubule formation in this hydrogel.

To demonstrate the versatility of image-guided TP-LSL to spatially guide vessel formation, this process was repeated with a vascular pattern from the subependymal zone NSC niche. In this case, the HUVECS and 10T1/2s were imaged immediately after patterning, and then again after 7 days. Immediately after patterning, the encapsulated HUVECs and 10T1/2s had not yet had time to assemble into vessels and were seen distributed throughout the PEG-PQ hydrogel (Figure 4-9a). However, after 7 days in culture, the endothelial cells had coalesced to form highly organized tubules (Figure 4-9b). To emphasize the alignment of these tubules to the chosen vascular pattern of RGDS, a skeletonized tracing was drawn over the RGDS patterned structure (Figure 4-9c). This tracing was then overlaid on the image of organized tubules (Figure 4-9d), demonstrating that the tubule structures aligned closely with the RGDS pattern, and therefore, mimicked the structure of the microvasculature from the endogenous SEZ NSC

niche. In this way, image-guided TP-LSL has shown the ability to organize vascular networks into biomimetic structures with diverse vessel densities and spatial organizations.

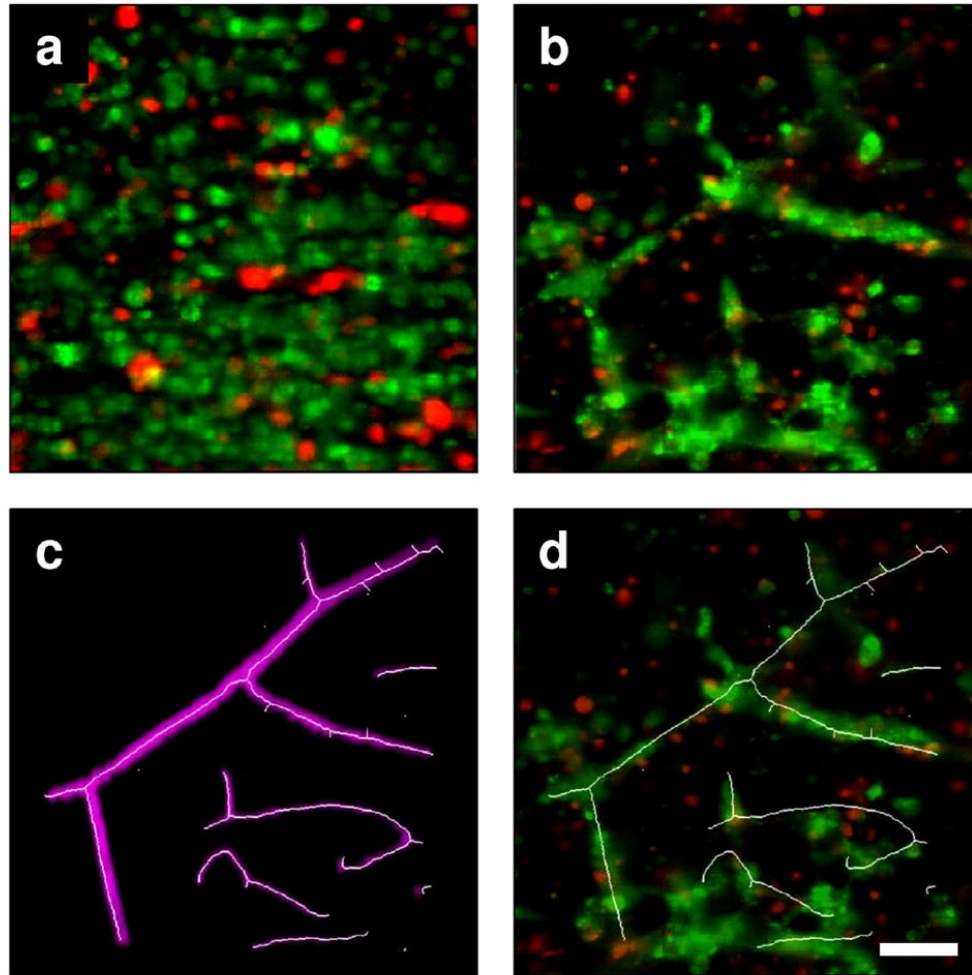


Figure 4-9: Guiding Vessel Network Formation to Mimic the Vasculature from the Neural Stem Cell Niche. (a) HUVECs (green) and 10T1/2s (red) encapsulated in a PEG-PQ hydrogel immediately after patterning an RGDS structure into the shape of the vasculature from the subependymal zone neural stem cell niche. (b) HUVECs and 10T1/2s assembled into an organized vessel structure within 7 days. (c) The RGDS pattern of the vessels from the subependymal zone neural stem cell niche. A skeleton trace has been applied to the image to better indicate the vessel structure. (d) The tubules from (b) with the skelotonized tracing from (c). The close alignment of the tubules to the skeleton tracing indicates precise guidance of the vessels into the organized structure of the vasculature from the neural stem cell niche. Scale bar = 100 μm .

These guided vessel networks were next investigated in terms of their development and precise structure. Specifically, in order to better visualize guided vessel network formation, HUVECs and 10T1/2s were first encapsulated within PEG-PQ hydrogels and PEG-RGDS was patterned into the biomimetic SEZ NSC vascular structure. The hydrogels were then fixed after 2 days in culture, and were stained to illuminate cellular nuclei (DAPI), f-actin (phalloidin) as well as apoptosis marker caspase 3.

3. Encapsulated HUVECs and 10T1/2s in PEG-PQ with and without PEG-RGDS throughout the hydrogels were fixed and stained in a similar manner as controls. The DAPI and phalloidin staining of the cells encapsulated with PEG-RGDS throughout the hydrogels indicated that organized tubule structures were forming with caspase 3 staining localized to the center of the more developed vessel tubules (Figure 4-10a-d). This result was expected as some cells within the center of forming vessels must apoptose in order to form hollow lumens. Contrastingly, without any PEG-RGDS in the hydrogels, HUVECs and 10T1/2s remained highly unorganized, with approximately 96% of the cells positive for active caspase 3 (Figure 4-10e-h). With the patterned hydrogels, the DAPI and phalloidin staining indicated that vessel networks were forming precisely along the PEG-RGDS pattern fabricated within the hydrogel (Figure 4-10i-j). Caspase 3 staining within the patterned hydrogels was present within the center of the forming vessels, indicating the cellular structures were likely in the process of controlled apoptosis to form lumens. Caspase 3 staining was also present in approximately 82% of cells outside of the PEG-RGDS patterned area. Such caspase 3 staining may indicate that organized vessel structures are formed largely due to cell apoptosis in non-patterned regions with cells in and around the patterned regions coalescing to form organized biomimetic tubules. While

further investigation is necessary to confirm the precise molecular mechanism of the formation of guided tubule networks, the work in this thesis stands as a significant step towards the engineering of spatially guided blood vessels for use in tissue engineering.

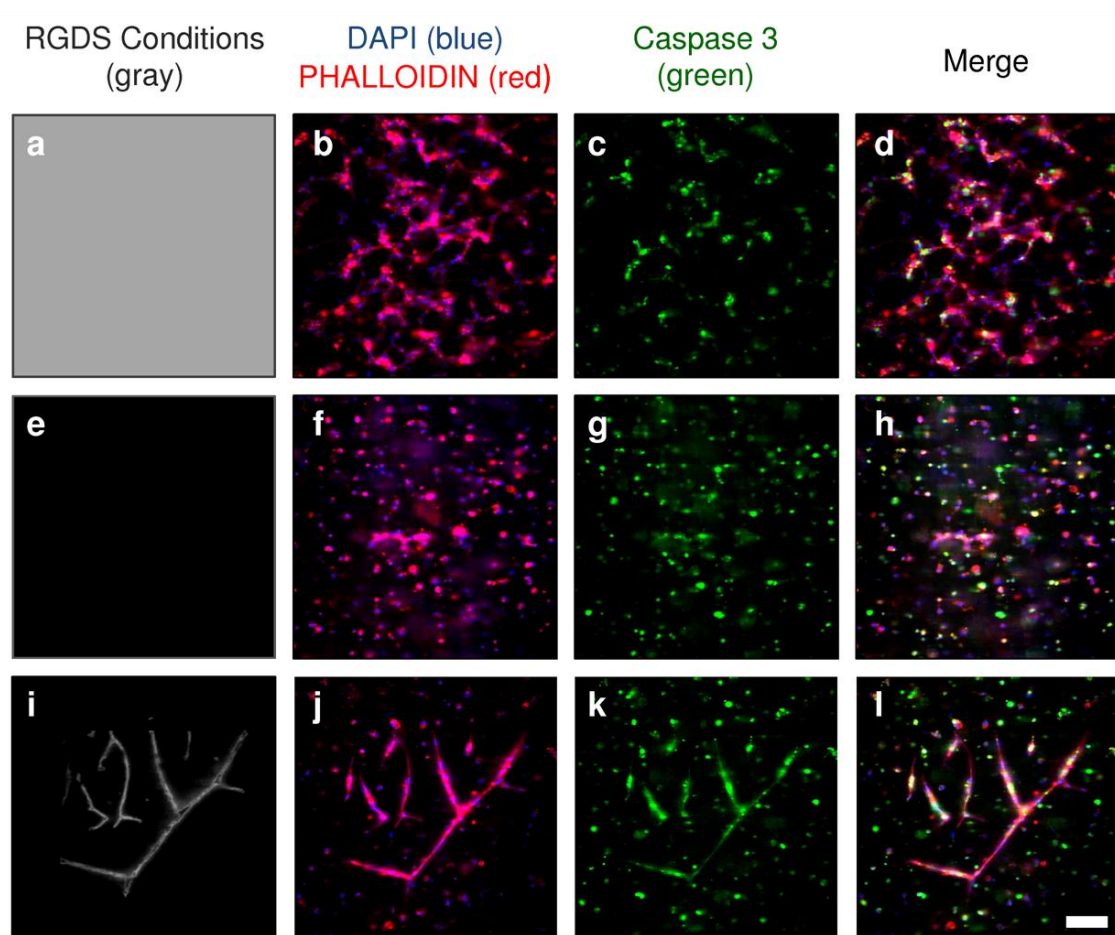


Figure 4-10: Investigating the Development of Guided Vessel Networks. (a-d) HUVECs and 10T1/2s encapsulated in a PEG-PQ hydrogel with PEG-RGDS throughout the hydrogel. (e-h) HUVECs and 10T1/2s encapsulated in a PEG-PQ hydrogel with no PEG-RGDS. (i-l) HUVECs and 10T1/2s encapsulated in a PEG-PQ hydrogel with PEG-RGDS patterned into the shape of the vessels from the SEZ NSC niche. (a,d,i) Indicates presence or absence of PEG-RGDS. (b,f,j) DAPI and phalloidin staining of cellularized PEG-PQ hydrogels. (c,g,k) Caspase 3 staining of cellularized PEG-PQ hydrogels. (d,h,l) Merge of the DAPI and phalloidin staining with the caspase 3 staining. All hydrogels were fixed after 2 days in culture. Scale bar = 100 μm .

4.4 Discussion

The development of the image-guided TP-LSL process allows for endogenous images to guide the facile customization of biomaterial design. In this chapter, images of microvessels from the heart, brain, and eye were used as templates to guide biomimetic patterning of PEG-RGDS within a degradable PEG based hydrogel with the PEG-RGDS patterns mimicking the vessel structures precisely in all three dimensions. While microvessels from the heart, brain, and eye were demonstrated as examples in this chapter, image-guided TP-LSL is directly applicable to imaged vessel networks from other imaged tissues such as the liver, kidney, and lung. The results in this chapter also demonstrate that multiple aspects of tissues can be patterned within a single microenvironment. Specifically, the murine neural stem cell niche was stained for both neural stem cells with one antibody (Ki67) and the endothelial cells of microvessels with a different antibody (PECAM). PEG-RGDS was then patterned into a PEG hydrogel in the shape of the microvessels, while a different peptide, PEG-IKVAV, was patterned into the structure of the neural stem cells. Such capabilities to directly pattern multiple biological molecules into distinct biomimetic structures within hydrogel scaffolds will likely be directly applicable to tissue engineering, as scientists look to control the organization and function of multiple cell types on the microscale. Almost any acrylated-PEG-peptide or protein may be three dimensionally patterned into any imaged tissue structure. For example, lymphatic vessels, blood vessels and nerves could be patterned into a single microenvironment, with specifically chosen peptides or proteins mimicking each structure. Additionally, smaller repeating structures of larger organs, such as liver

lobules or kidney nephrons could be used as templates to promote the organization of different cell types into cohesive, functional tissue units.

Finally, PEG-RGDS patterns were utilized in this chapter to guide the formation of engineered vessel networks that closely mimicked endogenous vessel structures in terms of both vessel density and vessel orientation. This work utilized a single mosaic of ROIs from the cerebral cortex that was utilized to pattern PEG-RGDS into the cellularized hydrogel that was constant in the Z direction. Future research will use sequential image templates with matching spacing to the original tissue so that engineered vessels may more accurately mimic endogenous vessels as their structure changes axially.

The ability to dictate the structure of engineered microvasculature in a biomimetic manner has important implications across the field of biomaterials and regenerative medicine. Our preliminary results have utilized acrylate-modified derivatives in a PEG hydrogel, but this approach is easily translatable to other materials and crosslinking chemistries that are amenable to TP-LSL^{45,123}. Soon researchers will look to flow media through guided vessel networks in order to allow for specialized control of nutrient and gas exchange in engineered tissues. Ultimately, scientists can look to fabricate hydrogels with a 3D tissue specific vasculature on the path towards functional, large-scale tissue engineered therapeutics. Additionally, complex physiological information may be implemented to fabricate 3D scaffolds capable of properly controlling stem cell maintenance and differentiation for applications in regenerative medicine and treatment of disease. Finally, the ever-expanding knowledge of tumor microenvironments may be applied to engineer *in vitro* 3D tumor models to probe potential cancer therapeutics.

Overall, image-guided TP-LSL now serves as an important tool for bioengineers to develop and probe engineered tissues.

4.5 Conclusion

In this chapter, a novel materials engineering approach, known as image-guided two-photon laser scanning lithography, has been developed that effectively bridges the disconnect between our knowledge of the endogenous cellular microenvironment and our ability to fabricate biomimetic materials on the microscale. Specifically, images of endogenous capillaries were utilized in combination with two-photon laser patterning to guide the 3D patterning of PEG-RGDS within enzymatically degradable, PEG-PQ hydrogels. PEG-RGDS patterns precisely mimicked microvasculature from multiple tissues with high fidelity in three dimensions. Further, multiple aspects of a single tissue were recreated, with PEG-RGDS patterns mimicking vessels from the brain, and PEG-IKVAV patterns mimicking neural stem cells in the brain. Finally, image-guided TP-LSL was utilized to direct the formation of HUVECs and 10T1/2s as they assembled into a vessel network that mimicked the structure of the vasculature in the cerebral cortex of the brain. Together, these results provide a new tool set to build engineered cellular microenvironments directly based on images from endogenous tissues. With the biological blueprints now unlocked, countless features of the cellular microenvironment may soon be recapitulated in synthetic scaffolds, leading the way for the development of a number of novel biomimetic technologies.

Chapter 5: Conclusions and Future Directions

5.1 Thesis Summary and Conclusions

The overarching goal of tissue engineering is to provide medical solutions for patients with diseased or damaged tissues and organs. While much progress has been made over the last 25 years, a number of significant obstacles remain. Perhaps the most significant challenge will be to successfully vascularize large, three-dimensional tissue constructs. It is now well known that cells more than several hundred microns from the nearest capillary suffer from hypoxia and eventual cell death⁸. Therefore, in order to engineer large, functional tissues, it will be required to design and implement a complex series of microvascular networks to promote sufficient gas exchange and nutrient supply to sustain high cell viability.

A number of researchers have begun to address this challenge through the successful assembly of vascular cells into microvascular tubules capable of sustaining flow^{28,29,35,38,141}. However, to this point, engineered vascular tubules have generally possessed a random and disorganized structure that limits their ability to allow sufficient nutrient transport for individual tissues. In healthy tissues within the body, the microstructure of the vasculature is highly ordered and specifically designed to promote the ability of each individual tissue to function properly⁹. Therefore, the next step in developing tissues with a functional microvasculature is to develop tools that enable micrometer control over the density and spatial orientation of engineered capillaries so that artificial vascular networks might precisely mimic the microvasculature of endogenous tissues.

This thesis has developed a 3D photolithographic patterning technology, known as two-photon laser scanning lithography (TP-LSL), to manipulate the physical and biochemical microenvironment of poly(ethylene glycol)(PEG)-based hydrogels. Patterned PEG-based hydrogels were then used to precisely guide cellular migration and organization. In the TP-LSL technique, PEG-based hydrogels were first fabricated and permeated with PEG-RGDS and a photoinitiator. A two-photon laser was then utilized to covalently crosslink PEG-RGDS into specific, 3D regions of the PEG-based hydrogel. After washing away the unbound PEG-RGDS, only the specified PEG-RGDS volumes were capable of promoting cell adhesion and migration within the otherwise non-adhesive hydrogel.

The capabilities of TP-LSL were investigated and expanded upon so that the technology might be better applied to a variety of bioengineering applications. The resolution limits of TP-LSL were tested, and PEG-RGDS patterns as small as 1 μm in the lateral (xy) direction and 5 μm in the axial (z) direction were generated. A variety of 3D patterns of PEG-RGDS were then fabricated, with the PEG-RGDS concentration easily controlled via variation of the laser intensity, scan speed or initial soaking concentration. Finally, it was shown that different kinds of biomolecules, in addition to the fibronectin derived RGDS, could be iteratively micropatterned into a single hydrogel environment. This ability will allow TP-LSL to mimic more biochemically complex microenvironments such as those seen *in vivo*. Overall, these initial results significantly advanced and clarified the micropatterning capabilities of TP-LSL, and thereby, provided a new set of tools to investigate cell behavior.

TP-LSL patterning was next employed to guide cell migration and probe how cells move under various micropatterned conditions. TP-LSL was used to fabricate PEG-RGDS patterns on the surface of non-degradable PEG-DA hydrogels (2D) and in the interior of enzymatically degradable PEG-PQ hydrogels (3D). A ninhydrin assay was performed to determine the approximate concentration of PEG-RGDS in these patterns. HT1080 cells were then seeded onto the surface of the patterned PEG-DA hydrogels and encapsulated adjacent to the patterned PEG-PQ hydrogels and migration was monitored using time-lapse microscopy.

HT1080s were observed to migrate over 5 times faster and with markedly less persistence on 2D surfaces than within 3D hydrogels. Further, cells migrating in 3D were smaller and more elongated than those in 2D. When the dimensions of PEG-RGDS patterns were decreased, cells in both 2D and 3D were observed to have increased persistence, as the cells were forced to move in straighter paths with less random motion. This thesis also investigated cell migration with various PEG-RGDS concentrations in both 2D and 3D. On 2D hydrogel surfaces, cell speed was seen to have a biphasic dependence on PEG-RGDS concentration, with the maximal speed occurring at an intermediate level of PEG-RGDS. In 3D, the migration of leading cells invading into the PEG-RGDS patterns also demonstrated a biphasic dependence on PEG-RGDS concentration. This thesis then investigated the effects of varying the hydrogel composition and showed that cells invaded significantly farther into 5% (w/w) hydrogels compared to 10% (w/w) hydrogels. Finally, the effect of time on 3D cell migration was probed, and it was shown that cell speed and persistence were increased when cells had been migrating for 2 days as opposed to 1.

The combination of the PEG-based biomaterial system with TP-LSL serves as a unique platform to quantitatively investigate cell motility. This study of HT1080 cell migration highlights differences in speed and persistence based on variation of adhesive ligand, hydrogel composition, and patterned area for both 2D and 3D cell migration. Importantly, this experimental system has allowed for elucidation of some of the multiple complex factors involved in cell migration, with typical confounding factors being independently controlled. The development of this unique platform will allow researchers to probe how cells behave within increasingly complex 3D microenvironments that mimic specifically chosen aspects of the *in vivo* landscape.

To fabricate truly biomimetic microenvironments, this thesis next introduced image-guided TP-LSL to pattern biomolecules into exact structures found in endogenous tissues, including those of the critical microvasculature. Image-guided TP-LSL converted images of tissue microenvironments into instructions for a two-photon laser so that PEG-RGDS was patterned into the precise microscopic structures from images of endogenous tissues. Images of the 3D microvasculature from the heart, retina, and brain were used as templates to fabricate adhesive patterns within PEG-PQ hydrogels. The micropatterns exactly mimicked the original microvascular structure in all 3 dimensions. Image-guided TP-LSL was also used to iteratively immobilize multiple bioactive moieties to precisely mimic several distinct aspects of endogenous tissue microenvironments. As an example, PEG-RGDS was patterned to mimic the structure of the microvasculature of the brain while a different bioactive molecule, PEG-IKVAV, was patterned to mimic adjacent neural stem cell structure. The ability to replicate multiple aspects of tissues in an *in vitro* biomaterial microenvironment will allow future researchers to model a limitless number

of complex biological scenarios in the laboratory. Finally, this thesis has demonstrated the ability to guide cellular organization to mimic structures from endogenous tissues. Specifically, vascular cells were homogeneously seeded in a PEG-based hydrogel and immobilized PEG-RGDS was patterned into a structure derived from images of a tissue microvascular network. The cells rapidly organized into a vessel network matching the original tissue image with good fidelity. Image-guided TP-LSL has enabled the successful engineering of microvasculature structures that precisely mimic the vessels in endogenous tissues in terms of both vessel density and orientation. These engineered vessels stand as an important accomplishment for tissue engineering, and bring the community one step closer to artificial tissue therapeutics to save patients' lives.

In summary, this thesis has developed a novel 3D photopatterning technique, known as two-photon laser scanning lithography, and utilized this technique to investigate how cells interact and organize, with applications for both biological science and tissue engineering. These contributions mark an important step forward for tissue engineering and biomaterial science, and lead the way into an exciting future of exploration of micropatterned materials for a variety of biomimetic applications.

5.2 Future Directions

5.2.1 TP-LSL Patterning of Proteins

The development of TP-LSL will allow for the biomimetic fabrication of tremendously complex cellular microenvironments within biomaterials. While 3 different bioactive peptides were patterned into PEG-based hydrogels within this thesis (PEG-RGDS, PEG-CS-1, PEG-IKVAV), a multitude of alternative biological moieties have previously been incorporated into PEG-based hydrogels and would be readily amenable

to patterning via TP-LSL. For example, vascular endothelial growth factor⁴⁷, platelet derived growth factor-BB¹³⁹, and ephrin-A1⁴⁶ have been shown to maintain their bioactivity after incorporation into PEG-based hydrogels. These proteins, among others, could be micropatterned via TP-LSL into 3D structures within PEG-based hydrogels to explore how cells respond in various pattern configurations. Specifically, PEG-VEGF could be patterned into a 3D gradient that mimics the gradient formed during angiogenesis *in vivo*. Endothelial cell sprouting from engineered vessels could then be investigated in a controlled biomaterial environment to provide insight into the angiogenic process.

5.2.2 Cell Migration Under Various Patterned Conditions

The use of TP-LSL to guide cell migration allows scientists to easily image and track how small numbers of cells migrate in 3D under a variety of controlled, patterned conditions. Future experimental work will be interfaced with developing modeling techniques to gain a more in-depth understanding of cell motility. Further, TP-LSL will allow for the fabrication of a number of 3D geometries of cell adhesive bioactive molecules that have not been previously studied. For example, spherical islands of PEG-RGDS with varying size and spacing could be patterned to probe the limits of cell adhesion and subsequent cell migration within 3D hydrogels. Differing amounts of PEG-PQ macromer could also be patterned into preformed PEG-PQ hydrogels to observe how cells migrate within hydrogels in response to local increases in crosslinking density and material stiffness. Immunostaining for specific integrins or focal adhesions under these and other pattern configurations should help to better define the modes and mechanisms of 3D cell migration. Additionally, exploring differences in 3D cell migration between

various cell types will also be of utmost importance. For example, investigating differences in cell migration between metastatic cancer cells and primary healthy cells could provide insight into biochemical mechanisms of cancer metastasis and potential targets for cancer treatment or prevention.

5.2.3 Image-Guided TP-LSL for Tissue Engineering and Model Development

Image-guided TP-LSL has the potential to be widely adopted by bioengineers as a tool to mimic specific aspects of the endogenous microenvironment within biomaterials. While image-guided TP-LSL was developed using acrylate-modified derivatives in a PEG-based hydrogel, the approach is easily translatable to other materials and crosslinking chemistries that are amenable to TP-LSL^{122,155}. Using image-guided TP-LSL, carefully chosen peptides or proteins may be three dimensionally patterned into any imaged tissue structure for tissue engineering applications. For example, the structure of neurons innervating muscle could be patterned into biomaterials to guide the assembly of biomimetic neural networks. Additionally, the smaller repeating structures of larger organs, such as liver lobules or kidney nephrons, could be used as templates to promote the organization of different cell types into cohesive, functional tissue units. Extracellular matrix proteins may also be patterned into fibrillar configurations to introduce desired anisotropy in tissue engineered heart valves.

Image-guided TP-LSL may also be utilized to develop *in vitro* biomaterial models of diseased or developing tissue. For example, the disorganized, leaky vasculature of tumors could be patterned and used to guide vessel formation. This engineered tissue model could then provide insight into the growth and evolution of tumors into metastatic

cancer. Alternatively, patterning prenatal tissues structures could provide a model to study normal developmental behaviors and cues as to how best deal with abnormalities.

5.2.4 Engineering Functional Vascularized Tissues

The successful guidance of vessel networks to mimic the endogenous microvasculature presented herein stands as a crucial step towards the fabrication of functional, vascularized tissues and organs; however, significant hurdles remain. In this thesis, a constant vessel template was micropatterned throughout the z dimension to guide the formation of an engineered vessel network. Future studies will utilize 3D pattern templates to mimic endogenous vessel beds as they vary throughout the axial dimension.

The next step to forming a truly functional vasculature will be to ensure that engineered vessels can maintain physiological flow rates. Researchers have recently shown success in utilizing microfluidics to induce flow within unorganized engineered vascularized networks¹⁴¹. Future research will focus on combining microfluidic systems with image guided TP-LSL in order to support flow within biomimetic engineered vessels. Once flow through these networks has been achieved, researchers will investigate the ability of these artificial capillaries to facilitate increased transport of nutrients and waste that could subsequently allow for increased cell viability within thicker tissue constructs. Future studies will also investigate the mechanical stability of the engineered microvascular networks compared with those seen *in vivo*. As progress continues, scientists will likely move away from HUVECs and 10T1/2s toward more clinically relevant cell types. For example, blood-derived endothelial colony forming

cells and mesenchymal stem cells can both be obtained non-invasively from humans and can be cultured together to form engineered vascular networks¹⁵⁶.

In this thesis, relatively small biomimetic microvascular networks were fabricated with the total volume of the vessels covering only about $500 \times 500 \times 100 \mu\text{m}$. Future work will move to patterning larger volumes through the use of microscope objectives with a larger view field and working distance. For example, researchers have recently designed two-photon laser systems with $2 \mu\text{m}$ resolution that are capable of scanning a $2.5 \times 2.5 \times 1.2 \text{ mm}$ volume¹⁵⁷. Such a system could be utilized to fabricate a larger scale biomimetic vasculature. A quilt work strategy could then be utilized to pattern multiple vascular beds adjacent to one another to fabricate functional engineered vascular networks that are on the size order of human tissues and organs.

5.2.5 Summary

In summary, this thesis has developed a novel 3D photopatterning technology, known as two-photon laser scanning lithography, capable of designing complex mechanical and biochemical microenvironments within biomaterials. These biomimetic landscapes were then utilized to guide cell migration and organization for applications in both cell science and tissue engineering. The contributions discussed herein should be widely applicable to the field of bioengineering, and lead the way to a number of significant scientific discoveries.

Chapter 6: References

1. UNOS United Network for Organ Sharing. (2012).at <www.unos.org>
2. Langer, R. & Vacanti, J.P. Tissue engineering. *Science* **260**, 920-926 (1993).
3. MacNeil, S. Progress and opportunities for tissue-engineered skin. *Nature* **445**, 874-880 (2007).
4. Tsai, R.F., Li, L.M. & Chen, J.K. Reconstruction of damaged corneas by transplantation of autologous limbal epithelial cells. *New England Journal of Medicine* **343**, 86-93 (2000).
5. Macchiarini, P. *et al.* Clinical transplantation of a tissue-engineered airway. *The Lancet* **372**, 2023-2030 (2008).
6. Atala, A., Bauer, S.B., Soker, S., Yoo, J.J. & Retik, A.B. Tissue-engineered autologous bladders for patients needing cystoplasty. *Lancet* **367**, 1241-1246 (2006).
7. Brun, P. *et al.* Characteristics of repair tissue in second-look and third-look biopsies from patients treated with engineered cartilage: Relationship to symptomatology and time after implantation. *Arthritis Research and Therapy* **10**, R132 (2008).
8. Moon, J.J. & West, J.L. Vascularization of engineered tissues: Approaches to promote angiogenesis in biomaterials. *Curr. Top. Med. Chem.* **8**, 300-310 (2008).
9. Gerhardt, H. & Betsholtz, C. How do endothelial cells orientate? *Mechanisms of Angiogenesis* (2005).
10. Bergers, G. Pericytes, the Mural Cells of the Microvascular System. *Angiogenesis An Integrative Approach from Science to Medicine* 45-55 (2008).
11. Shepro, D. & Morel, N.M.L. Pericyte Physiology. *Faseb Journal* **7**, 1031-1038 (1993).
12. Schmidt, A., Brixius, K. & Bloch, W. Endothelial precursor cell migration during vasculogenesis. *Circulation Research* **101**, 125-136 (2007).

13. Guedez, L. & Stetler-Stevenson, W.G. Matrix Metalloproteinases and Their Endogenous Inhibitors. *Angiogenesis An Integrative Approach From Science to Medicine* 55-63 (2008).
14. Iruela-Arispe, L. Endothelial Cell Activation. *Angiogenesis An Integrative Approach from Science to Medicine* 55-63 (2008).
15. Karamysheva, A.F. Mechanisms of angiogenesis. *Biochemistry-Moscow* **73**, 751-762 (2008).
16. Kamei, M. *et al.* Endothelial tubes assemble from intracellular vacuoles in vivo. *Nature* **442**, 453-456 (2006).
17. Adams, R.H. & Alitalo, K. Molecular regulation of angiogenesis and lymphangiogenesis. *Nature Reviews Molecular Cell Biology* **8**, 464-478 (2007).
18. Shibuya, M. Vascular Permeability/Vascular Endothelial Growth Factor. *Angiogenesis An Integrative Approach From Science to Medicine* 89-95 (2008).
19. Wise, L.M. *et al.* Vascular endothelial growth factor (VEGF)-like protein from orf virus NZ2 binds to VEGFR2 and neuropilin-1. *Proceedings of the National Academy of Sciences of the United States of America* **96**, 3071-3076 (1999).
20. Fong, G.-H., Rossant, J., Gertsenstein, M. & Breitman, M.L. Role of the Flt-1 receptor tyrosine kinase in regulating the assembly of vascular endothelium. *Nature* **376**, 66-70 (1995).
21. Gerhardt, H. *et al.* VEGF guides angiogenic sprouting utilizing endothelial tip cell filopodia. *Journal of Cell Biology* **161**, 1163-1177 (2003).
22. Murai, K.K. & Pasquale, E.B. `Eph`ective signaling: forward, reverse and crosstalk. *J Cell Sci* **116**, 2823-2832 (2003).
23. Brantley, D.M. *et al.* Soluble Eph A receptors inhibit tumor angiogenesis and progression in vivo. *Oncogene* **21**, 7011-7026 (2002).
24. Presta, M., Mitola, S., Dell'Era, P., Leali, D. & Nicoli, S. Fibroblast Growth Factor-2 in Angiogenesis. *Angiogenesis An Integrative Approach From Science to Medicine* 77-89 (2008).
25. Maisonpierre, P.C. *et al.* Angiopoietin-2, a Natural Antagonist for Tie2 That Disrupts in vivo Angiogenesis. *Science* **277**, 55-60 (1997).

26. Kazlauskas, A. Platelet-Derived Growth Factor. *Angiogenesis An Integrative Approach from Science to Medicine* 99-113 (2008).
27. Sato, Y. & Rifkin, D.B. Inhibition of endothelial cell movement by pericytes and smooth muscle cells: activation of a latent transforming growth factor-beta 1-like molecule by plasmin during co-culture. *The Journal of Cell Biology* **109**, 309-315 (1989).
28. Moon, J.J. *et al.* Biomimetic hydrogels with pro-angiogenic properties. *Biomaterials* **31**, 3840-3847 (2010).
29. Koike, N. *et al.* Creation of long-lasting blood vessels. *Nature* **428**, 138-139 (2004).
30. Mammoto, A. *et al.* A mechanosensitive transcriptional mechanism that controls angiogenesis. *Nature* **457**, 1103-U57 (2009).
31. Young, P.P., Vaughan, D.E. & Hatzopoulos, A.K. Biologic Properties of Endothelial Progenitor Cells and Their Potential for Cell Therapy. *Progress in Cardiovascular Diseases* **49**, 421-429 (2007).
32. Melero-Martin, J.M. *et al.* Engineering robust and functional vascular networks in vivo with human adult and cord blood-derived progenitor cells. *Circulation Research* **103**, 194-202 (2008).
33. Lokmic, Z. & Mitchell, G.M. Engineering the microcirculation. *Tissue Engineering Part B-Reviews* **14**, 87-103 (2008).
34. Twardowski, T., Fertala, A., Orgel, J. & Antonio, J.D.S. Type I collagen and collagen mimetics as angiogenesis promoting superpolymers. *Current Pharmaceutical Design* **13**, 3608-3621 (2007).
35. Davis, G.E. & Camarillo, C.W. An alpha 2 beta 1 integrin-dependent pinocytic mechanism involving intracellular vacuole formation and coalescence regulates capillary lumen and tube formation in three-dimensional collagen matrix. *Experimental Cell Research* **224**, 39-51 (1996).
36. Koch, S. *et al.* Enhancing angiogenesis in collagen matrices by covalent incorporation of VEGF. *J. Mater. Sci. - Mater. Med.* **17**, 735-741 (2006).

37. Chalupowicz, D.G., Chowdhury, Z.A., Bach, T.L., Barsigian, C. & Martinez, J. Fibrin-II Induces Endothelial-Cell Capillary-Tube Formation. *Journal of Cell Biology* **130**, 207-215 (1995).
38. Montano, I. *et al.* Formation of Human Capillaries In Vitro: The Engineering of Prevascularized Matrices. *Tissue Engineering Part A* **16**, 269-282 (2010).
39. Arnaoutova, I. & Kleinman, H.K. In vitro angiogenesis: endothelial cell tube formation on gelled basement membrane extract. *Nat. Protoc.* **5**, 628-635 (2010).
40. Shin, M. *et al.* Endothelialized Networks with a Vascular Geometry in Microfabricated Poly(dimethyl siloxane). *Biomedical Microdevices* **6**, 269-278 (2004).
41. Bianchi, F. *et al.* Microfabrication of fractal polymeric structures for capillary morphogenesis: Applications in therapeutic angiogenesis and in the engineering of vascularized tissue. *Journal of Biomedical Materials Research Part B-Applied Biomaterials* **81B**, 462-468 (2007).
42. Lavik, E. & Langer, R. Tissue engineering: current state and perspectives. *Applied Microbiology and Biotechnology* **65**, 1-8 (2004).
43. Fournier, N. & Doillon, C.J. Biological molecule-impregnated polyester: An in vivo angiogenesis study. *Biomaterials* **17**, 1659-1665 (1996).
44. Zisch, A.H. *et al.* Cell-demanded release of VEGF from synthetic, biointeractive cell-ingrowth matrices for vascularized tissue growth. *Faseb Journal* **17**, 2260-2262 (2003).
45. DeForest, C.A., Polizzotti, B.D. & Anseth, K.S. Sequential click reactions for synthesizing and patterning three-dimensional cell microenvironments. *Nature Materials* **8**, 659-664 (2009).
46. Moon, J.J., Lee, S.H., Hahn, M.S., Nsiah, B.A. & West, J.L. Regulation of endothelial angiogenesis and vasculogenesis in synthetic poly(ethylene glycol) hydrogels modified with biomolecules. *Faseb Journal* **21**, A748-A749 (2007).
47. Leslie-Barbick, J.E., Moon, J.J. & West, J.L. Covalently-Immobilized Vascular Endothelial Growth Factor Promotes Endothelial Cell Tubulogenesis in Poly(ethylene glycol) Diacrylate Hydrogels. *J. Biomater. Sci., Polym. Ed.* **20**, 1763-1779 (2009).

48. Moon, J.J., Lee, S.H. & West, J.L. Synthetic biomimetic hydrogels incorporated with Ephrin-A1 for therapeutic angiogenesis. *Biomacromolecules* **8**, 42-49 (2007).
49. Shoichet, M.S. & Kapur, T.A. Immobilized concentration gradients of nerve growth factor guide neurite outgrowth. *Journal of Biomedical Materials Research Part A* **68A**, 235-243 (2004).
50. Shin, H., Zygourakis, K., Farach-Carson, M., Yaszemski, M.J. & Mikos, A.G. Modulation of differentiation and mineralization of marrow stromal cells cultured on biomimetic hydrogels modified with Arg-Gly-Asp containing peptides. *Journal of Biomedical Materials Research Part A* **69A**, 535-543 (2004).
51. Khademhosseini, A. & Langer, R. Microengineered hydrogels for tissue engineering. *Biomaterials* **28**, 5087-5092 (2007).
52. Nguyen, K.T. & West, J.L. Photopolymerizable hydrogels for tissue engineering applications. *Biomaterials* **23**, 4307-4314 (2002).
53. Bryant, S.J. & Anseth, K.S. Photopolymerization of Hydrogel Scaffolds. *Scaffolding in Tissue Engineering* 71-91 (2006).
54. Burdick, J.A. & Anseth, K.S. Photoencapsulation of osteoblasts in injectable RGD-modified PEG hydrogels for bone tissue engineering. *Biomaterials* **23**, 4315-4323 (2002).
55. Suggs, L.J. & Mikos, A.G. Development of poly(propylene fumarate-co-ethylene glycol) as an injectable carrier for endothelial cells. *Cell Transplantation* **8**, 345-350 (1999).
56. Ifkovits, J.L. & Burdick, J.A. Review: Photopolymerizable and degradable biomaterials for tissue engineering applications. *Tissue Eng.* **13**, 2369-2385 (2007).
57. Lee, S.H., Moon, J.J., Miller, J.S. & West, J.L. Poly(ethylene glycol) hydrogels conjugated with a collagenase-sensitive fluorogenic substrate to visualize collagenase activity during three-dimensional cell migration. *Biomaterials* **28**, 3163-3170 (2007).
58. Lee, S.-H., Moon, J.J. & West, J.L. Three-dimensional micropatterning of bioactive hydrogels via two-photon laser scanning photolithography for guided 3D cell migration. *Biomaterials* **29**, 2962-2968 (2008).

59. Hahn, M.S. *et al.* Photolithographic patterning of polyethylene glycol hydrogels. *Biomaterials* **27**, 2519-2524 (2006).
60. Miller, J.S., Béthencourt, M.I., Hahn, M., Lee, T.R. & West, J.L. Laser-scanning lithography (LSL) for the soft lithographic patterning of cell-adhesive self-assembled monolayers. *Biotechnology and Bioengineering* **93**, 1060-1068 (2006).
61. Gobin, A.S. & West, J.L. Cell migration through defined, synthetic ECM analogs. *FASEB J.* **16**, 751-753 (2002).
62. Gobin, A.S. & West, J.L. Val-ala-pro-gly, an elastin-derived non-integrin ligand: Smooth muscle cell adhesion and specificity. *Journal of Biomedical Materials Research Part A* **67A**, 255-259 (2003).
63. Jun, H.W. & West, J. Development of a YIGSR-peptide-modified polyurethaneurea to enhance endothelialization. *Journal of Biomaterials Science, Polymer Edition* **15**, 73-94 (2004).
64. Chen, C.S., Alonso, J.L., Ostuni, E., Whitesides, G.M. & Ingber, D.E. Cell shape provides global control of focal adhesion assembly. *Biochemical and Biophysical Research Communications* **307**, 355-361 (2003).
65. Moon, J.J., Hahn, M.S., Kim, I., Nsiah, B.A. & West, J.L. Micropatterning of poly(ethylene glycol) diacrylate hydrogels with biomolecules to regulate and guide endothelial morphogenesis. *Tissue Eng Part A* **15**, 579-585 (2009).
66. Griffith, L.G. & Swartz, M.A. Capturing complex 3D tissue physiology in vitro. *Nat Rev Mol Cell Biol* **7**, 211-224 (2006).
67. Zamir, E. *et al.* Molecular diversity of cell-matrix adhesions. *J Cell Sci* **112**, 1655-1669 (1999).
68. Cukierman, E., Pankov, R., Stevens, D.R. & Yamada, K.M. Taking cell-matrix adhesions to the third dimension. *Science* **294**, 1708-1712 (2001).
69. Zaman, M.H. *et al.* Migration of tumor cells in 3D matrices is governed by matrix stiffness along with cell-matrix adhesion and proteolysis. *Proceedings of the National Academy of Sciences of the United States of America* **103**, 10889-10894 (2006).

70. Dikovsky, D., Bianco-Peled, H. & Seliktar, D. Defining the Role of Matrix Compliance and Proteolysis in Three-Dimensional Cell Spreading and Remodeling. *Biophysical Journal* **94**, 2914-2925 (2008).
71. Chu, T.-M.G. Solid Freeform Fabrication of Tissue Engineering Scaffolds. *Scaffolds in Tissue Engineering* 139-155 (2006).
72. Sherwood, J.K. *et al.* A three-dimensional osteochondral composite scaffold for articular cartilage repair. *Biomaterials* **23**, 4739-4751 (2002).
73. Lewis, J.A. & Gratson, G.M. Direct writing in three dimensions. *Materials Today* **7**, 32-39 (2004).
74. Chang, C.C., Boland, E.D., Williams, S.K. & Hoying, J.B. Direct-write bioprinting three-dimensional biohybrid systems for future regenerative therapies. *Journal of Biomedical Materials Research Part B-Applied Biomaterials* **98B**, 160-170 (2011).
75. Smith, C.M. *et al.* Three-dimensional bioassembly tool for generating viable tissue-engineered constructs. *Tissue Engineering* **10**, 1566-1576 (2004).
76. Lee, W. *et al.* On-demand three-dimensional freeform fabrication of multi-layered hydrogel scaffold with fluidic channels. *Biotechnol Bioeng* **105**, 1178-1186 (2010).
77. Norotte, C., Marga, F.S., Niklason, L.E. & Forgacs, G. Scaffold-free vascular tissue engineering using bioprinting. *Biomaterials* **30**, 5910-5917 (2009).
78. Cohen, D.L., Malone, E., Lipson, H. & Bonassar, L.J. Direct freeform fabrication of seeded hydrogels in arbitrary geometries. *Tissue Engineering* **12**, 1325-1335 (2006).
79. Fedorovich, N.E., Wijnberg, H.M., Dhert, W.J.A. & Alblas, J. Distinct tissue formation by heterogeneous printing of osteo-and endothelial progenitor cells. *Tissue Engineering - Part A* **17**, 2113-2121 (2011).
80. Skardal, A. *et al.* Photocrosslinkable Hyaluronan-Gelatin Hydrogels for Two-Step Bioprinting. *Tissue Engineering Part A* **16**, 2675-2685 (2010).
81. Censi, R. *et al.* A Printable Photopolymerizable Thermosensitive p(HPMAm-lactate)-PEG Hydrogel for Tissue Engineering. *Advanced Functional Materials* **21**, 1833-1842 (2011).

82. Smith, C.M., Christian, J.J., Warren, W.L. & Williams, S.K. Characterizing environmental factors that impact the viability of tissue-engineered constructs fabricated by a direct-write bioassembly tool. *Tissue Engineering* **13**, 373-383 (2007).
83. Ringeisen, B.R., Othon, C.M., Barron, J.A., Young, D. & Spargo, B.J. Jet-based methods to print living cells. *Biotechnology Journal* **1**, 930-948 (2006).
84. Wüst, S., Müller, R. & Hofmann, S. Controlled Positioning of Cells in Biomaterials—Approaches Towards 3D Tissue Printing. *Journal of Functional Biomaterials* **2**, 119-154 (2011).
85. Pepper, M.E. *et al.* Design and implementation of a two-dimensional inkjet bioprinter. *2009 Annual International Conference of the IEEE Engineering in Medicine and Biology Society* 6001-6005 (2009).doi:10.1109/IEMBS.2009.5332513
86. Xu, T., Jin, J., Gregory, C., Hickman, J.J. & Boland, T. Inkjet printing of viable mammalian cells. *Biomaterials* **26**, 93-99 (2005).
87. Cui, X. & Boland, T. Human microvasculature fabrication using thermal inkjet printing technology. *Biomaterials* **30**, 6221-6227 (2009).
88. Pataky, K. *et al.* Microdrop printing of hydrogel bioinks into 3D tissue-like geometries. *Advanced Materials* **24**, 391-396 (2012).
89. Barron, J.A. *et al.* Printing of protein microarrays via a capillary-free fluid jetting mechanism. *PROTEOMICS* **5**, 4138-4144 (2005).
90. Barron, J.A., Wu, P., Ladouceur, H.D. & Ringeisen, B.R. Biological laser printing: A novel technique for creating heterogeneous 3-dimensional cell patterns. *Biomedical Microdevices* **6**, 139-147 (2004).
91. Barron, J.A., Krizman, D.B. & Ringeisen, B.R. Laser printing of single cells: Statistical analysis, cell viability, and stress. *Annals of Biomedical Engineering* **33**, 121-130 (2005).
92. Hopp, B. *et al.* Survival and proliferative ability of various living cell types after laser-induced forward transfer. *Tissue Engineering* **11**, 1817-1823 (2005).
93. Guillemot, F. *et al.* High-throughput laser printing of cells and biomaterials for tissue engineering. *Acta Biomaterialia* **6**, 2494-2500 (2009).

94. Guillotin, B. *et al.* Laser assisted bioprinting of engineered tissue with high cell density and microscale organization. *Biomaterials* **31**, 7250-7256 (2010).
95. Pirlo, R.K., Wu, P., Liu, J. & Ringeisen, B. PLGA/hydrogel biopapers as a stackable substrate for printing HUVEC networks via BioLP (TM). *Biotechnology and Bioengineering* **109**, 262-273 (2011).
96. Bryant, S.J., Cuy, J.L., Hauch, K.D. & Ratner, B.D. Photo-patterning of porous hydrogels for tissue engineering. *Biomaterials* **28**, 2978-2986 (2007).
97. Papavasiliou, G. *et al.* Three-dimensional patterning of poly(ethylene glycol) hydrogels through surface-initiated photopolymerization. *Tissue Engineering Part C-Methods* **14**, 129-140 (2008).
98. Tsang, V.L. *et al.* Fabrication of 3D hepatic tissues by additive photopatterning of cellular hydrogels. *FASEB J.* **21**, 790-801 (2007).
99. Khetan, S. & Burdick, J.A. Patterning hydrogels in three dimensions towards controlling cellular interactions. *Soft Matter* **7**, 830-838 (2010).
100. Chan, V., Zorlutuna, P., Jeong, J.H., Kong, H. & Bashir, R. Three-dimensional photopatterning of hydrogels using stereolithography for long-term cell encapsulation. *Lab on a Chip* **10**, 2062-2070 (2010).
101. Khademhosseini, A., Langer, R., Borenstein, J. & Vacanti, J.P. Microscale technologies for tissue engineering and biology. *Proc. Natl. Acad. Sci.* **103**, 2480-2487 (2006).
102. Tan, W. & Desai, T.A. Microscale multilayer cocultures for biomimetic blood vessels. *Journal of Biomedical Materials Research Part A* **72A**, 146-160 (2005).
103. Wong, A.P., Perez-Castillejos, R., Love, J.C. & Whitesides, G.M. Partitioning microfluidic channels with hydrogel to construct tunable 3-D cellular microenvironments. *Biomaterials* **29**, 1853-1861 (2008).
104. Cheung, Y.K., Gillette, B.M., Zhong, M., Ramcharan, S. & Sia, S.K. Direct patterning of composite biocompatible microstructures using microfluidics. *Lab on a Chip* **7**, 574-579 (2007).
105. Luo, Y. & Shoichet, M.S. A photolabile hydrogel for guided three-dimensional cell growth and migration. *Nature Materials* **3**, 249-253 (2004).

106. Luo, Y. & Shoichet, M.S. A photolabile hydrogel for guided three-dimensional cell growth and migration. *Nature materials* **3**, 249-53 (2004).
107. Shotton, D.M. Confocal scanning optical microscopy and its applications for biological specimens. *J Cell Sci* **94**, 175-206 (1989).
108. Hahn, M.S., Miller, J.S. & West, J.L. Laser Scanning Lithography for Surface Micropatterning on Hydrogels. *Advanced Materials* **17**, 2939-2942 (2005).
109. Soeller, C. & Cannell, M.B. Two-photon microscopy: Imaging in scattering samples and three-dimensionally resolved flash photolysis. *Microscopy Research and Technique* **47**, 182-195 (1999).
110. Denk, W., Strickler, J.H. & Webb, W.W. Two-photon laser scanning fluorescence microscopy. *Science* **248**, 73-76 (1990).
111. Langer, R. & Tirrell, D.A. Designing materials for biology and medicine. *Nature* **428**, 487-492 (2004).
112. Slaughter, B.V., Khurshid, S.S., Fisher, O.Z., Khademhosseini, A. & Peppas, N.A. Hydrogels in Regenerative Medicine. *Advanced Materials* **21**, 3307-3329 (2009).
113. Hahn, M.S., Miller, J.S. & West, J.L. Three-dimensional biochemical and biomechanical patterning of hydrogels for guiding cell behavior. *Adv. Mater.* **18**, 2679-2684 (2006).
114. Saik, J.E. Bioactive Poly(ethylene glycol)-based Hydrogels for Angiogenesis in Tissue Engineering. (2011).
115. Hoffmann, J.C. & West, J.L. Three-dimensional photolithographic patterning of multiple bioactive ligands in poly(ethylene glycol) hydrogels. *Soft Matter* **6**, 5056-5063 (2010).
116. Wosnick, J.H. & Shoichet, M.S. Three-dimensional chemical Patterning of transparent hydrogels. *Chemistry of Materials* **20**, 55-60 (2008).
117. Wylie, R.G. & Shoichet, M.S. Two-photon micropatterning of amines within an agarose hydrogel. *Journal of Materials Chemistry* **18**, 2716-2721 (2008).
118. Seidlits, S.K., Schmidt, C.E. & Shear, J.B. High-Resolution Patterning of Hydrogels in Three Dimensions using Direct-Write Photofabrication for Cell Guidance. *Advanced Functional Materials* **19**, 3543-3551 (2009).

119. Komoriya, A. *et al.* The Minimal Essential Sequence for a Major Cell Type-Specific Adhesion Site (Cs1) within the Alternatively Spliced Type-III Connecting Segment Domain of Fibronectin is Leucine-Aspartic Acid-Valine. *Journal of Biological Chemistry* **266**, 15075-15079 (1991).
120. Liu, L.Y., Ratner, B.D., Sage, E.H. & Jiang, S.Y. Endothelial cell migration on surface-density gradients of fibronectin, VEGF, or both proteins. *Langmuir* **23**, 11168-11173 (2007).
121. Cao, R.H. *et al.* Angiogenic synergism, vascular stability and improvement of hind-limb ischemia by a combination of PDGF-BB and FGF-2. *Nature Medicine* **9**, 604-613 (2003).
122. Wylie, R.G. *et al.* Spatially controlled simultaneous patterning of multiple growth factors in three-dimensional hydrogels. *Nature Materials* **10**, 799-806 (2011).
123. Aizawa, Y., Wylie, R. & Shoichet, M. Endothelial Cell Guidance in 3D Patterned Scaffolds. *Adv. Mater.* (2010).at <<http://dx.doi.org/10.1002/adma.201001855>>
124. Kim, H.-D. & Peyton, S.R. Bio-inspired materials for parsing matrix physicochemical control of cell migration: A Review. *Integrative Biology* **4**, 37 (2012).
125. Mierke, C.T., Rösel, D., Fabry, B. & Brábek, J. Contractile forces in tumor cell migration. *European journal of cell biology* **87**, 669-76 (2008).
126. Lauffenburger, D.A. & Horwitz, A.F. Cell migration: a physically integrated molecular process. *Cell* **84**, 359-69 (1996).
127. Palecek, S.P., Loftus, J.C., Ginsberg, M.H., Lauffenburger, D.A. & Horwitz, A.F. Integrin-ligand binding properties govern cell migration speed through cell-substratum adhesiveness. *Nature* **385**, 537-40 (1997).
128. Peyton, S.R. & Putnam, A.J. Extracellular matrix rigidity governs smooth muscle cell motility in a biphasic fashion. *Journal of cellular physiology* **204**, 198-209 (2005).
129. Gobin, A.S. & West, J.L. Cell migration through defined, synthetic ECM analogs. *FASEB journal : official publication of the Federation of American Societies for Experimental Biology* **16**, 751-3 (2002).

130. Mann, B.K. & West, J.L. Cell adhesion peptides alter smooth muscle cell adhesion, proliferation, migration, and matrix protein synthesis on modified surfaces and in polymer scaffolds. *Journal of biomedical materials research* **60**, 86-93 (2002).
131. Tayalia, P., Mendonca, C.R., Baldacchini, T., Mooney, D.J. & Mazur, E. 3D Cell-Migration Studies using Two-Photon Engineered Polymer Scaffolds. *Advanced Materials* **20**, 4494-4498 (2008).
132. Schwartz, M.P. *et al.* A synthetic strategy for mimicking the extracellular matrix provides new insight about tumor cell migration. *Integrative biology : quantitative biosciences from nano to macro* **2**, 32-40 (2010).
133. Wolf, K. *et al.* Compensation mechanism in tumor cell migration: mesenchymal-amoeboid transition after blocking of pericellular proteolysis. *The Journal of cell biology* **160**, 267-77 (2003).
134. Gill, B.J. *et al.* A biomimetic synthetic matrix with independently tunable biochemistry and mechanical properties to study epithelial morphogenesis and EMT in a lung adenocarcinoma model. *Cancer Research In Review*, (2012).
135. McHale, M.K. Thesis. (2008).
136. Wacker, B.K. *et al.* Endothelial cell migration on RGD-peptide-containing PEG hydrogels in the presence of sphingosine 1-phosphate. *Biophysical journal* **94**, 273-85 (2008).
137. Zaman, M.H., Matsudaira, P. & Lauffenburger, D.A. Understanding effects of matrix protease and matrix organization on directional persistence and translational speed in three-dimensional cell migration. *Annals of Biomedical Engineering* **35**, 91-100 (2007).
138. Kim, H.-D. *et al.* Epidermal growth factor-induced enhancement of glioblastoma cell migration in 3D arises from an intrinsic increase in speed but an extrinsic matrix- and proteolysis-dependent increase in persistence. *Molecular biology of the cell* **19**, 4249-59 (2008).
139. Saik, J.E., Gould, D.J., Watkins, E.M., Dickinson, M.E. & West, J.L. Covalently immobilized platelet-derived growth factor-BB promotes angiogenesis in biomimetic poly(ethylene glycol) hydrogels. *Acta Biomater.* (2010).doi:10.1016/j.actbio.2010.08.018

140. DeLong, S.A., Moon, J.J. & West, J.L. Covalently immobilized gradients of bFGF on hydrogel scaffolds for directed cell migration . *Biomaterials* **26**, 3227-3234 (2005).
141. Cuchiara, M.P. Microfabricated Poy (ethylene glycol) Hydrogels for Microvascular Tissue Engineering Applications. *Thesis* (2011).
142. Shen, Q. *et al.* Adult SVZ stem cells lie in a vascular niche: a quantitative analysis of niche cell-cell interactions. *Cell stem cell* **3**, 289-300 (2008).
143. Tavazoie, M. *et al.* A specialized vascular niche for adult neural stem cells. *Cell stem cell* **3**, 279-88 (2008).
144. Yokomizo, T. & Dzierzak, E. Three-dimensional cartography of hematopoietic clusters in the vasculature of whole mouse embryos. *Development (Cambridge, England)* **137**, 3651-61 (2010).
145. Anderson, J.R. *et al.* Exploring the retinal connectome. (2011).at <<http://www.molvis.org/molvis/v17/a41/>>
146. Gunn, J.W., Turner, S.D. & Mann, B.K. Adhesive and mechanical properties of hydrogels influence neurite extension. *Journal of biomedical materials research. Part A* **72**, 91-7 (2005).
147. Liu Tsang, V. *et al.* Fabrication of 3D hepatic tissues by additive photopatterning of cellular hydrogels. *FASEB journal : official publication of the Federation of American Societies for Experimental Biology* **21**, 790-801 (2007).
148. Geraets, W.G.M., van Daatselaar, A.N. & Verheij, J.G.C. An efficient filling algorithm for counting regions. *Computer methods and programs in biomedicine* **76**, 1-11 (2004).
149. Bolte, S. & Cordelières, F.P. A guided tour into subcellular colocalization analysis in light microscopy. *Journal of microscopy* **224**, 213-32 (2006).
150. West, J.L. & Hubbell, J.A. Polymeric Biomaterials with Degradation Sites for Proteases Involved in Cell Migration. *Macromolecules* **32**, 241-244 (1999).
151. Oheim, M., Michael, D.J., Geisbauer, M., Madsen, D. & Chow, R.H. Principles of two-photon excitation fluorescence microscopy and other nonlinear imaging approaches. *Advanced drug delivery reviews* **58**, 788-808 (2006).

152. Shen, Q. *et al.* Endothelial cells stimulate self-renewal and expand neurogenesis of neural stem cells. *Science* **304**, 1338-40 (2004).
153. Kazanis, I. *et al.* Quiescence and activation of stem and precursor cell populations in the subependymal zone of the mammalian brain are associated with distinct cellular and extracellular matrix signals. *The Journal of neuroscience : the official journal of the Society for Neuroscience* **30**, 9771-81 (2010).
154. Mirzadeh in JoVE. at <<http://www.jove.com/search?q=Mirzadeh>>
155. DeForest, C.A. & Anseth, K.S. Cytocompatible click-based hydrogels with dynamically tunable properties through orthogonal photoconjugation and photocleavage reactions. *Nat Chem* **3**, 925-931 (2011).
156. Chen, Y.-C. *et al.* Functional Human Vascular Network Generated in Photocrosslinkable Gelatin Methacrylate Hydrogels. *Advanced Functional Materials* n/a-n/a (2012).doi:10.1002/adfm.201101662
157. Ovsianikov, A. *et al.* Laser Fabrication of Three-Dimensional CAD Scaffolds from Photosensitive Gelatin for Applications in Tissue Engineering. *Biomacromolecules* **12**, 851-858 (2011).

Chapter 7: Appendix

7.1 Description of Custom MATLAB Scripts

The complete lines of code for the custom written MATLAB scripts used in image guided TP-LSL (Chapter 4) have been included. These scripts produce overlay files that can be utilized by a Zeiss laser scanning microscope to guide photolithography based on an input image. Comments are denoted by lines starting with “%” and are included throughout the code in order to describe requirements for input arguments and to explain important parts of the algorithm. The main program is “vesselmosaic2.m”; the other programs, “segment.m” and “roifiles2.m,” are subroutines used by “vesselmosaic2.m.” Note that the subroutine “segment.m” is a modification of a published segmentation algorithm¹⁴⁸.

7.2 Custom MATLAB Scripts

```
function output =
vesselmosaic2(raw, pixlength, xres, film, innum1, innum2, innum3, innum4)
%
% vesselmosaic2.m
%
% Copyright 2009-2011,
% Baylor College of Medicine and Rice University,
% All Rights Reserved
%
% ***Main program; run at the command prompt
%
% Reconstructs a binary image using a mosaic of quadrilateral ROIs to
% guide LSM photolithography.
%
% Two files are created in the working directory. The first file
% JCCxxxx.rls is an overlay file that defines a list of regions of
% interest (ROIs) in a format that is readable by Zeiss AIM or Zen
% software. By default, the overlay file is created with a .rls
% extension, which is the extension used by the AIM software. For use
% with the Zen software, simply change the file extension to .ovl
%
% The second file ROIxxxx.tif is a rendering of the ROIs in tif format.
% This is for making qualitative comparisons between the generated ROIs
% and the original image, but is not intended for quantitative
% comparisons.
```

```

%
% .rls files must be placed into the folder C:\AIM\ROIS
% .ovl files must be loaded using the Zen GUI
%
% Input arguments:
% raw = Matrix of integers, all either 0 or 1, describing the
% binary image to be used for image guided patterning
% pixlength = Physical length of a single pixel, in micrometers
% xres = Desired maximum width of an ROI, in pixels. Must be an
% integer > 1
% filnm = Name and path of a template .rls file. This file must be
% a .rls file defining a list of Polyline ROIs
% innum1 = First digit in file identifier number
% innum2 = Second digit in file identifier number
% innum3 = Third digit in file identifier number
% innum4 = Fourth digit in file identifier number
%
% Notes:
% - file identifier number is an arbitrary tag for distinguishing
between
% different overlay files
%Set variables based on input arguments
strinnum1=int2str(innum1);
strinnum2=int2str(innum2);
strinnum3=int2str(innum3);
strinnum4=int2str(innum4);
currdir=cd;
dirr=cd;
a=raw;
%Display original image for reference
figure('Position',[1 1 659 659]);
imagesc(a);colormap(gray);
set(gca,'DataAspectRatio',[1 1 1]);
temp=size(a);
ysize=temp(1);
xsize=temp(2);
b=a;
%Divide input image into two interleaved images before segmentation.
This
%essentially divides large regions into smaller, simpler regions
for i=1:(2*xres):xsize
b(:,i:(i+xres-1))=0;
end
b=b(1:ysize,1:xsize);
if (xsize-i)>xres
b(:,(xsize-xres+1):xsize)=0;
end
c=(1-b);
d=c.*a;
%Pass each of the two interleaved images to the subroutine segment.m to
%identify and count each interconnected region
e=segment(b);
f=segment(d);
g=e(:, :, 1).*b;
h=f(:, :, 1).*d;
%Initialize matrix of coordinates
splinx=[0 0 0 0];

```

```

spliney=[0 0 0 0];
splinenum=1;
%Approximate each segmented region into a vertically simple
quadrilateral.
%Begin with the first of the two interleaved images.
%Display cumulative progress as a percentage
for i=1:(max(max(g)))
DefiningROIs=100*i/(max(max(g)))
if sum(sum(g==i))==0
continue
end
curr=g==i;
[row col]=find(curr==1);
%Define left and right limits of quadrilateral
lx=min(col);
rx=max(col);
%Define upper and lower limits of quadrilateral at each x-limit
[row col]=find(curr(:,lx)==1);
uly=min(row);
lly=max(row);
if uly==lly
lly=lly+1;
end
[row col]=find(curr(:,rx)==1);
ury=min(row);
lry=max(row);
if ury==lry
lry=lry+1;
end
%Store the coordinates of these vertices into splineX and spliney
splineX(splinenum,:)= [lx rx rx lx];
spliney(splinenum,:)= [uly ury lry lly];
splinenum=splinenum+1;
%Go to the next region and repeat
end
%Now, repeat the above process for the second of the two interleaved
images
for i=1:(max(max(h)))
DefiningROIs2=100*i/(max(max(h)))
if sum(sum(h==i))==0
continue
end
curr=h==i;
[row col]=find(curr==1);
lx=min(col);
rx=max(col);
[row col]=find(curr(:,lx)==1);
uly=min(row);
lly=max(row);
if uly==lly
lly=lly+1;
end
[row col]=find(curr(:,rx)==1);
ury=min(row);
lry=max(row);
if ury==lry
lry=lry+1;
end

```



```

end
splinex(splinenum,:)= [lx rx rx lx];
spliney(splinenum,:)= [uly ury lry lly];
splinenum=splinenum+1;
end
%Here, the program pauses - to continue, type "return" at the command
%prompt
keyboard
%MATLAB is used to create a rendering of the ROIs. This is for making
%qualitative comparisons between the generated ROIs and the original
image,
%but is not intended for quantitative comparisons.
j=a.*0;
temp=size(splines);
for i=1:temp(1)
PlottingROIs=100*i/temp(1)
BW=roipoly(a, (splines(i,:)+[-1 0 0 -1]), (spliney(i,:)+[0 0 -1 -1]));
j=j+BW;
end
j=j>0;
figure('Position',[1 1 659 659]);
imagesc(j);colormap(gray);
set(gca,'DataAspectRatio',[1 1 1])
%Rendering is saved in the working directory as 'ROIxxxx.tif'
temp=strcat('ROI',strinum1,strinum2,strinum3,strinum4,'.tif');
imwrite(j,temp,'tif');
%Convert pixel coordinates into real coordinates in units of
micrometers by
%scaling with pixlength
splinesxtrans=pixlength.*splines;
splinesytrans=pixlength.*spliney;
%Convert into the coordinate system used by the microscope. Coordinate
%system is in units of meters, with the origin at the center of the
field
%of view.
splinesxtrans=((splinesxtrans-(xsize*pixlength/2))*(10^-6));
splinesytrans=((splinesytrans-(ysize*pixlength/2))*(10^-6));
%Define path and file name for .rls file
film2=strcat(dirr,'/','JCC',strinum1,strinum2,strinum3,strinum4,'.
rls');
tempsizee=size(splinesxtrans);
drawnumber=tempsizee(1);
%Pass the coordinates for the vertices of each ROI to the subroutine
%roifiles2.m which will write the information about the list of ROIs to
a
%file written in a format that is readable by Zeiss AIM or Zen software
roifiles2(film,film2,strinum1,strinum2,strinum3,strinum4,drawnumb
er,splinesxtrans,
splinesytrans);
cd(currdir);
%Some of the important variables are included in the output for further
use
%at the command prompt, if necessary.
output.original=a;
output.roi=j;
output.splines=splines;
output.spliney=spliney;

```

```

output.splinxtrans=splinxtrans;
output.splineytrans=splineytrans;
%End of program

function output = segment(raw)
%
% segment.m
%
% Copyright 2009-2011,
% Baylor College of Medicine and Rice University,
% All Rights Reserved
%
% ***Subroutine for vesselmosaic.m
%
% Segments an image into regions based on connectivity of points with
the
% same value. Based on an algorithm described by Geraets et. al.,
Computer
% Methods and Programs in Biomedicine (2004) 76, 1-11, "An efficient
% filling algorithm for counting regions." Variable names and program
% structure are similar, but code is rewritten for MATLAB, restructured
so
% that it doesn't use GOTO statements, and modified to add labeling
% functionality, as stored in the PaintbyNo variable.
%
% Input arguments:
% raw = matrix of integers, all either 0 or 1, describing the binary
% image to be segmented into connected regions
%
%Initialize variables
bSeed = int32(0);
KX = int32(0);
lWidth = int32(0);
XSeed = int32(0);
XCursor = int32(0);
XRight = int32(0);
LY = int32(0);
lHeight = int32(0);
YSeed = int32(0);
YCursor = int32(0);
YUpper = int32(0);
iBlacks = int32(0);
iWhites = int32(0);
iTotal = int32(0);
Sze=size(raw);
lHeight=Sze(1);
lWidth = Sze(2);
TotProg=lHeight*lWidth
%Notepad is the matrix keeping track of which pixels have already been
%assigned to a segment.
%
%PaintbyNo is the matrix keeping track of which segment each pixel is
%assigned to.
Notepad=0*raw;
PaintbyNo=0*raw;
%Outer loop; done until every pixel has been assigned a segment.
while (all(all(Notepad)))~=1;

```

```

%Progress is calculated and displayed as a percentage
Prog=100*(sum(sum(Notepad)))/TotProg
%This loop finds the next pixel which is not yet assigned a segment.
for XSeed=1:lWidth;
for YSeed=1:lHeight;
if Notepad(YSeed,XSeed)==0;
break;
end;
end;
if Notepad(YSeed,XSeed)==0;
break;
end;
end;
%Here we assign the value of this pixel to bSeed, so we can call a
%variable rather than a matrix.
bSeed=raw(YSeed,XSeed);
%We then increase the counts of black, white, and total segments.
if bSeed==0;
iBlacks=iBlacks+1;
end;
if bSeed==1;
iWhites=iWhites+1;
end;
iTotal=iTotal+1;
%We then set the cursor, and mark that this pixel has been assigned a
segment (in the
%Notepad matrix), and keep track of which segment it is assigned (in
%the PaintbyNo matrix).
XCursor=XSeed;
YCursor=YSeed;
XRight=XSeed;
YUpper=YSeed;
Notepad(YCursor,XCursor)=1;
PaintbyNo(YCursor,XCursor)=iTotal;
%Part "D" - Do this while the lower neighbor is a new member of the
%segment.
while ((YCursor-1)>=1) && (raw((YCursor-1),XCursor)==bSeed) &&
(Notepad((YCursor-1),
XCursor)==0);
Notepad((YCursor-1),XCursor)=1;
PaintbyNo((YCursor-1),XCursor)=iTotal;
YCursor=YCursor-1;
end;
%Part "E" - Do this while the left neighbor is a new member of the
%segment. Note, D is nested within this loop.
while ((XCursor-1)>=1) && (raw(YCursor,(XCursor-1))==bSeed) &&
(Notepad(YCursor,
(XCursor-1))==0);
Notepad(YCursor,(XCursor-1))=1;
PaintbyNo(YCursor,(XCursor-1))=iTotal;
XCursor=XCursor-1;
while ((YCursor-1)>=1) && (raw((YCursor-1),XCursor)==bSeed) && (Notepad
((YCursor-1),XCursor)==0);
Notepad((YCursor-1),XCursor)=1;
PaintbyNo((YCursor-1),XCursor)=iTotal;
YCursor=YCursor-1;
end;

```

```

end;
%Part "F" - If right neighbor is a new member, mark it and update
%border.
if ((XCursor+1)<=lWidth) && (raw(YCursor,(XCursor+1))==bSeed) &&
(Notepad(YCursor,
(XCursor+1))==0);
Notepad(YCursor,(XCursor+1))=1;
PaintbyNo(YCursor,(XCursor+1))=iTotal;
if XRight < (XCursor+1);
XRight = XCursor+1;
end;
end;
%Part "G" - If upper neighbor is a new member, mark it and update
%border.
if ((YCursor+1)<=lHeight) && (raw((YCursor+1),XCursor)==bSeed) &&
(Notepad
((YCursor+1),XCursor)==0);
Notepad((YCursor+1),XCursor)=1;
PaintbyNo((YCursor+1),XCursor)=iTotal;
if YUpper < (YCursor+1);
YUpper=YCursor+1;
end;
end;
%Part "H" - Step cursor to the right, or at extreme left of next
%"upper" line.
XCursor=XCursor+1;
if XCursor > XRight;
XCursor=XSeed;
YCursor=YCursor+1;
end;
%Part "I" - Do this until you have surpassed the upper border.
while YCursor <= YUpper;
%Part "J" - If pixel at cursor is not the value, go to next pixel
%using "H"
if raw(YCursor,XCursor)~=bSeed;
XCursor=XCursor+1;
if XCursor > XRight;
XCursor=XSeed;
YCursor=YCursor+1;
end;
continue;
end;
%Part "K" - If pixel at cursor is not already marked, go to next
%pixel using "H"
if Notepad(YCursor,XCursor)==0;
XCursor=XCursor+1;
if XCursor > XRight;
XCursor=XSeed;
YCursor=YCursor+1;
end;
continue;
end;
%Nested Loop!
%Part "D" - Do this while the lower neighbor is a new member of the
%segment.
while ((YCursor-1)>=1) && (raw((YCursor-1),XCursor)==bSeed) &&
(Notepad((YCursor-

```

```

1),XCursor)==0);
Notepad((YCursor-1),XCursor)=1;
PaintbyNo((YCursor-1),XCursor)=iTotal;
YCursor=YCursor-1;
end;
%Part "E" - Do this while the left neighbor is a new member of the
%segment. Note, D is nested within this loop.
while ((XCursor-1)>=1) && (raw(YCursor,(XCursor-1))==bSeed) &&
(Notepad(YCursor,
(XCursor-1))==0);
Notepad(YCursor,(XCursor-1))=1;
PaintbyNo(YCursor,(XCursor-1))=iTotal;
XCursor=XCursor-1;
while ((YCursor-1)>=1) && (raw((YCursor-1),XCursor)==bSeed) && (Notepad
((YCursor-1),XCursor)==0);
Notepad((YCursor-1),XCursor)=1;
PaintbyNo((YCursor-1),XCursor)=iTotal;
YCursor=YCursor-1;
end;
end;
%Part "F" - If right neighbor is a new member, mark it and update
%border.
if ((XCursor+1)<=lWidth) && (raw(YCursor,(XCursor+1))==bSeed) &&
(Notepad(YCursor,
(XCursor+1))==0);
Notepad(YCursor,(XCursor+1))=1;
PaintbyNo(YCursor,(XCursor+1))=iTotal;
if XRight < (XCursor+1);
XRight = XCursor+1;
end;
end;
%Part "G" - If upper neighbor is a new member, mark it and update
%border.
if ((YCursor+1)<=lHeight) && (raw((YCursor+1),XCursor)==bSeed) &&
(Notepad
((YCursor+1),XCursor)==0);
Notepad((YCursor+1),XCursor)=1;
PaintbyNo((YCursor+1),XCursor)=iTotal;
if YUpper < (YCursor+1);
YUpper=YCursor+1;
end;
end;
%Part "H" - Step cursor to the right, or at extreme left of next
%"upper" line.
XCursor=XCursor+1;
if XCursor > XRight;
XCursor=XSeed;
YCursor=YCursor+1;
end;
end;
end;
%Format the output. Will be a 3D array. output(:, :, 1) will be the
%PaintbyNo. The other stacks will contain the number of white segments
%(iWhites), the number of black segments (iBlacks), and the total
number of
%segments(iTotal).
output=zeros(lHeight,lWidth,4);

```

```

output(:, :, 1) = PaintbyNo;
output(1, 1, 2) = iBlacks;
output(1, 1, 3) = iWhites;
output(1, 1, 4) = iTotals;
%End of program

function output =
roifiles2(film, film2, custnum1, custnum2, custnum3, custnum4, drawnumber,
splinesx, splinesy)
%
% roifiles2.m
%
% Copyright 2009-2011,
% Baylor College of Medicine and Rice University,
% All Rights Reserved
%
% ***Subroutine for vesselmosaic.m
%
% Creates an overlay file that defines a list of regions of interest
% (ROIs) in a format that is readable by Zeiss AIM or Zen software.
%
% By default, the file is created with a .rls extension, which is used
% for the AIM software. For use with the Zen software, simply change
the
% file extension to .ovl
%
% .rls files must be placed into the folder C:\AIM\ROIS
% .ovl files must be loaded using the Zen GUI
%
% Input arguments:
% film = Name and path of a template .rls file. This file must be
% a .rls file defining a list of Polyline ROIs
% film2 = Name and path for the new overlay file to be created
% custnum1 = First digit in file identifier number
% custnum2 = Second digit in file identifier number
% custnum3 = Third digit in file identifier number
% custnum4 = Fourth digit in file identifier number
% drawnumber = Number of ROIs to be defined
% splinesx = Matrix containing the x coordinates of each ROI vertex
% splinesy = Matrix containing the y coordinates of each ROI vertex
%
% Notes:
% - file identifier number is an arbitrary tag for distinguishing
between
% different overlay files
% - each row of splinesx and splinesy defines an individual ROI, and
should
% be formatted like this:
% splinesx = [lx rx rx lx] splinesy = [uly ury lry lly]
% . . . . .
% . . . . .
% . . . . .
%
% x-coordinates defining: y-coordinates defining:
% lx = left vertices uly = upper left vertex
% rx = right vertices ury = upper right vertex
% lly = lower left vertex

```

```

% lry = lower right vertex
%
% *notice that upper and lower vertices have the same x-value, making
% each ROI vertically simple.
% *vertices are defined as distance from the center of the field of
% view, in units of meters
%
%Initialize variables
clear A
clear ver1
clear hor1
clear ver2
clear hor2
pl=1;
%Open and read template file
fid=fopen(filnm);
%Each line of the template file is stored to the variable A
A(pl:pl+35,1) = fread(fid,36,'uint8');
pl=pl+36;
filnamnum = fread(fid,1,'uint32');
A(pl,1)=filnamnum;
pl=pl+1;
A(pl:pl+filnamnum,1)= fread(fid,filnamnum+1,'uint8');
pl=pl+filnamnum+1;
numelements = fread(fid,1,'int32');
A(pl,1)=numelements;
pl=pl+1;
totsize = fread(fid,1,'int32');
A(pl,1)=totsize;
pl=pl+1;
A(pl:pl+20,1) = fread(fid,21,'int32');
pl=pl+21;
A(pl:pl+31,1) = fread(fid,32,'uint16');
pl=pl+32;
A(pl:pl+9,1) = fread(fid,10,'int32');
pl=pl+10;
for i=1:numelements
drawelemtype = fread(fid,1,'int32');
A(pl,1)=drawelemtype;
pl=pl+1;
%This segment of the code assumes that the template file only defines
%polyline ROIS
elemsize = fread(fid,1,'int32');
A(pl,1)= elemsize;
pl=pl+1;
A(pl:pl+1,1) = fread(fid,2,'int32');
pl=pl+2;
A(pl:pl+1,1) = fread(fid,2,'float64');
pl=pl+2;
A(pl:pl+16,1) = fread(fid,17,'int32');
pl=pl+17;
A(pl:pl+31,1) = fread(fid,32,'uint16');
pl=pl+32;
A(pl,1) = fread(fid,1,'int32');
pl=pl+1;
A(pl:pl+8,1) = fread(fid,9,'int32');
pl=pl+9;

```

```

numvertex = fread(fid,1,'int32');
A(pl,1)=numvertex;
pl=pl+1;
clear xxx
clear yyy
for j=1:numvertex
xxx(i,j) = fread(fid,1,'float64');
A(pl,1)=xxx(i,j);
pl=pl+1;
yyy(i,j) = fread(fid,1,'float64');
A(pl,1)=yyy(i,j);
pl=pl+1;
end
end
A(pl,1) = fread(fid,1,'int32');
%Template file is closed
fclose(fid)
pl=1;
%New overlay file is created
fid=fopen(filnm2,'w');
%Where appropriate, lines from the template file are directly copied to
%this new file
fwrite(fid,A(pl:pl+35,1),'uint8');
pl=pl+36;
%Here, the internal name of the overlay file is defined
fwrite(fid,uint32(7),'uint32');
pl=pl+1;
fwrite(fid,uint8('J'),'uint8');
fwrite(fid,uint8('C'),'uint8');
fwrite(fid,uint8('C'),'uint8');
fwrite(fid,uint8(custnum1),'uint8');
fwrite(fid,uint8(custnum2),'uint8');
fwrite(fid,uint8(custnum3),'uint8');
fwrite(fid,uint8(custnum4),'uint8');
fwrite(fid,A(pl+filnamnum,1),'uint8');
pl=pl+filnamnum+1;
%The number of ROIs is defined, and the size of the file is defined
fwrite(fid,int32(drawnumber),'int32');
pl=pl+1;
fwrite(fid,int32((200+(drawnumber*272))),'int32');
pl=pl+1;
fwrite(fid,A(pl:pl+20,1),'int32');
pl=pl+21;
fwrite(fid,A(pl:pl+31,1),'uint16');
pl=pl+32;
fwrite(fid,A(pl:pl+9,1),'int32');
pl=pl+10;
plremember=pl;
%Each ROI is defined using the coordinates from splinex and spliney
for i=1:drawnumber
pl=plremember;
fwrite(fid,int32(20),'int32');
pl=pl+1;
fwrite(fid,int32(272),'int32');
pl=pl+1;
fwrite(fid,A(pl:pl+1,1),'int32');
pl=pl+2;

```



```

fwrite(fid,A(pl:pl+1,1),'float64');
pl=pl+2;
fwrite(fid,A(pl:pl+16,1),'int32');
pl=pl+17;
fwrite(fid,A(pl:pl+31,1),'uint16');
pl=pl+32;
fwrite(fid,A(pl,1),'int32');
pl=pl+1;
fwrite(fid,A(pl:pl+8,1),'int32');
pl=pl+9;
fwrite(fid,int32(4),'int32');
fwrite(fid,double(splines(i,1)),'float64');
fwrite(fid,double(spliney(i,1)),'float64');
fwrite(fid,double(splines(i,2)),'float64');
fwrite(fid,double(spliney(i,2)),'float64');
fwrite(fid,double(splines(i,3)),'float64');
fwrite(fid,double(spliney(i,3)),'float64');
fwrite(fid,double(splines(i,4)),'float64');
fwrite(fid,double(spliney(i,4)),'float64');
end
stest=size(A);
stest2=stest(1);
fwrite(fid,A(stest2,1),'int32');
%The file is finished and closed
fclose(fid)
%The file is written to the working directory; there is no other
functional
%output by the program
output=0;
%End of program

```